Inertial particles in unsteady hydrodynamic environments: theory and numerics

A Thesis

Submitted to the
Tata Institute of Fundamental Research, Mumbai
Subject Board of Physics
for the degree of Doctor of Philosophy

by

Divya Jaganathan

International Centre for Theoretical Sciences
Tata Institute of Fundamental Research
Bengaluru, India

October, 2024

Final version submitted in
March, 2025

Declaration

This thesis is a presentation of my original research work. Wherever contributions of others are involved, every effort is made to indicate this clearly, with due reference to the literature, and acknowledgment of collaborative research and discussions.

The work was done under the guidance of Professor Rama Govindarajan at the International Centre for Theoretical Sciences, Tata Institute of Fundamental Research (ICTS-TIFR), Bangalore. Prof. Vishal Vasan served as co-supervisor.

Divya Jaganathan

In my capacity as the formal supervisor of record of the candidate's thesis, I certify that the above statements are true to the best of my knowledge.

Rama Govindarajan
Date: 01-March-2025

Acknowledgements

Firstly, I thank my advisors, Professors Rama Govindarajan and Vishal Vasan, for their invaluable guidance throughout my PhD journey. They have been encouraging, kind, accessible and patient. I am grateful for the many fruitful research opportunities they gave me over the years and the freedom to pursue the research problems that interested me. I would also like to thank Ganga Prasath who got me interested in the topic of my thesis research.

I thank my collaborators on various projects that form part of this thesis: Ganga Prasath, Rahil N. Valani, Saumav Kapoor, Tomek Jaroslawski, and Professor Beverley McKeon. Godwin, Harshit, and Omkar have patiently helped me with *Mathematica*, and Rajarshi with all things computer and coding. Interactions with the fellow graduate students at ICTS have been helpful. Insightful questions from Professors Abhishek Dhar and Loganayagam, even if over limited interactions, prompted interesting lines of inquiry that rekindled my enthusiasm at work on several occasions.

I thank my thesis monitoring committee: Professors Samriddhi Sankar Ray and Duvvuri Subrahmanyam, and my synopsis committee: Professors Brato Chakraborti, Vijay Krishnamurthy, Shashi Thutupalli and Prasad Perlekar for their time and feedback. I would also like to thank my thesis reviewers, Professors Jean-Luc Thiffeault and Manikandan Mathur for their comments and questions which helped improve the thesis.

My stay at ICTS has been positively supported by the administrative and scientific & technical teams. I thank Jeeva, Deepali, Pavana, Veena, Nidhi, Jenny, Madhulika, Sunitha, Ramya, Renu for their assistance through the administrative procedures. I thank Hemanta, Prashanth, Irshad for the help with the computational facilities and Gobi, Shantaraj, Naveen for their IT/AV assistance. I thank Basavaraj and Suresh for the logistical assistance and their support to the graduate students, specially during the pandemic. The cafeteria has been the place for many welcome encounters and distractions on dull and productive days alike. I thank Naga and the cafeteria staff for patiently pouring us countless cups of coffee and tea. I also thank the housekeeping staff for selflessly keeping up our workspace. I appreciate the access to the NCBS common spaces, where I often escaped the feeling of workspace monotony.

I enjoyed the company of many at ICTS, engaging in random conversations, watching movies and cricket, frequenting music concerts and plays, playing TT together: Vee (Aditya), Junaid, Aditya, Jitendra, Srashti, Chandra, Saikat, Praneet, Basudeb, Akhil, Apratim, Bhanu, Rahul, Jason, Sangeeth, Sunil, Rajarshi, Ritwik, Santhiya, Siddharth, Siddhartha, Sharath, Shashank, Shivam, Sugan, Omkar, Irshad, Chandru. Jigyasa has been a joyful company, both as an office mate and a friend. Dinners and late-night ice-cream escapades with Godwin, Nirnoy, Tamoghna, Priyadarshi provided much-needed cool-off on long days. I thank Rahul Singh, Ganga, Krishnendu, Adhip, Sharath, Siddhartha for being accessible for conversations, helping me navigate the work and the workplace better. My friends from the outside world: Harkirat, Rajesh 'Tina', Mandakini, Lisa, Elackiya, Pompi, Prerna, Sudha, Swetha, brought in the balance and perspective.

I thank my family for their encouragement and understanding throughout my convoluted academic journey. My mother unwittingly showed the strength of patience, resilience and spiritedness through her way of life–qualities often in short supply in my personality. My brother, Anirudh, showed the most faith and reminded me at times of exhaustion to preserve the fun in what I do. I recall my father once encouragingly telling me in a moment of self-doubt, "Go, be a small fish in a big pond. It's alright." In hindsight, I have benefited from these humbling words for replacing fear with a sense of opportunity. Swethaa has been generous with her support. I am incredibly lucky to receive unconditional affection from my niece and nephew, Srishti and Vedant, who have been a source of relief and much-coveted silly joy in the past many years! Many members of my extended family have provided a strong support system to us during both good and trying times.

Finally, I would like to acknowledge the support extended by the Department of Atomic Energy, Government of India, under project no. RTI4001, the Infosys Foundation Excellence Program of ICTS and the Infosys-TIFR Leading Edge Travel Grant.

List of Tables

List of Figures

Contents

Abstract

Inertial particles with finite size and mass move differently from the surrounding flow due to finite-time hydrodynamic response of both the particle and fluid to perturbations. While viscosity-dominated Stokes flows are well-studied under steady conditions, the unsteady route to the steady state remains less explored. In this thesis, we examine the transport of inertial particles using the unsteady Stokes model, capturing the non-instantaneous relaxation effects. We revisit the classical problem of a sphere settling in a viscous fluid under gravity using the unsteady Stokes model, highlighting the emergence of memory effects, and compare our theoretical findings with experimental observations from our collaborators. To address the computational challenges of incorporating memory effects in particle dynamics for general flows, we develop a memoryless framework using a Markovian embedding procedure. This results in an explicit integrator, called the RK-χTD schemes, for solving the governing Maxey-Riley-Gatignol (MRG) equation. The RK-χTD schemes significantly reduce computational costs, making the MRG equation as accessible to numerical solutions as ordinary differential equations. We show how the approach may be generalized to other nonlocal evolutionary equations. We numerically investigate memory effects on non-interacting particles in rotating vortical flows. Finally, we describe a two-dimensional multi-particle model with fluid-mediated interactions in the unsteady Stokes regime, setting the framework for future development of an MRG analogue that includes interactions.

Chapter 1

Introduction

Small particles or droplets suspended in, and interacting with, a background fluid are common in various physical systems across different length and timescales. Examples include microswimmers in biological fluids, dust particles in air, bouncing droplets off a fluid surface, and water droplets in the clouds. How the particles, or equivalently, droplets, move upon interacting with the background fluid – both individually and collectively in the presence of other particles – dictates several important large-scale emergent phenomena. For instance, organic matter and plankton, ranging in size from several nanometers to micrometers, aggregate to form millimeter-sized marine snow that settle in the ocean, which is critical to oceanic carbon sequestration [5, 6]. Small and large marine animals swimming in the ocean induce flows which positively contribute to biogenic mixing [7, 8]. In the Earth's atmosphere, micrometer-sized water droplets in the cloud coalesce to form bigger raindrops through various mechanisms [9, 10], crucial for eventual precipitation.

These particle-laden flows exhibit complex coupled dynamics: the particle perturbs the surrounding flow as it moves, and these perturbations, in turn, influence the particle's motion. In many cases, these perturbations are small. A key factor in studying these coupled dynamics is the response time of both the particle and the fluid to each other's perturbations. We consider scenarios, such as those in microhydrodynamic applications, where both the particle and the fluid have perceptible response times to perturbations over the timescale of the phenomenon in question, such that neither instantly relaxes to a quasi-steady state upon interacting. Instead, owing to finite inertia, each relaxes non-instantaneously, resulting in a nontrivial transient dynamic route to the quasi-steady state. It is in this sense of their response behavior that we refer to particles with finite mass and size as '*inertial*'. In this thesis, we focus on the *unsteady* particle motion in spatio-temporally varying flows due to the finite-time response dynamics.

Critical to characterizing various aspects of inertial particle transport in flows is an

accurate description of particles' motion in the fluid. This involves studying the different forces on the particles as they move through the fluid. To relate the forces to the motion, we write the equation of motion in its most general form for a single particle of mass m_p and arbitrary shape in a flow field using Newton's law:

$$m_p \frac{d\boldsymbol{V}_p'(t')}{dt'} = \boldsymbol{f}_H'(t') + \boldsymbol{f}_{\mathrm{NH}}'(t') \ , \tag{1.1}$$

where $\boldsymbol{V}_p'(t')$ is the particle's instantaneous translational velocity, related to its position vector $\boldsymbol{X}_p'(t')$ by $d\boldsymbol{X}_p'(t')/dt' = \boldsymbol{V}_p'(t')$ and t' denotes time. For easy interpretation, we have decomposed the total driving force on the particle into hydrodynamic $\boldsymbol{f}_H'$ and non-hydrodynamic $\boldsymbol{f}_{\mathrm{NH}}'$. All quantities with the prime symbols $(\cdot)'$ are dimensional. The dynamical nature of eq. (1.1) reflects particle's finite inertia. In contrast, neglecting the particle's inertia reduces eq. (1.1) to an instantaneous force balance relation ($\boldsymbol{f}_H' + \boldsymbol{f}_{NH}' = 0$), which is often used to model force-free particles in suspensions [11].

Non-hydrodynamic forces may include external body forces due to gravity and electromagnetic fields, short-ranged inter-particle forces of molecular origins such as the van der Waals', and stochastic Brownian forces due to thermal motion of fluid. We focus on the hydrodynamic forces exerted by the surrounding flow, including fluid-mediated interaction forces due to other particles. The significance of hydrodynamic forces compared to other forces in the steady-state equilibrium varies across different length scales. Typically, larger particles such as rocks (several centimeters in size) are minimally influenced by hydrodynamic forces, where the body forces often dominate. On the other hand, smaller particles such as colloidal particles ($0.01 - 0.1\mu$m) are predominantly driven by Brownian forces. In the intermediate size range of a few hundred micrometers to a few millimeters, Brownian effects are negligible, but hydrodynamic forces become significant. When making these comparisons, the particle size is measured relative to a typical flow length scale. We are concerned with particles in the intermediate size range. In non-equilibrium states, however, the interplay between length scales and timescales become crucial, potentially altering the dominant balance of forces, which will be discussed in section 1.1.

The hydrodynamic force on a particle is given by the surface integral of traction, $\boldsymbol{\sigma}' \cdot \boldsymbol{n}$, that develops on the particle's surface due to the surrounding fluid:

$$\boldsymbol{f}_H'(t') = \oint_{\boldsymbol{x}' \in \partial\mathcal{V}(t')} \boldsymbol{\sigma}'(\boldsymbol{v}'(\boldsymbol{x}', t'),\ p'(\boldsymbol{x}', t')) \cdot \boldsymbol{n}(\boldsymbol{x}')\, dS(\boldsymbol{x}') \ ,$$

where the fields $(\boldsymbol{v}', p')$ denote the velocity vector and hydrodynamic pressure of the particle-induced flow. Here, $\boldsymbol{\sigma}'$ represents the fluid stress tensor, $\partial\mathcal{V}(t')$ denotes the moving particle's

surface, which bounds the exterior fluid volume $\mathcal{V}$, $\boldsymbol{n}$ denotes the unit normal vector directed outwards from the surface $\partial\mathcal{V}$ (see fig. 1.3) and $dS(\boldsymbol{x}')$ is the surface measure in the vector space $\boldsymbol{x}'$. The specific form of the hydrodynamic stress, $\boldsymbol{\sigma}'$, depends on the suspending fluid's response behavior to local deformations. The response behavior is given by a *constitutive relation* between stress and a quantity characterizing the deformation, such as strain or strain rate. For isotropic Newtonian fluids, the stress tensor depends linearly on the velocity gradient $\boldsymbol{\nabla}'\boldsymbol{v}'$ and hydrodynamic pressure p' [12]:

$$\boldsymbol{\sigma}' = -p'\mathbb{I}_d + \mu(\boldsymbol{x}', t')[\boldsymbol{\nabla}'\boldsymbol{v}' + (\boldsymbol{\nabla}'\boldsymbol{v}')^T] + \mu^*(\boldsymbol{x}', t')(\boldsymbol{\nabla}' \cdot \boldsymbol{v}')\mathbb{I}_d \ ,$$

where $\mathbb{I}_d$ is the identity matrix in $d-$dimensional space occupied by the fluid (typically $d = 2, 3$), the superscript T indicates transpose operation, and μ, μ^* are the fluid's dynamic and bulk viscosity, respectively. In many cases, such as in stratified flows [13], the viscosity may vary spatio-temporally with temperature, salinity, and other factors. However, we restrict ourselves to the case of constant viscosity.

Integrating the traction over the particle's surface gives the driving hydrodynamic force. Evaluating the surface traction requires the knowledge of the flow field $(\boldsymbol{v}', p')$ which, for a fluid of density ρ_f, evolves dynamically according to the following momentum balance equation:

$$\rho_f\Big(\frac{\partial \boldsymbol{v}'}{\partial t'} + \boldsymbol{v}' \cdot \boldsymbol{\nabla}'\boldsymbol{v}'\Big) = \boldsymbol{\nabla}' \cdot \boldsymbol{\sigma}' + \boldsymbol{F}'_{\text{ext}}(\boldsymbol{x}', t') \ , \tag{1.2}$$

subject to an external forcing $\boldsymbol{F}'_{\text{ext}}$ and appropriate boundary conditions at the particle's surface. The above equation is supplemented by a mass-conservation equation:

$$\frac{\partial \rho_f}{\partial t'} + \boldsymbol{\nabla}' \cdot (\rho_f \boldsymbol{v}') = 0 \implies \frac{D\rho_f}{Dt'} + \rho_f \boldsymbol{\nabla}' \cdot \boldsymbol{v}' = 0 \ . \tag{1.3}$$

For incompressible flows, the density of an arbitrary small continuum fluid parcel is constant, i.e., $D\rho_f/Dt' = 0$, where D/Dt' is the material derivative following the fluid parcel. This leads to the commonly-used divergence-free condition for incompressibility, $\boldsymbol{\nabla}' \cdot \boldsymbol{v}' = 0$. As a result, the expression for the divergence of the stress tensor in eq. (1.2) simplifies as follows,

$$\boldsymbol{\nabla}' \cdot \boldsymbol{\sigma}' = -\boldsymbol{\nabla}' p' + \mu \boldsymbol{\nabla}'^2 \boldsymbol{v}' + (\mu + \mu^*)\boldsymbol{\nabla}'(\boldsymbol{\nabla}' \cdot \boldsymbol{v}') = -\boldsymbol{\nabla}' p' + \mu \boldsymbol{\nabla}'^2 \boldsymbol{v}' \ .$$

Substituting the above relation in eq. (1.2) gives the *Navier-Stokes equation* for *incompressible* flows with uniform viscosity.

Different hydrodynamical models for inertial particles are derived from eq. (1.1) by incorporating dominant hydrodynamic forces that emerge from the fluid dynamics (eq. (1.2)),

at the relevant time and length scales of the phenomena of interest. At the smaller length scales of the particle, viscous forces dominate. When the particle-induced perturbations are sufficiently small, which is likely in the viscosity-dominated conditions, the dynamics follows a linear Stokes theory. This theory is characterized by a small nondimensional Reynolds number, Re_p, which is defined based on the particle's size and particle-induced velocity perturbation in the flow. To distinguish from the Reynolds number associated with the ambient unperturbed flow field, we refer to Re_p as the *particle* Reynolds number. Unsteady dynamics warrants a careful assessment of the timescales involved in the system, which introduces yet another nondimensional number, also a ratio of timescales, called the *Stokes number*, denoted by S. In the following sections, we discuss the Stokesian regime, the primary theme of this thesis, where we define these nondimensional numbers precisely and describe the dominant hydrodynamic physics as we account for fluid's inertia marked by finite-time relaxation.

In the rest of the thesis, we assume the particles are spherical and rigid, unless mentioned otherwise. The symmetry of the assumed geometry greatly simplifies many calculations, and rigidity enforces *no-slip* boundary conditions at the particle-fluid interfaces. Also, we consider particles heavier than the fluid such that $\rho_p > \rho_f$. We reiterate our assumptions regarding the fluid that it is Newtonian and incompressible.

1.1 Overview of unsteady Stokesian dynamics

In this section, we discuss the unsteady version of the Stokes theory relevant in particle-laden flows and the associated nondimensional parameters. The purpose is to outline the minimal hydrodynamic theory for viscosity-dominated flows, incorporating the fluid's finite-time relaxation and the forces acting on the inertial particle as a result. To that end, for simplicity, we ignore external forces on the fluid without any loss of generality.

1.1.1 Leading order flow physics

The purpose of this subsection is to derive the leading-order governing equation for the particle-laden flow in the viscosity-dominated regime using scale analysis. We consider the flow field that develops as a particle moves through a background flow, which in the absence of the particle is $(\boldsymbol{u}'^{\infty},\ p'^{\infty})$. The presence of the particle perturbs this free-space[1] background field locally, leading to the perturbed field $(\boldsymbol{v}', p')$, supported in the exterior volume $\mathcal{V}$ (see fig. 1.3). Assuming incompressibility and uniform viscosity of the fluid, we write the Navier-

[1]We call $\boldsymbol{u}'^{\infty}$ a free-space field since it is supported in the entire space $\mathbb{R}^3$ with no particle.

Stokes equation for the perturbed flow subject to boundary and initial conditions:

$$\rho_f\Big(\frac{\partial \boldsymbol{v}'}{\partial t'} + \boldsymbol{v}'\cdot\boldsymbol{\nabla}'\boldsymbol{v}'\Big) = -\boldsymbol{\nabla}' p' + \mu\boldsymbol{\nabla}'^2\boldsymbol{v}', \tag{1.4a}$$

$$\boldsymbol{\nabla}'\cdot\boldsymbol{v}' = 0\ , \tag{1.4b}$$

$$\boldsymbol{v}'(\boldsymbol{x}', 0) = \boldsymbol{v}_0'(\boldsymbol{x}')\ , \tag{1.4c}$$

$$\boldsymbol{v}'(\boldsymbol{x}', t') = \boldsymbol{V}_p'(t')\ \text{ on the particle's surface}\ , \tag{1.4d}$$

$$\boldsymbol{v}'(\boldsymbol{x}', t') \to \boldsymbol{u}'^{\infty}(\boldsymbol{x}', t')\ ,\ p'(\boldsymbol{x}', t') \to p'^{\infty}(\boldsymbol{x}', t')\ \text{ as } |\boldsymbol{x}' - \boldsymbol{X}_p'(t)| =: r' \to \infty\ , \tag{1.4e}$$

where eq. (1.4e) suggests that at far-field the flow is unperturbed by the particle and is given by the free-space field ($\boldsymbol{u}'^{\infty},\ p'^{\infty}$). For the order-of-magnitude comparison, it suffices to consider a quiescent background flow ($\boldsymbol{u}'^{\infty} \equiv 0$), simplifying the analysis to focus on the time and length scales intrinsic to the particle-induced dynamics. We will briefly address the case of the nonuniform, unsteady background flow, which introduces external scales, at the end of this subsection.

The dimensional equations above contain parameters ρ_f and μ which are fundamental properties of the fluid. Rewriting the equations in terms of dimensionless variables eliminates the explicit dependence on these parameters in favor of deriving an equation for a broader class of flow conditions. The exercise further allows us to estimate the size of various terms in the momentum balance to extract the leading order physics.

We nondimensionalise the equation by introducing a length scale L_c, a timescale T_c, and a velocity scale U_c. In typical particle-laden flows, the particle radius a_p serves as a relevant representative length scale, so we set $L_c = a_p$. We will explicitly state it when a different choice is warranted during the discussion. The velocity U_c is a characteristic measure of the particle-induced perturbed flow velocity. The timescale T_c depends on the phenomenon of interest, often related to the background flow, which will be stated explicitly on a case-by-case basis. For the scenarios we wish to consider, reflecting finite-time relaxation of the fluid, we allow an independent choice for T_c, different from a_p/U_c. The resulting nondimensional variables are,

$$\frac{t'}{T_c} \to t\ ,\ \frac{\boldsymbol{x}'}{a_p} \to \boldsymbol{x}\ ,\frac{\boldsymbol{v}'}{U_c} \to \boldsymbol{v}\ ,\ \frac{p'}{P_c} \to p\ .$$

Consequently, the equation of motion for the nondimensional perturbed field reads

$$\Big(\frac{\rho_f U_c}{T_c}\Big)\frac{\partial \boldsymbol{v}}{\partial t} + \Big(\frac{\rho_f U_c^2}{a_p}\Big)\boldsymbol{v}\cdot\boldsymbol{\nabla}\boldsymbol{v} = -\Big(\frac{P_c}{a_p}\Big)\boldsymbol{\nabla} p + \Big(\frac{\mu U_c}{a_p^2}\Big)\boldsymbol{\nabla}^2\boldsymbol{v}, \tag{1.5a}$$

$$\boldsymbol{\nabla}\cdot\boldsymbol{v} = 0\ , \tag{1.5b}$$

where the variables without primes are dimensionless. We distinguish between two terms in eq. (1.5) related to fluid inertia: we refer to the Eulerian acceleration $\partial \boldsymbol{v}/\partial t$ as *unsteady inertia*, and the nonlinear term $\boldsymbol{v}\cdot\boldsymbol{\nabla}\boldsymbol{v}$ as the *convective inertia*. To compare the relative size of all the terms in the viscosity-dominated regime, we divide the entire equation by $\mu U_c/a_p^2$, ensuring the viscous term dominates the balance.

The choice for the characteristic scale for the pressure variable is yet to be made. There are two choices: $P_c = \{\mu U_c/a_p,\ \rho_f U_c^2\}$. To reflect the viscosity-dominated regime, we choose $P_c = \mu U_c/a_p$. As a result, the nondimensional equation of motion becomes

$$S\frac{\partial \boldsymbol{v}}{\partial t} + Re_p \boldsymbol{v}\cdot\boldsymbol{\nabla}\boldsymbol{v} = -\boldsymbol{\nabla}p + \boldsymbol{\nabla}^2\boldsymbol{v}, \tag{1.6a}$$

$$\boldsymbol{\nabla}\cdot\boldsymbol{v} = 0\ , \tag{1.6b}$$

where the nondimensional Stokes and particle Reynolds numbers are

$$S = a_p^2/(\nu T_c)\ ,\quad Re_p = a_p U_c/\nu\ , \tag{1.7}$$

respectively. Here, $\nu = \mu/\rho_f$ is fluid's kinematic viscosity. The Stokes number S quantifies the relative strength of unsteady inertia ($\partial \boldsymbol{v}/\partial t$) to viscous forces ($\nabla^2\boldsymbol{v}$), while the particle's Reynolds number, Re_p, compares convective inertia ($\boldsymbol{v}\cdot\boldsymbol{\nabla}\boldsymbol{v}$) to viscous forces. When viscous effects dominate, we have $Re_p \ll 1$, and the dominant balance includes the pressure gradient and the viscous term, both linear in $\boldsymbol{v}$ and p. The convective inertia term drops off, whereas we retain the unsteady inertia term, which reflects the fluid's unsteady or finite-time response, whose relative strength is determined by S. Thus, in the $Re_p \ll 1$ limit, the dominant balance in eq. (1.6) is represented by the Stokes equation. Further distinction between steady and unsteady behavior thereafter is based on S: the limit $S \to 0$, corresponding to instantaneous fluid relaxation over the timescale T_c, yields the steady Stokes theory, whereas allowing for finite $S > 0$ corresponds to its unsteady counterpart.

A comment on the other choice for characteristic pressure is in order here. Suppose we make the alternative choice, i.e., $P_c = \rho_f U_c^2$ [14]. In this case, the pressure gradient becomes $\mathcal{O}(Re_p)$ and drops out of the leading-order balance, resulting in a $d-$dimensional vector diffusion equation for $\boldsymbol{v}$. This, however, introduces inconsistency if we also demand incompressibility, since the system becomes over-constrained with $(d+1)$ equations for d unknown variables. An insightful reflection of this inconsistency stemming from a poor choice of characteristic pressure is that pressure enforces incompressibility in low-Reynolds number flows[2]. Choosing $P_c = \mu U_c/a_p$ ensures that the pressure gradient remains in the

[2]A similar argument can be made for the high-Re_p flows, driving the choice of $P_c = \rho_f U_c^2$ instead.

leading-order balance and couples with the velocity field, ensuring in turn that the $(d+1)$-dimensional system is adequately constrained by as many equations in eq. (1.6).

The nondimensional form of eq. (1.6) broadly applies to a class of flow scenarios characterized by Re_p, S due to *dynamical similarity*. This means that, instead of a specific fluid with density ρ_f and viscosity μ in eq. (1.4), the nondimensional eq. (1.6) describes a family of flow conditions sharing the same boundary and initial conditions, but with different values of ρ_f, μ and the characteristic scales, as long as the corresponding values of Re_p and S remain invariant. Thus, discounting the information on the exact magnitude of each term in the balance, the nondimensional representation preserves the ratios of their strengths and provides a uniform qualitative picture for a class of flows.

To begin with, we have identified the small parameter $Re_p \ll 1$. Therefore, we consider the vanishing Reynolds number limit by setting $Re_p = 0$. This limit enforces a clear and large separation between the fast/short viscous and the slow/long inertial timescales: $a_p^2/\nu \ll a_p/U_c$. A physical interpretation for the viscous timescale can be given as follows. Taking the curl of the first equation in eq. (1.4), upon neglecting the nonlinear term, yields the following diffusion equation for the vorticity field, $\boldsymbol{\omega}' := \boldsymbol{\nabla}' \times \boldsymbol{v}'$,

$$\frac{\partial \boldsymbol{\omega}'}{\partial t'} = \nu \boldsymbol{\nabla}'^2 \boldsymbol{\omega}' \ ,$$

where the kinematic viscosity ν acts as the diffusion coefficient. Thus, the timescale a_p^2/ν is the time it takes for the vorticity generated by the particle-induced field to diffuse over a distance a_p.

The timescale T_c in the Stokes number S is a free parameter, yet to be chosen. When the phenomenon of interest occurs over a faster timescale comparable to the viscous timescale, the Stokes number $S \sim 1$. In a time-dependent dynamical process, $S \sim 1$ may also correspond to the early or short-time dynamics. On the other hand, when the phenomenon of interest is slow and is observed over longer timescales, i.e., $S \ll 1$, the unsteady inertia term becomes negligible, and we recover the classical steady Stokes equation from eq. (1.6) at the leading order:

$$0 = -\boldsymbol{\nabla} p + \boldsymbol{\nabla}^2 \boldsymbol{v} \ , \tag{1.8}$$

which is the common quasi-steady assumption that accurately captures equilibrium states in low-Re_p systems. However, in the interest of capturing the transient dynamics as the fluid relaxes in finite time, we focus on $S > 0$. We scale the nondimensional time further by $t/S \to t$, leading to the following unsteady Stokes equation at the leading order:

$$\frac{\partial \boldsymbol{v}}{\partial t} = -\boldsymbol{\nabla} p + \boldsymbol{\nabla}^2 \boldsymbol{v} \ . \tag{1.9}$$

The above equation governs the primary regime of interest in this thesis (except chapter 6). We shall refer to it as the *unsteady Stokes model*. It is linear and retains the unsteady inertia term, reflecting finite-time relaxation of the fluid to perturbations caused by the particle.

Validity of the unsteady Stokes model: Understanding the validity of the simplified unsteady Stokes model is equally important. In practice, the particle Reynolds number Re_p is never exactly zero, and the effects due to small Re_p, however small, can become significant over the timescale of interest. The dynamics in eq. (1.4) suggests a coupling between length- and timescales. We briefly discuss how small convective inertial effects might emerge in the dynamics when $Re_p \neq 0$ using scale analysis to assess the validity of the unsteady Stokes model, which is derived in the vanishing Re_p limit.

Previously, we set $L_c = a_p$. To account for small convective inertial effects, we now seek an alternative length scale L_c, where convective inertia becomes comparable to the viscous effects. Comparing the coefficients of the corresponding terms in eq. (1.5), we find

$$\frac{\rho_f U_c^2}{L_c} \sim \frac{\mu U_c}{L_c^2} \implies L_c \sim \frac{\nu}{U_c} = a_p Re_p^{-1} \ .$$

The new length scale, ν/U_c, is known as the *Oseen length* [15, 16]. The corresponding timescale, known as the *Oseen timescale*, is ν/U_c^2, which compares to the viscous diffusion time as $a_p Re_p^{-2}$. These scalings suggest that the Oseen length and timescale correspond to the far-field (as measured from the particle's center) and late-time dynamics, respectively. See the schematic in fig. 1.1 for spatial separation.

We now revisit the order-of-magnitude analysis in eq. (1.5) across the spatio-temporal landscape swept by length scales $\{a_p,\ \nu/U_c\}$ and timescales $\{a_p^2/\nu,\ \nu/U_c^2\}$. At early/short times, when $T_c \sim a_p^2/\nu$ (equivalently $S \sim 1$), diffusive dynamics dominates uniformly across length scales, described by eq. (1.9). On the other hand, at later times, when $T_c \sim \nu/U_c^2$ ($S \sim Re_p^2$), distinct behaviors emerge at near ($r' \sim a_p$) and far-field ($r' \sim a_p Re_p^{-1} = \nu/U_c$). Setting $T_c = \nu/U_c^2$ in eq. (1.5), corresponding to later times, the nondimensional equation reveals the following:

$$\text{Near-field } (r' \sim a_p): \quad Re_p^2 \frac{\partial \boldsymbol{v}}{\partial t} + Re_p \boldsymbol{v} \cdot \boldsymbol{\nabla} \boldsymbol{v} = -\boldsymbol{\nabla} p + \boldsymbol{\nabla}^2 \boldsymbol{v} \ , \tag{1.10a}$$

$$\text{Far-field } (r' \sim a_p Re_p^{-1}): \quad Re_p^2 \frac{\partial \boldsymbol{v}}{\partial t} + Re_p^2 \boldsymbol{v} \cdot \bar{\boldsymbol{\nabla}} \boldsymbol{v} = -Re_p \bar{\boldsymbol{\nabla}} p + Re_p^2 \bar{\boldsymbol{\nabla}}^2 \boldsymbol{v} \tag{1.10b}$$

where the variable with the overhead bar is scaled by *Oseen length scale*: $\bar{\boldsymbol{\nabla}} = Re_p^{-1} \boldsymbol{\nabla}$. Close to the particle, eq. (1.10a) suggests steady Stokes dynamics, whereas in the far-field all the

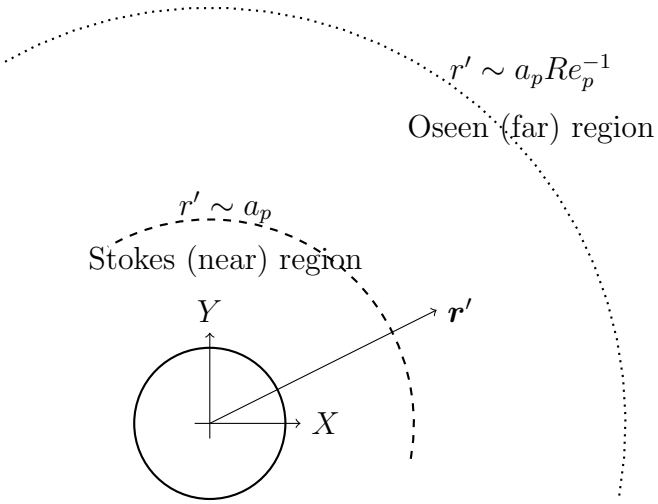

Figure 1.1: Schematic showing development of distinct near and far fields around the particle at late Oseen times $t' \sim \nu/U_c^2$.

terms become comparable to each other, approximated by unsteady Oseen dynamics[3] (see fig. 1.2). A detailed perturbation analysis, such as asymptotic matching, would be needed to address this complex behavior [1, 2, 16], but we do not explore it further. This heuristic dimensional analysis suggests an inertial timescale, like the Oseen timescale in the simplified case considered here, beyond which the unsteady Stokes equation may no longer hold, as the omitted convective inertial term become significant. These inertial effects may become important if they emerge during the timescale of the phenomenon of our interest, warranting further corrections to the unsteady Stokes model.

What if there are multiple inertial timescales? So far, we have considered quiescent background flow for simplicity. In practice, moving particles perturb a non-zero background flow, $\boldsymbol{u}'^{\infty}(\boldsymbol{x}, t)$, which can vary spatially and temporally. The insights from the previous dimensional analysis largely hold for the perturbation field $(\boldsymbol{v}' - \boldsymbol{u}'^{\infty})$ too, showing a spatially heterogeneous dynamics at later times under small fluid inertial effects. However, a non-zero background flow may introduce additional inertial scales besides the intrinsic *Oseen scale*. One such scale, relevant to particle lift dynamics [18], is linked to the local strain rate. This introduces a new, typically small, Reynolds number, $Re_s = a^2 s_*/\nu$, called the *shear Reynolds number*, based on the inverse shear rate $s_*^{-1} \sim 1/|\boldsymbol{\nabla}' \boldsymbol{u}'^{\infty}|$. This requires careful consideration of various limiting cases characterizing the dominant source of inertia: the Oseen limit ($Re_s^{1/2} \ll Re_p \ll 1$), where convective inertia dominates over shear-induced inertia, and the Saffman limit ($Re_p \ll Re_s^{1/2} \ll 1$), where shear-induced inertia prevails. Both these limits have been studied previously [19–22]. Evidently, the interplay between

[3]This far-field behavior is similar to Oseen's observation [17] in the steady scenario.

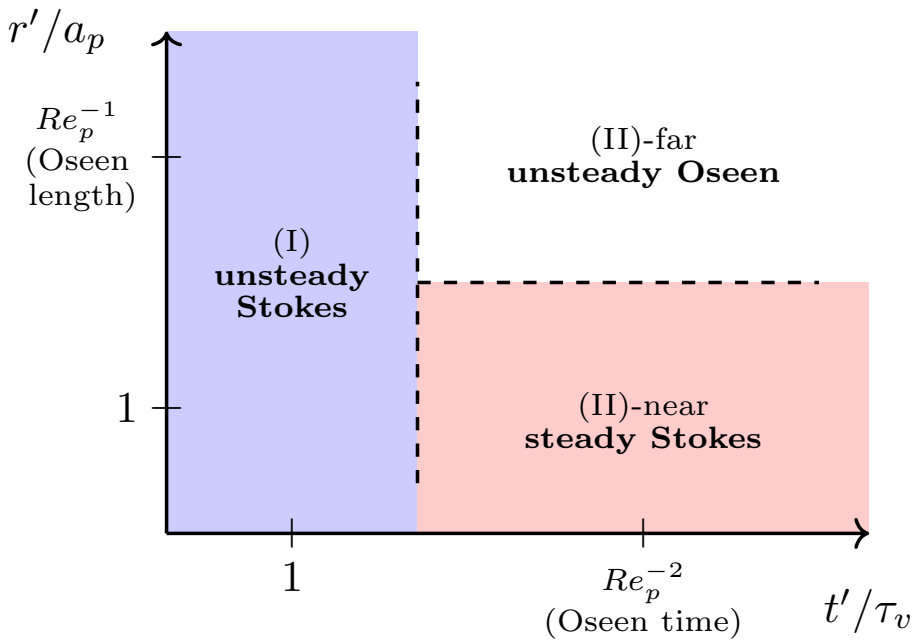

Figure 1.2: Schematic of *leading-order* flow physics in the spatio-temporal landscape around a moving particle perturbing a quiescent flow in viscosity-dominated conditions ($0 < Re_p \ll 1$), with no externally imposed time or length scales beyond those inherent to the dynamics. Here, a_p denotes the particle's radius, and $\tau_v = a_p^2/\nu$ denotes the time taken for particle-induced vorticity to diffuse over particle's size. Region (I) corresponds to early-time dynamics with spatially homogeneous physics, uniformly described by the unsteady Stokes equation. Region (II) corresponds to late-time dynamics, characterized by spatial heterogeneity in the flow physics in the near and far fields. The boundaries between the regions are not as well-defined as the dashed lines used for representation might indicate–they are separated by a continuum of length and time scales. This representation is adapted from [1] and [2].

various scales becomes increasingly complex in multiscale processes such as turbulence.

Nevertheless, for processes with low Reynolds numbers, the early or short-time dynamics are well-described by the unsteady Stokes model. The extent to which this model remains valid at later times depends on the magnitude of the relevant Reynolds numbers. Smaller inertial scale Reynolds numbers extend the early-time diffusive regime governed by the unsteady Stokes model, prolonging its applicability.

We focus on the unsteady Stokes regime hereon, bearing in mind the above factors that control its validity. In the next few subsections in this chapter, we briefly review some preliminaries of the unsteady Stokes equation.

1.1.2 Fundamental solution: the unsteady Stokeslet

We review the fundamental solution for the three-dimensional unsteady Stokes equation to gain insights into far-field behavior and highlight key differences from the steady Stokes problem. Although both problems are linear, the steady Stokes problem is characterized by the Laplace equation, whereas the unsteady counterpart by the modified Helmholtz equation. In this subsection, we also introduce the Laplace and Fourier transform conventions used throughout this thesis.

We seek a rotationally invariant fundamental solution (the *Green's function*) to the unsteady Stokes operator in $\mathbb{R}^3$. We write the fundamental solution as $\boldsymbol{v}_\delta = \boldsymbol{f}_\delta \cdot \mathbb{G}(\boldsymbol{x}, t)$ and $p_\delta = \boldsymbol{f}_\delta \cdot \boldsymbol{\Pi}(\boldsymbol{x}, t)$. We look for $(\mathbb{G}, \boldsymbol{\Pi})$ that solves the unsteady Stokes flow due to a constant point force $\boldsymbol{f}_\delta$ applied at the origin $\boldsymbol{x} = \boldsymbol{0}$ (chosen arbitrarily), acting impulsively at $t = 0$:

$$\frac{\partial \mathbb{G}}{\partial t} = -\boldsymbol{\nabla}\boldsymbol{\Pi} + \boldsymbol{\nabla}^2\mathbb{G} + \mathbb{I}\delta(\boldsymbol{x})\delta(t) \ , \ \boldsymbol{\nabla} \cdot \mathbb{G} = 0 \ , \tag{1.11}$$

where $\mathbb{I}$ is the 3×3 identity matrix, δ is the Dirac delta 'function' satisfying the identity $\int_{\mathbb{R}^3} \delta(\boldsymbol{r}) d\boldsymbol{r} = 1$ for space-like argument and $\int_{\mathbb{R}^+} \delta(t) dt = 1$ for time-like argument. The tensor $\mathbb{G}$ is also known as the *unsteady Stokeslet*. We recall that $\mathbb{G}$ is a tensor, and $\boldsymbol{\Pi}$ a vector.

Taking the Laplace transform with respect to time, the equation becomes:

$$s\tilde{\mathbb{G}} = -\boldsymbol{\nabla}\tilde{\boldsymbol{\Pi}} + \boldsymbol{\nabla}^2\tilde{\mathbb{G}} + \mathbb{I}\delta(\boldsymbol{x}) \ , \ \boldsymbol{\nabla} \cdot \tilde{\mathbb{G}} = 0 \ , \tag{1.12}$$

where s is the Laplace variable, and the tilde denotes the Laplace transform defined according to the following transform pair-

$$\tilde{(\cdot)}(*, s) = \int_0^\infty e^{-st}(\cdot)(*, t)\, dt \ , \ (\cdot)(*, t) = \frac{1}{2\pi i}\int_{\mathcal{L}_B} e^{st}\tilde{(\cdot)}(*, s)\, ds \ ,$$

where $\mathcal{L}_B$ is the standard Bromwich contour in the complex-s space. One may note the structural similarity of eq. (1.12) for $\tilde{\mathbb{G}}$ to the modified Helmholtz equation. Using the Fourier transform in eq. (1.12), we solve for the transformed variables:

$$\hat{\tilde{\boldsymbol{\Pi}}}(\boldsymbol{k}, s) = -i\frac{\boldsymbol{k}}{k^2} \ , \ \hat{\tilde{\mathbb{G}}}(\boldsymbol{k}, s) = \frac{\mathbb{I} - \frac{\boldsymbol{k}\boldsymbol{k}}{k^2}}{k^2 + s} \tag{1.13}$$

where $k = |\boldsymbol{k}|$ and the hatted variables are Fourier transforms defined as

$$\hat{(\cdot)}(\boldsymbol{k}, *) = \int_{-\infty}^\infty e^{-i\boldsymbol{k}\cdot\boldsymbol{x}}(\cdot)(\boldsymbol{x}, *)\, d\boldsymbol{x} \ , \ (\cdot)(\boldsymbol{x}, *) = \frac{1}{(2\pi)^3}\int_{\mathbb{R}^3} e^{i\boldsymbol{k}\cdot\boldsymbol{x}}\hat{(\cdot)}(\boldsymbol{k}, *)\, d\boldsymbol{k} \ .$$

Inverting the Fourier transform gives the unsteady Stokeslet in Laplace space:

$$\begin{aligned}\tilde{\mathbb{G}}(\boldsymbol{x}, s) = &\frac{1}{4\pi s r^3}\left\{(1 + r\sqrt{s} + r^2 s)e^{-r\sqrt{s}} - 1\right\}\left(\mathbb{I} - \frac{\boldsymbol{x}\boldsymbol{x}}{r^2}\right) \\ &+ \frac{1}{2\pi s r^3}\left\{1 - (1 + r\sqrt{s})e^{-r\sqrt{s}}\right\}\frac{\boldsymbol{x}\boldsymbol{x}}{r^2} \ ,\end{aligned} \tag{1.14}$$

where $|\boldsymbol{x}| = r$. In the interest of assessing only the spatial decay properties, we don't perform Laplace inverse transform. For comparison, we recall the fundamental solution to the steady Stokes problem here [23]:

$$\mathbb{G}_{\text{steady}}(\boldsymbol{x}) = \frac{1}{8\pi r}\left(\mathbb{I} + \frac{\boldsymbol{x}\boldsymbol{x}}{r^2}\right) \ .$$

We note the difference in the far-field behavior of the two fields: as $r \to \infty$, we have $\mathbb{G}_{\text{steady}} \sim \mathcal{O}(1/r)$, whereas $\mathbb{G} \sim \mathcal{O}(1/r^3)$. The fast decay of the unsteady Stokeslet guarantees well-defined integrals in the symmetry relation that we discuss in the following section 1.1.3. Further, it estimates a smaller radius of influence, meaning other particles–or more generally surfaces–must be much closer to feel the hydrodynamic interaction effects.

An advantage of the fundamental solution is that a suitable modification of it may serve as a reference known solution when constructing general solution for the unsteady Stokes equation in scenarios subject to other initial and boundary conditions.

1.1.3 Reciprocal theorem for unsteady Stokes equation

For particle's motion in the unsteady Stokes regime, the quantity of interest is the following hydrodynamic force, as seen in eq. (1.1), written here in nondimensional form,

$$\boldsymbol{f}_H(\boldsymbol{x}, t) = \oint_{\boldsymbol{x}\in\partial\mathcal{V}} \boldsymbol{\sigma}(\boldsymbol{v}(\boldsymbol{x}, t), p(\boldsymbol{x}, t)) \cdot \boldsymbol{n}\, dS(\boldsymbol{x}) \ .$$

This is an integrated quantity: the surface traction $\boldsymbol{\sigma} \cdot \boldsymbol{n}$ is integrated over the particle's surface. This may be conventionally determined by exactly solving for the underlying flow field first, $(\boldsymbol{v}, p)$, and then constructing the stress tensor. However, this approach may not be feasible for all boundary and initial conditions. In this subsection, we review a symmetry relation, called the *Lorentz Reciprocal theorem* [23, 24], for the unsteady Stokes equation that provides direct access to this integrated quantity, circumventing the need to solve exactly for the field.

The Reciprocal theorem is an analogue of Green's second identity. It is derived using the divergence theorem, yielding an integral relation between two fields satisfying identical partial differential equation (PDE) in the same domain, differing in boundary and initial conditions.

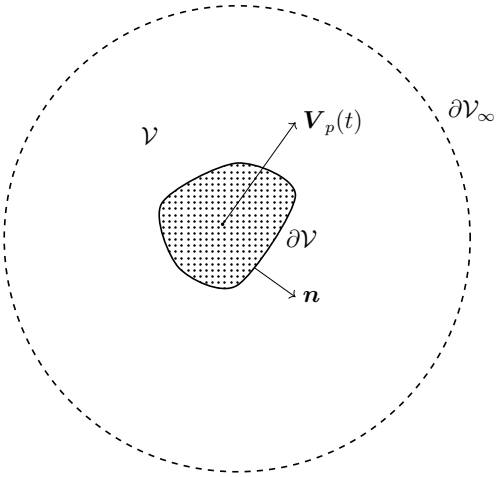

Figure 1.3: Schematic showing an arbitrarily-shaped particle (dotted region) and the domain exterior to the particle, $\mathcal{V}$, where the fluid is present and follows the unsteady Stokes dynamics. The surface bounding the particle is $\partial\mathcal{V}$ and $\boldsymbol{n}$ is the unit vector normal to this surface.

Consider two incompressible (dimensionless) flow fields $(\boldsymbol{v}^{(1)}, p^{(1)})$ and $(\boldsymbol{v}^{(2)}, p^{(2)})$, each supported in the volume $\mathcal{V}$ exterior to an arbitrarily shaped particle (see fig. 1.3). Let $\boldsymbol{\sigma}^{(1)}$ and $\boldsymbol{\sigma}^{(2)}$ denote the corresponding stress tensors. Suppose that both these fields satisfy the unsteady Stokes equation, eq. (1.9), distinguished by different boundary conditions on the bounding particle surface $\partial\mathcal{V}$ and initial conditions. Further, we assume these fields vanish with sufficient decay rate at $\partial\mathcal{V}_\infty$ at infinity.

We follow the steps used in deriving Green's second identity. We take the inner product of the first field $\boldsymbol{v}^{(1)}$ with the unsteady Stokes equation for the second field $\boldsymbol{v}^{(2)}$ and subtract the inner product of $\boldsymbol{v}^{(2)}$ with the equation for $\boldsymbol{v}^{(1)}$, following which we integrate over the exterior fluid volume to get,

$$\int_{\boldsymbol{x}\in\mathcal{V}} \left(\boldsymbol{v}^{(1)} \cdot \frac{\partial \boldsymbol{v}^{(2)}}{\partial t} - \boldsymbol{v}^{(2)} \cdot \frac{\partial \boldsymbol{v}^{(1)}}{\partial t}\right) dV(\boldsymbol{x}) = \int_{\boldsymbol{x}\in\mathcal{V}} \left(\boldsymbol{v}^{(1)} \cdot \boldsymbol{\nabla}\boldsymbol{\sigma}^{(2)} - \boldsymbol{v}^{(2)} \cdot \boldsymbol{\nabla}\boldsymbol{\sigma}^{(1)}\right) dV(\boldsymbol{x}) \ , \quad (1.15)$$

where $dV(\boldsymbol{x})$ is the volume measure in the vector space $\boldsymbol{x}$ corresponding to $dS(\boldsymbol{x})$.

One can show the following relation for an incompressible Newtonian fluid using integration by parts [23]:

$$\boldsymbol{v}^{(1)} \cdot \boldsymbol{\nabla}\boldsymbol{\sigma}^{(2)} - \boldsymbol{v}^{(2)} \cdot \boldsymbol{\nabla}\boldsymbol{\sigma}^{(1)} = \boldsymbol{\nabla} \cdot (\boldsymbol{v}^{(1)} \cdot \boldsymbol{\sigma}^{(2)}) - \boldsymbol{\nabla} \cdot (\boldsymbol{v}^{(2)} \cdot \boldsymbol{\sigma}^{(1)}) \ .$$

Substituting the above on the right-hand side in eq. (1.15), followed by invoking the diver-

gence theorem, we get the following final integral form:

$$\int_{\boldsymbol{x}\in\mathcal{V}} \left(\boldsymbol{v}^{(1)}(\boldsymbol{x},t)\cdot\frac{\partial \boldsymbol{v}^{(2)}(\boldsymbol{x},t)}{\partial t} - \boldsymbol{v}^{(2)}(\boldsymbol{x},t)\cdot\frac{\partial \boldsymbol{v}^{(1)}(\boldsymbol{x},t)}{\partial t}\right) dV(\boldsymbol{x}) \\ = \oint_{\boldsymbol{x}\in\partial\mathcal{V}} \left(\boldsymbol{v}^{(1)}(\boldsymbol{x},t)\cdot\boldsymbol{\sigma}^{(2)}\cdot(-\boldsymbol{n}) - \boldsymbol{v}^{(2)}(\boldsymbol{x},t)\cdot\boldsymbol{\sigma}^{(1)}\cdot(-\boldsymbol{n})\right) dS(\boldsymbol{x}) \ , \tag{1.16}$$

where the integral on the right-hand side of the relation is over the particle's surface (a dimensional reduction!). Note that the integral over $\partial\mathcal{V}_\infty$ is absent due to the assumed decay properties of the integrand. This is the statement of the Lorentz Reciprocal theorem for the unsteady Stokes equation, applicable for arbitrarily shaped particle. We shall, however, consider the particular case of spherical particle for our applications. In applications, $(\boldsymbol{v}^{(1)}, p^{(1)})$ is the primary field corresponding to the conditions of interest, whereas the auxiliary field $(\boldsymbol{v}^{(2)}, p^{(2)})$ is assumed known.

The above sequence of operations (eqs. (1.15) and (1.16)) can be repeated, starting from the unsteady Stokes equations in the Laplace space instead, to derive the following relation, which corresponds to eq. (1.16) for the Laplace-transforms of the field variables:

$$\int_{\boldsymbol{x}\in\mathcal{V}} \left(\tilde{\boldsymbol{v}}^{(2)}(\boldsymbol{x},s)\cdot\boldsymbol{v}^{(1)}(\boldsymbol{x},0) - \tilde{\boldsymbol{v}}^{(1)}(\boldsymbol{x},s)\cdot\boldsymbol{v}^{(2)}(\boldsymbol{x},0)\right) dV(\boldsymbol{x}) \\ = \oint_{\boldsymbol{x}\in\partial\mathcal{V}} \left(\tilde{\boldsymbol{v}}^{(1)}(\boldsymbol{x},s)\cdot\tilde{\boldsymbol{\sigma}}^{(2)}\cdot(-\boldsymbol{n}) - \tilde{\boldsymbol{v}}^{(2)}(\boldsymbol{x},s)\cdot\tilde{\boldsymbol{\sigma}}^{(1)}\cdot(-\boldsymbol{n})\right) dS(\boldsymbol{x}) \ . \tag{1.17}$$

Note that by choosing the auxiliary field $\tilde{\boldsymbol{v}}^{(2)}$ with desirable initial and boundary conditions, the integral of surface traction due to the primary field $\tilde{\boldsymbol{v}}^{(1)}$ can be extracted. The above form of the Reciprocal relation is used in deriving equation of motion for the particle in a flow, discussed in the upcoming section 1.1.4.

The unsteady Stokeslet from eq. (1.11) can be modified for a singular source placed in the exterior $\mathcal{V}$ (instead of $\boldsymbol{x} = 0$) to serve as the auxiliary field, and obtain an integral expression for the primary velocity field $\boldsymbol{v}^{(1)}$ subject to desired conditions. This forms the basis for fast numerical methods based on such integral solution representations (see [25, 26] for example). The Reciprocal identity finds wider applications in other low-Reynolds number flows, for instance, [27] uses a modification of the identity to explore fluids with odd viscosity and [28] uses it in active Stokesian suspensions. We refer to [24] for a detailed review of the reciprocal theorem and its various applications. However, we note here that the utility of the symmetry relation relies on a known solution that serves as the auxiliary field, which may be infeasible in some cases, especially for multi-particle systems.

1.1.4 Hydrodynamic force on inertial particle in Stokesian regime

So far, we addressed the dominant fluid dynamics around the moving particle. In this subsection, we discuss the hydrodynamic force that a particle experiences as a result while it moves through a background flow field $\boldsymbol{u}'^{\infty}$ in the unsteady Stokes regime. Using the tools discussed so far, we outline the derivation for the particle's equation of motion following [29–31].

Assuming the particle induces only a small perturbation, the (dimensional) perturbed fluid field can be decomposed as,

$$\begin{aligned}
\boldsymbol{v}'(\boldsymbol{x}',t') &= \boldsymbol{u}'^{\infty}(\boldsymbol{x}',t') + \Big(\boldsymbol{v}'(\boldsymbol{x}',t') - \boldsymbol{u}'^{\infty}(\boldsymbol{x}',t')\Big) \equiv \boldsymbol{u}'^{\infty}(\boldsymbol{x}',t') + \boldsymbol{v}'_p(\boldsymbol{x}',t') \ , \\
p'(\boldsymbol{x}',t') &= p'^{\infty}(\boldsymbol{x}',t') + \Big(p'(\boldsymbol{x}',t') - p'^{\infty}(\boldsymbol{x}',t')\Big) \equiv p'^{\infty}(\boldsymbol{x}',t') + p'_p(\boldsymbol{x}',t') \ ,
\end{aligned}$$

where $\boldsymbol{v}'_p := (\boldsymbol{v}' - \boldsymbol{u}'^{\infty})$ represents the small disturbance induced by the particle on the free-space background field $\boldsymbol{u}'^{\infty}$. Correspondingly, owing to the linear dependence of the stress tensor on the velocity field for a Newtonian fluid, the stress field and the hydrodynamic force follow identical decomposition:

$$\begin{aligned}
&\boldsymbol{\sigma}'(\boldsymbol{v}',p') = \boldsymbol{\sigma}'(\boldsymbol{u}'^{\infty},p'^{\infty}) + \boldsymbol{\sigma}'(\boldsymbol{v}'-\boldsymbol{u}'^{\infty},p'-p'^{\infty}) \equiv \boldsymbol{\sigma}'^{\infty} + \boldsymbol{\sigma}'_p \ , \\
\implies &\boldsymbol{f}'_H(\boldsymbol{x}',t') = \oint_{\partial\mathcal{V}} \boldsymbol{\sigma}'\cdot\boldsymbol{n}\, dS = \oint_{\partial\mathcal{V}} \boldsymbol{\sigma}'^{\infty}\cdot\boldsymbol{n}\, dS + \oint_{\partial\mathcal{V}} \boldsymbol{\sigma}'_p\cdot\boldsymbol{n}\, dS
\end{aligned} \tag{1.18}$$

The Navier-Stokes equations for the decomposed fields can be written as follows:

$$\rho_f\Big(\frac{\partial \boldsymbol{u}'^{\infty}}{\partial t'} + \boldsymbol{u}'^{\infty}\cdot\boldsymbol{\nabla}'\boldsymbol{u}'^{\infty}\Big) = \boldsymbol{\nabla}'\cdot\boldsymbol{\sigma}'^{\infty} \ , \tag{1.19a}$$

$$\rho_f\Big(\frac{\partial \boldsymbol{v}'_p}{\partial t'} + \boldsymbol{u}'^{\infty}\cdot\boldsymbol{\nabla}'\boldsymbol{v}'_p + \boldsymbol{v}'_p\cdot\boldsymbol{\nabla}'\boldsymbol{u}'^{\infty} + \boldsymbol{v}'_p\cdot\boldsymbol{\nabla}\boldsymbol{v}'_p\Big) = \boldsymbol{\nabla}'\cdot\boldsymbol{\sigma}'_p \ , \tag{1.19b}$$

along with their respective divergence-free conditions.

The contribution of the *known* free-space ambient flow field $\boldsymbol{u}'^{\infty}$ to the hydrodynamic force on the particle can be inferred from eq. (1.19a) as follows,

$$\oint_{\boldsymbol{x}'\in\partial\mathcal{V}} \boldsymbol{\sigma}'^{\infty}\cdot\boldsymbol{n}\, dS(\boldsymbol{x}') = \int_{\boldsymbol{x}'\in\mathbb{R}^3\setminus\mathcal{V}} \boldsymbol{\nabla}'\cdot\boldsymbol{\sigma}'^{\infty}\, d\boldsymbol{x}' \approx \frac{4}{3}\pi a_p^3\rho_f \frac{D\boldsymbol{u}'^{\infty}}{Dt'}\bigg|_{\boldsymbol{x}'=\boldsymbol{X}'_p(t')} \ , \tag{1.20}$$

where the final approximation is made assuming the quantity $D\boldsymbol{u}'^{\infty}/Dt'$ is almost uniform in the volume occupied by the particle, $\mathbb{R}^3\setminus\mathcal{V}$. Therefore, assuming smoothness of $\boldsymbol{u}'^{\infty}$, we use Taylor series expansion for the material derivative in the neighborhood of the instantaneous

center of the moving particle for sufficiently small particle size a_p compared to a characteristic length scale in the ambient flow, retaining only the leading-order term in eq. (1.20), given by its value at the particle's instantaneous center. Higher-order correction terms, dependent on gradients of $\boldsymbol{u}'^{\infty}$, have been consistently derived in [32].

Now, we focus on the remaining contribution from the *unknown* evolving perturbation field, $\boldsymbol{v}'_p$. Following the non-dimensionalisation procedure in section 1.1.1 with similar choice of characteristic scales, $L_c = a_p,\ P_c = \mu U_c/a_p$, eq. (1.19b) reduces to the following unsteady Stokes equation at the leading-order in the small particle Reynolds number parameter[4] with modified boundary conditions,

$$\rho_f \frac{\partial \boldsymbol{v}'_p}{\partial t'} = \boldsymbol{\nabla}' \cdot \boldsymbol{\sigma}'_p \ , \tag{1.21a}$$

$$\boldsymbol{\nabla}' \cdot \boldsymbol{v}'_p = 0 \ , \tag{1.21b}$$

$$\boldsymbol{v}'_p(\boldsymbol{x}', 0) = \boldsymbol{v}'_0(\boldsymbol{x}') - \boldsymbol{u}'^{\infty}(\boldsymbol{x}', 0) \ , \tag{1.21c}$$

$$\boldsymbol{v}'_p(\boldsymbol{x}', t') = \boldsymbol{V}'_p(t') - \boldsymbol{u}'^{\infty}(\boldsymbol{x}', t') \ \text{ on the particle's surface} \ , \tag{1.21d}$$

$$\boldsymbol{v}'_p(\boldsymbol{x}', t') \to \boldsymbol{0} \ , \ p'_p(\boldsymbol{x}', t') \to 0 \ \text{ as } |\boldsymbol{x}' - \boldsymbol{X}'_p(t)| \to \infty \ , \tag{1.21e}$$

Evaluating the contribution from the *unknown* perturbation field $\boldsymbol{v}_p{}'$ is more involved and requires solving eq. (1.21). Following [29, 30], we apply the Reciprocal Theorem in the Laplace space (eq. (1.17)) with $\boldsymbol{v}^{(1)} = \boldsymbol{v}'_p$ and choose an appropriate auxiliary field, $\boldsymbol{v}^{(2)}$. For $\boldsymbol{v}^{(2)}$, Maxey and Riley [29] used a flow resulting from an impulsively-started rigid sphere at $t' = 0$, while Gatignol [30] chose a flow resulting from an oscillating sphere as the auxiliary field. Both choices yield the following expression for the hydrodynamic force due to $\boldsymbol{v}'_p$:

$$\begin{aligned}\oint_{\boldsymbol{x}' \in \partial\mathcal{V}} \boldsymbol{\sigma}'_p \cdot \boldsymbol{n} \, dS(\boldsymbol{x}') = -6\pi a_p \mu \boldsymbol{w}'(t') - 6\pi a_p^2 \mu \left(\frac{\boldsymbol{w}'(0)}{\sqrt{\pi \nu t'}} + \int_0^{t'} \frac{1}{\sqrt{\pi \nu (t' - \tau')}} \frac{d\boldsymbol{w}'(\tau')}{d\tau'} \, d\tau' \right) \\ - \frac{m_f}{2} \left(\frac{d\boldsymbol{V}'_p(t')}{dt'} - \frac{D\boldsymbol{u}'^{\infty}}{Dt'}(\boldsymbol{X}'_p(t'), t') \right) \ ,\end{aligned} \tag{1.22}$$

where $\boldsymbol{w}'(t') = \boldsymbol{V}'_p(t') - \boldsymbol{u}'^{\infty}(\boldsymbol{X}'_p(t'), t')$ is the *particle slip-velocity* and m_f is the mass of fluid displaced by the particle.

Combining the contributions from the two decomposed fields (eq. (1.20) and eq. (1.22)) for the total hydrodynamic force in eq. (1.1), we obtain the following *integro-differential*

[4] Recall our particle Reynolds number, Re_p, is based on the particle-induced perturbation velocity. The field $\boldsymbol{v}'_p$ emerging from the decomposition here is consistent with this definition.

equation for the particle's translational motion,

$$m_p \frac{d\boldsymbol{V}_p'(t')}{dt'} = \Bigg[-6\pi a_p \mu \boldsymbol{w}'(t') - 6\pi a_p^2 \mu \left(\frac{\boldsymbol{w}'(0)}{\sqrt{\pi\nu t'}} + \int_0^{t'} \frac{1}{\sqrt{\pi\nu(t'-\tau')}} \frac{d\boldsymbol{w}'(\tau')}{d\tau'} \, d\tau' \right) + m_f \frac{D\boldsymbol{u}'^{\infty}}{Dt'}\Bigg|_{\boldsymbol{x}'=\boldsymbol{X}_p'(t')} - \frac{m_f}{2}\left(\frac{d\boldsymbol{V}_p'(t')}{dt'} - \frac{D\boldsymbol{u}'^{\infty}}{Dt'}(\boldsymbol{X}_p'(t'),t') \right) \Bigg] + \boldsymbol{f}_{\mathrm{NH}}'(\boldsymbol{X}_p'(t'),t') \ , \tag{1.23}$$

This is the *Maxey-Riley-Gatignol* (MRG) equation[5], also commonly known as the *Maxey-Riley* equation, where the Faxén correction terms which account for local curvature of the flow field are omitted ($\sim \boldsymbol{\nabla}'^2 \boldsymbol{u}'^{\infty}$), assuming $a_p \ll L^{\infty}$, where L^{∞} is some characteristic length scale of the ambient flow (see [29] for the Faxeń corrections). According to eq. (1.23), the hydrodynamic force under unsteady Stokes theory includes four contributions in the order that they appear in the square parenthesis: the *quasi-steady Stokes* drag, the nonlocal *Basset-Boussinesq history* (BBH) force, the inertial force from the ambient flow acceleration, and the *added mass* due to particle acceleration.

1.2 Motivation and Organization of thesis

Parts of this subsection are taken from the published article titled '*The Basset-Boussinesq history force: its neglect, validity, and recent numerical developments*' [Jaganathan *et al.*, Front. Phys. (2023)]. I acknowledge my co-authors on it for their contributions.

We have seen that accounting for finite-time response of the fluid warrants an *unsteady* Stokes theory, which is fundamentally different from its steady counterpart in a number of ways. An immediate consequence is the emergence of a nonlocal force on the particle called the *Basset-Boussinesq history force* in addition to the standard Stokes drag, leading to an integro-differential equation of motion governing the particle's motion eq. (1.23).

Previous analytical and experimental works have reported notable qualitative differences when the BBH force is neglected in the inertial particle model even in the simplest scenarios; a small sphere in a quiescent fluid, either relaxing freely (no external forcing) or approaching terminal velocity under gravity, does so algebraically when the BBH force is included [34–37] as opposed to exponentially when excluded. This algebraic behavior is consistent with short-time experimental observations made by [38] on a sphere settling under gravity. Similarly, a colloidal particle in fluid displaying long-time tails in velocity auto-correlations [39, 40] is supported in theory by inclusion of the history force [41–44]. A marginally heavy particle

[5]Gatignol in [30] additionally also provides the torque equation.

in a simulation without the BBH force is ejected from a solid-body vortex more rapidly than observed in experiment [45, 46], whereas inclusion of the BBH force provides better agreement with experiment. Exceptionally, [47] reported that while certain aspects of the dynamics of neutrally-buoyant particles in chaotic flow observed by [48] are predicted by the MRG equation, any deterministic force including the BBH force is inadequate to capture random fluctuations.

Numerical studies too have highlighted the role of the BBH force in particle dynamics in turbulent flows [49–59]. The main conclusions of these studies are (*i*) particle clustering and caustics formation are strongly reduced by the BBH force; (*ii*) in a typical chaotic flow without external forcing, particle attractors are *less typical* in the presence of the BBH force for light particles and the basin of attractions where particulate matter tends to aggregate shrinks irrespective of the particle's Stokes number (ratio of particle relaxation timescale to flow timescale). Convergence to the attractors that remain is algebraically slower with BBH as opposed to exponential convergence in its absence; however, (*iii*) several statistical properties of particles remain unchanged. For example, the standard deviation σ of trajectories of a collection of sedimenting particles scales as ballistic, $\sigma^2 \sim t^2$ for short times and diffusive, $\sigma^2 \sim t$ for long times both with and without the BBH force. Nevertheless, individual trajectories of the particles show deviation. Yet, as Haller in [60] summarizes the collective viewpoint, the BBH force "is notoriously difficult to handle", which prompts most studies to ignore this term despite ample numerical and experimental evidence of its significance. The challenges posed by the BBH force and thereby the MRG equation are largely due to its nonlocal nature and are discussed in detail in section 3.1.2.

The work in this thesis explores aspects of inertial particle transport in unsteady environments and is motivated by the following broad questions:

- What is the unsteady Stokes flow model for a single particle? How is it fundamentally different from its well-known steady counterpart? How do memory effects emerge?
- Accounting for memory effects results in an integro-differential equation for the particle's motion. How can we construct an equivalent memoryless framework which lends itself to an efficient numerical method with time-independent computational cost?
- How do the memory effects influence the dynamics of inertial particles in vortical flows? Can inertial particles cluster and get trapped indefinitely in such flows?
- What is a minimal particle-particle interaction model in the unsteady Stokesian regime?

The rest of the thesis is organized as follows: in chapter 2, we examine the unsteady Stokes model in a simple sedimentation experiment, containing a rigid sphere settling under gravity

in a viscous fluid. Due to its finite inertia, the sphere undergoes perceivable unsteady settling dynamics before reaching a steady state. Our objective is to characterize this transient behavior and demonstrate that the unsteady Stokes model reliably describes the observed motion and flow structures, whereas the steady Stokes model is found lacking. Experiments conducted under controlled Stokesian conditions by our collaborators at *Stanford University* show good agreement between the sphere's trajectory and predictions from the *Maxey-Riley-Gatignol* equation for $Re_p < 1$. While the unsteady Stokes model captures flow structures accurately for very small Re_p, deviations appear at larger $Re_p < 1$, highlighting the theory's limitations as indicated by scale analysis in section 1.1.1.

In chapter 3, we address the *Maxey-Riley-Gatignol* (MRG) equation, which governs the motion of a sphere in nonuniform flow under unsteady Stokes conditions. The equation includes the nonlocal BBH force, an integral along the particle's trajectory. Closed-form solutions exist only for specific cases, such as unidirectional sedimentation in quiescent ambient flow, addressed in chapter 2. For more general nonuniform flows, numerical methods are required due to the nonlinear dependence on the particle's position. However, solving the MRG equation numerically is challenging because of the growing memory effect of the BBH force. To address this, we develop a memoryless framework using a *Markovian embedding procedure*, which forms the basis of our explicit time-integrator scheme, which is a generalization of the *exponential time-differencing method* [3] to nonlocal equations, significantly reducing the computational cost of solving the MRG equation.

In chapter 4, we use the explicit MRG integrator from chapter 3 to study inertial particle trapping and clustering tendencies, a precursor to inter-particle collisions critical for various physical phenomena, near a pair of co-rotating vortices, which is a canonical structure in typical 2D turbulent flows. Common wisdom suggests that particles denser than the suspending fluid centrifuge out of vortical flow regions and cluster in high-strain regions [61–64]. However, particles in a rotating system of vortices can get indefinitely trapped in attracting fixed points and orbits near the vortices in the rotating frame of reference. We find an enhanced clustering tendency for inertial particles, especially under the memory effects of the BBH force.

In chapter 5, we describe a minimal hydrodynamic interaction model for multiple particles in a viscous fluid. Our long-term objective is to generalize the MRG model to multi-particle scenarios, focusing on particle interactions mediated by the fluid within the unsteady Stokesian regime. This involves studying the unsteady Stokes equation in a time-dependent domain where particle motion depends on fluid flow. In this chapter, we consider a simpler problem first: the unsteady Stokes equation in a stationary, 2D multiply-connected domain, which poses many of the main challenges of the time-dependent domain problem.

Chapter 6 may appear thematically different from the rest of the chapters, since it doesn't primarily concern particle-laden flows. However, the systems we discuss here evolve according to an integro-differential equation like the MRG equation. The analytical work in this chapter is derived from the ideas used for the MRG equation. We describe a generalization of the Markovian embedding procedure to a broader class of nonlocal evolutionary equations which have *nonlinear dependence* on past values of the evolving quantity. We use two physical equations, namely the integro-differential equation in the 1D stroboscopic model for a walking droplet [65] and the Volterra integral equation that governs the motion of a melting front in the idealized single-phase Stefan problem [66], to demonstrate the embedding procedure.

Finally, we conclude in chapter 7 with pertinent discussions and an outlook for future work.

Chapter 2

A sphere settling under gravity in a quiescent fluid

This chapter is based on the article titled *Basset-Boussinesq history force and inertia are relevant for unsteady particle settling dynamics* [Jaroslawski *et al.*, arXiv:2408.12530]. The experiments were carried out by co-authors Tomek Jaroslawski and Prof. Beverley McKeon. Sections 2.3 and 2.4 are largely reproduced verbatim from this article. I acknowledge the contributions of all the co-authors. I primarily contributed to the theoretical modeling.

2.1 Introduction

The gravitational settling of particles in a viscous medium is an important aspect of several environmental and industrial transport processes, such as settling of aerosol particles in turbulent air [68], deposition of clay and silt in the oceans [69], and settling of ice particles in cloud [70]. Understanding the short-time dynamics of these settling particles is crucial for predicting transient behaviors like pollutant residence times, and the growth rate of particle/droplet aggregates. Previous studies on gravitational settling have examined the effects of irregular particle shapes [71–73], inter-particle interactions [74, 75], and stratification in the ambient flow [76, 77], among other factors. This chapter presents a simple experiment on the gravitational settling of a rigid sphere to probe the finite-time relaxation of the system to a steady state and compares the observations with theoretical predictions from the unsteady Stokes model.

Despite growing evidence of the history force's significance in short/early-time dynamics of particles and droplets–including theoretical findings of algebraic rather than exponential relaxation rates of particles to their asymptotic states in different physical contexts [16, 46, 78, 79] –accurate experimental observations are scarce, with even fewer studies quantitatively

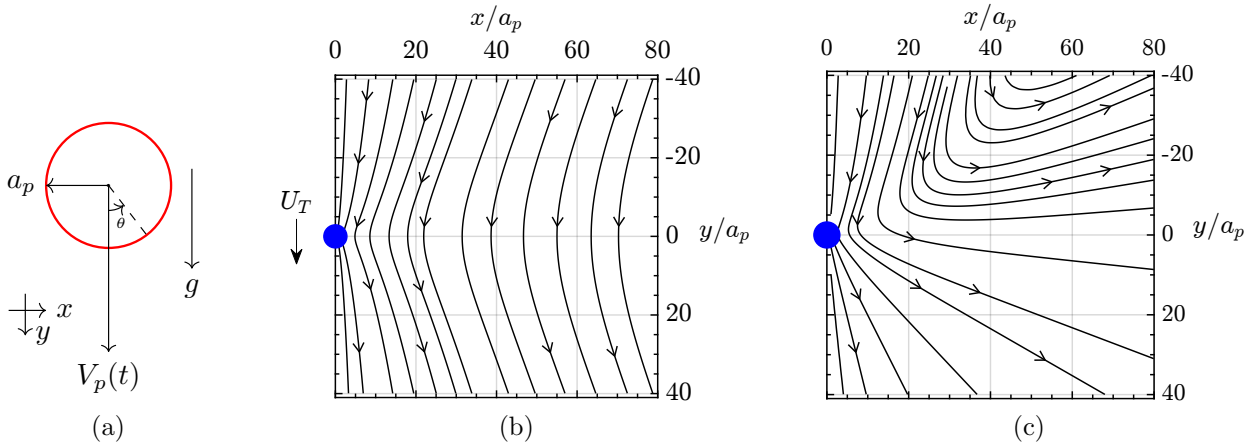

Figure 2.1: (a) Schematic showing the settling sphere, where θ is the polar angle of spherical coordinate system. Streamlines in an axial plane for flow around a rigid sphere in uniform translational motion, when $V_p(t) = U_T$, according to (b) the steady Stokes equation (eq. (2.1)) and (c) the Oseen equation (eq. (2.3)), shown in laboratory frame The sphere, marked by a blue circle (not to scale) at $(0, 0)$, is falling downward under gravity. Note the *fore-aft* symmetry in the steady Stokes model, while the steady Oseen model develops asymmetry.

validating these against theoretical predictions. In addition, the flow field generated by an accelerating particle in such flows remains poorly understood and has rarely been measured.

We consider the simple case of an isolated small rigid sphere of radius a_p and density ρ_p held at rest against gravity. At time $t = 0$, the sphere is released into a highly viscous and otherwise quiescent fluid of density ρ_f and viscosity μ, and falls vertically with velocity $V_p(t)$ under gravity's action (see the schematic fig. 2.1a). Eventually, the sphere reaches its *terminal velocity*, $V_p(t) \to U_T$ as $t \to \infty$, and continues to move at this constant velocity (assuming no new perturbations act on the system); an equilibrium state wherein the sphere experiences as much hydrodynamic resistive force due to the ambient fluid as the combined effect of gravitational force and buoyancy. In the experiments, our collaborators measure the transient dynamics leading up to this steady state, and we demonstrate that the unsteady Stokes model provides a more accurate prediction of the sphere's trajectory and the surrounding flow disturbances than the quasi-steady Stokes theory.

2.1.1 Steady-state theories and quasi-steady models

Before addressing the transient dynamics, we review low Reynolds number theories to describe the steady-state of fluid and particle during gravitational settling. These steady state theories are useful on two accounts: they predict the asymptotic state of the experiment and form the basis for quasi-steady particle models.

In the equilibrium state, the rigid sphere translates steadily with constant terminal velocity in the direction of gravity. For $Re_p = 0$, this scenario can be described by the classical Stokes problem of a sphere in uniform rectilinear motion in a quiescent fluid, first solved by Stokes (1851) [80]. Based on this classical problem, the axisymmetric flow field that develops around the sphere moving with terminal velocity U_T is given by the following steady stream function in spherical coordinate system [15],

$$\psi'_{\text{Stokes}}(\underset{\sim}{\boldsymbol{x}}') = U_T \left(\frac{3}{4}\frac{a_p}{r'} - \frac{1}{4}\frac{a_p^3}{r'^3} \right) r'^2 \sin^2\theta \tag{2.1}$$

where $r' = |\underset{\sim}{\boldsymbol{x}}'| := |\boldsymbol{x}' - \boldsymbol{X}'_p(t')|$ is the dimensional radial coordinate measured from the sphere's instantaneous centre and $\theta \in [0, \pi]$ is the polar angle. The corresponding streamlines, shown in fig. 2.1b, exhibit fore-aft symmetry about the plane perpendicular to U_T.

The hydrodynamic drag on the sphere due to eq. (2.1) is the well-known Stokes drag, $\boldsymbol{f}'_H = -6\pi a_p \mu U_T$, acting in the direction opposite to gravity. This expression has found many successful applications including famously in Millikan's oil drop experiment [81] to determine an electron's electric charge. The sphere's terminal velocity is obtained by balancing Stokes drag with gravitational and buoyancy forces:

$$(m_p - m_f)g - 6\pi a_p \mu U_T = 0 \implies U_T = \frac{2(\rho_p - \rho_f)a_p^2 g}{9\mu} \,, \tag{2.2}$$

where g is the gravitational acceleration.

For small but nonzero Re_p, however, Oseen (1910) [17] criticized the use of eq. (1.8) to describe steady-state flow. He noted that the convective inertia term in the Navier-Stokes eq. (1.4) becomes comparable to the viscous term at far-field, $r' \sim a_p Re_p^{-1}$ (see fig. 1.1), affecting the leading-order balance. Thus, solving the linearized steady Oseen equations for the uniformly moving sphere, that partially accounts for the convective inertia (see [14, 15] for details), Lamb (1911) [82] provided an approximate expression for the steady-state stream function:

$$\psi'_{\text{Oseen}}(\underset{\sim}{\boldsymbol{x}}') = U_T a_p^2 \left[-\frac{1}{4}\frac{a_p}{r'}\sin^2\theta + \frac{3}{2}(1-\cos\theta)\left(\frac{1 - \exp\{-\frac{1}{2}Re_p(1+\cos\theta)r'/a_p\}}{Re_p} \right) \right] . \tag{2.3}$$

The streamlines plotted using the above expression are shown in fig. 2.1c. Consistent with the expression's dependence on $\cos\theta$, which is an odd function of the polar angle, the streamlines show fore-aft asymmetry, reflecting the influence of convective inertia. The corresponding

correction in the hydrodynamic drag force is given by Oseen's drag [83]:

$$\boldsymbol{f}'_H = -6\pi a_p \mu U_T \Big(1 + \frac{3}{8} Re_p + \mathcal{O}(Re_p^2 \log Re_p)\Big) \ . \tag{2.4}$$

Notably, the expression for terminal velocity remains unchanged (eq. (2.2)) to the leading order in Re_p. Depending on the magnitude of Re_p, the above expressions provide predictions for the asymptotic states of the settling particle and flow structures in our experiments.

These steady-state theories can also model fluid's instantaneous response to particle perturbations in the limit $S \to 0$. Such models assume either the Stokes or Oseen's drag (eq. (2.4)) as the hydrodynamic force in eq. (1.1), with U_T replaced by the time-dependent particle velocity $V_p(t)$ in their respective expressions. This results in a simple *quasi-steady Stokes/Oseen* model, without the integral BBH force, that predicts the particle's exponential relaxation rate to its steady state, as the fluid relaxes instantaneously. This, however, is not true for many scenarios.

Now, we turn to the transient dynamics during gravitational settling.

2.2 Theory of an accelerating sphere: the unsteady Stokes model

In this section, we describe the unsteady Stokes model forced by gravity for the transient settling motion of the particle and the flow field that develops around it.

For convenience, we work in the body-fixed frame of reference with nondimensional variables under the following transformation of variables: $\boldsymbol{x} - \boldsymbol{X}_p(t) \to \underset{\sim}{\boldsymbol{x}}$, $\boldsymbol{v} - \boldsymbol{V}_p(t) \to \underset{\sim}{\boldsymbol{v}}$. All the quantities with symbol $\underset{\sim}{(\cdot)}$ are measured in the body-fixed frame, whereas the ones without correspond to laboratory-fixed reference frame. The physical variables are nondimensionalized by characteristic length a_p and time a_p^2/ν. For convenience of interpretation, we choose U_T as the velocity scale. The pressure field is scaled by $\mu U_T/a_p$. The resultant nondimensional equations of motion for the fluid in the body-fixed frame and in the vanishing limit of Reynolds number are:

$$\frac{\partial \underset{\sim}{\boldsymbol{v}}}{\partial t} = -\nabla \underset{\sim}{p} + \nabla^2 \underset{\sim}{\boldsymbol{v}} + \left(\sigma \frac{\boldsymbol{g}}{|\boldsymbol{g}|} - \frac{d\boldsymbol{V}_p}{dt}\right) , \boldsymbol{\nabla} \cdot \underset{\sim}{\boldsymbol{v}} = 0 \ , \ \ \boldsymbol{x} \in \mathcal{V} \ , \tag{2.5a}$$

$$\underset{\sim}{\boldsymbol{v}}(|\underset{\sim}{\boldsymbol{x}}| = 1, t) = \boldsymbol{0} \ , \ \underset{\sim}{\boldsymbol{v}}(|\underset{\sim}{\boldsymbol{x}}| \to \infty, t) = -\boldsymbol{V}_p(t) \ , \ \underset{\sim}{\boldsymbol{v}}(\underset{\sim}{\boldsymbol{x}}, 0) = \boldsymbol{0} \ , \tag{2.5b}$$

where the boundary conditions include no-slip condition at the sphere's surface and decay at far-field, and the initial condition corresponds to a stationary state. Here, $\sigma = 9/[2(\rho_p/\rho_f - 1)]$ is the scaled gravitational acceleration. The uniform acceleration term $d\boldsymbol{V}_p(t)/dt$ in eq. (2.5a) appears as a result of coordinate change.

We assume axisymmetry of the flow field about the axis passing through the sphere's center and parallel to gravity, which is reasonable since the sphere's motion during the experiment is predominantly vertical in the direction of gravity. Hence, owing to incompressibility, we can define as well as solve for a scalar stream function in the body-fixed spherical polar coordinate system to describe the flow structures. The nondimensional axisymmetric stream function $\psi = \psi(r, \theta, t)$ is related to the radial and polar velocity fields by:

$$\underset{\sim}{v}_r(r, \theta, t) = \frac{1}{r^2 \sin\theta} \frac{\partial \psi}{\partial \theta} \ , \ \underset{\sim}{v}_\theta(r, \theta, t) = -\frac{1}{r \sin\theta} \frac{\partial \psi}{\partial r} \ .$$

By taking the curl of eq. (2.5), we eliminate pressure and uniform body forces (see section 2.A for derivation), yielding the governing equation for the unsteady stream function,

$$\left(\frac{\partial}{\partial t} - d^2\right) d^2 \psi(r, \theta, t) = 0 \ , \tag{2.6}$$

subject to conditions

$$\begin{aligned} \psi(1, \theta, t) = 0 = \frac{\partial \psi}{\partial r}(1, \theta, t), \\ \psi(r \to \infty, \theta, t) \sim -\frac{1}{2} r^2 V_p(t) \sin^2\theta \ , \\ \psi(r, \theta, t = 0) = 0 \ , \end{aligned} \tag{2.7}$$

where the scalar operator d^2 is

$$d^2 = \frac{\partial^2}{\partial r^2} + \frac{\sin\theta}{r^2} \frac{\partial}{\partial \theta} \frac{1}{\sin\theta} \frac{\partial}{\partial \theta} \ .$$

The Dirichlet condition, $\psi(1, \theta, t) = 0$, enforces zero radial velocity on the sphere's surface, whereas the radial direction Neumann condition enforces zero polar velocity.

Remark 2.1. The governing equation eq. (2.6) describes the unsteady stream function in all scenarios where eq. (2.5) is driven by a uniform or, more generally, a curl-free force. Such forces do not affect flow kinematics, and thus the flow structures represented by the streamlines remain unchanged.

The linear PDE system given by eq. (2.6) and eq. (2.7) is solved using Laplace transform (see section 2.A), yielding the following exact expression for the nondimensional unsteady stream function (scaled by $a_p^2 U_T$),

$$\psi(r, \theta, t) = \sin^2\theta \left[\left(-\frac{r^2}{2} + \frac{1}{2r} \right) V_p(t) + \frac{3}{2r} \int_0^t V_p(\tau) K(t - \tau; r) \, d\tau \right] \ , \tag{2.8}$$

where the flow memory kernel is

$$K(z;c) = \left(\frac{1 - ce^{-\frac{(c-1)^2}{4z}}}{\sqrt{\pi z}} + \mathrm{erf}\Big\{ \frac{(c-1)}{2\sqrt{z}} \Big\} \right), \ z > 0, \ c > 1 \ .$$

The stream function in the laboratory-fixed frame is recovered by removing the spatially uniform flow part (the term proportional to r^2) from the above expression, resulting in

$$\psi(r,\theta,t) = \sin^2\theta \left[\frac{1}{2r} V_p(t) + \frac{3}{2r} \int_0^t V_p(\tau) K(t-\tau; r)\, d\tau \right] . \tag{2.9}$$

The above time-dependent expression for the unsteady stream function is fundamentally different from the steady stream function in eq. (2.1). It consists of two components: one depends on the particle's instantaneous velocity, while the other integrates the particle's velocity over its lifetime. This generalizes the expressions in [1, 25][1] to a sphere moving with arbitrary time-dependent velocity. The time integral in eq. (2.9) represents the history/memory effect: a 'superposition' of decaying flow perturbations generated by the sphere along its trajectory on the present state, sustained due to fluid's finite-time relaxation.

Figure 2.2 shows representative snapshots of the unsteady streamlines in response to a prescribed velocity of sphere, qualitatively mimicking the settling sphere's velocity for an arbitrary set of parameters. A notable prediction of this theory is the vortex formation at the sphere's accelerating surface, which drifts away over time while exhibiting fore-aft symmetry. In contrast, there is no vortex formation in the steady Stokes theory (see fig. 2.1b).

So far, we have looked at the fluid dynamics resulting from an arbitrarily accelerating sphere, which also applies to gravitational settling. We now focus on the exact dynamics of the settling sphere when coupled to the unsteady Stokes flow. The trajectory of the settling sphere, when $\boldsymbol{V}_p'(0) = \boldsymbol{0}$, is given by the *Basset-Boussinesq-Oseen (BBO) equation* [84], which implicitly accounts for the effects of the unsteady Stokes flow. The BBO equation is a reduced form of the gravity-forced MRG equation for a quiescent ambient flow $\boldsymbol{u}'^{\infty} = 0$,

$$m_p \frac{d\boldsymbol{V}_p'(t')}{dt'} = -6\pi\mu a_p \boldsymbol{V}_p'(t') - 6\pi\mu a_p^2 \int_0^{t'} \frac{1}{\sqrt{\pi\nu(t'-\tau')}} \frac{d\boldsymbol{V}_p'(\tau')}{d\tau'}\, d\tau' - \frac{m_f}{2} \frac{d\boldsymbol{V}_p'}{dt'} + (m_p - m_f)\boldsymbol{g} \ . \tag{2.10}$$

In fig. 2.2, we prescribed a particle velocity to obtain flow structures. In practice, the dynamics of the particle and fluid are mutually coupled. Therefore, we first need to solve eq. (2.10) to obtain the particle's velocity, which is then used to obtain the unsteady stream

[1] where unsteady stream function was derived for an impulsively-started and an oscillating sphere, respectively.

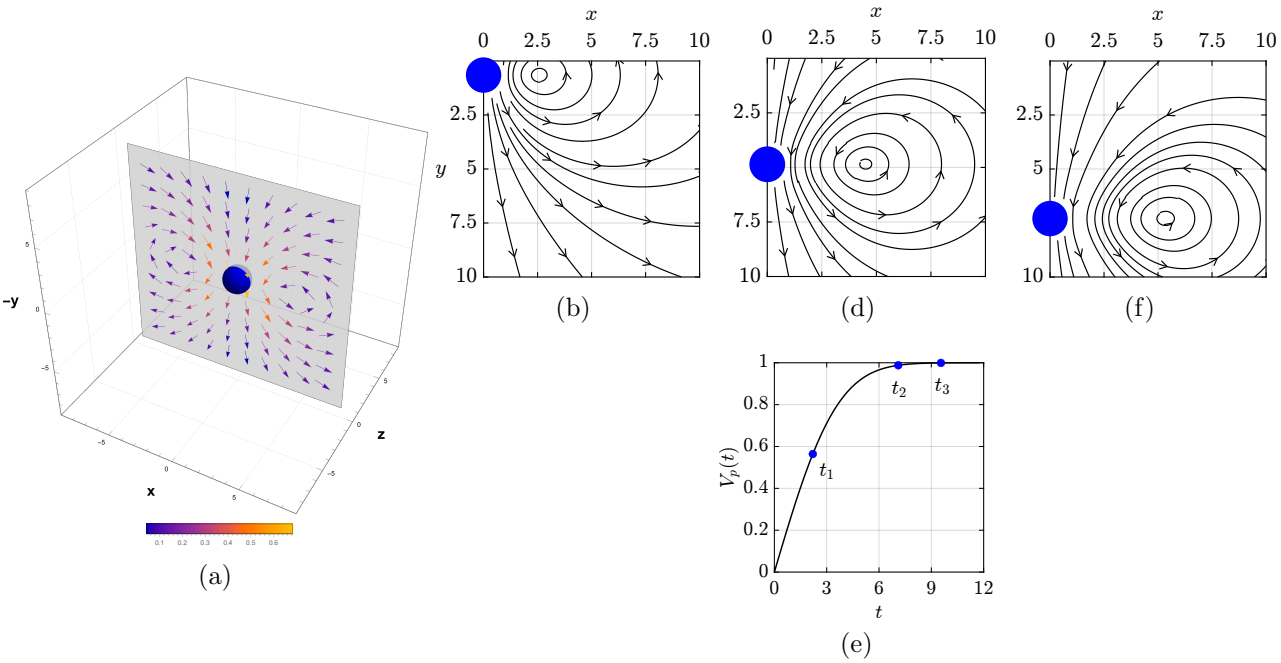

Figure 2.2: Theoretical predictions of the unsteady Stokes model for a sphere accelerating under gravity in a viscous medium: (a) A typical flow field around the settling sphere (blue) in an axial plane, where colors indicate the magnitude of velocity. Panels (b), (d), and (f) show snapshots of the flow streamlines that develop in response to the sphere's falling motion at representative times t_1, t_2, and t_3, which correspond to the times marked in panel (e) for the prescribed particle velocity $V_p(t) = \mathrm{erf}(0.25t)$. A counterclockwise vortex forms at the sphere's accelerating surface and drifts away over time, while the flow maintains fore-aft symmetry. Compare this with the steady Stokes streamlines in fig. 2.1b where no vortex is present.

function according to eq. (2.9). The BBO eq. (2.10) can be solved exactly (see section 2.B) since the gravitational forcing is uniform, leading to a *linear* integro-differential equation[2]. The solution to eq. (2.10) approaches the terminal velocity at an algebraically slow rate, particularly, $|V_p(t) - U_T| \sim 1/\sqrt{t}$, as $t \to \infty$, as shown in section 2.B.

2.2.1 Asymptotics ($t \to \infty$): recovery of steady Stokes flow

We compare the unsteady stream function, ψ, to its steady counterpart given by the nondimensional form of ψ_{Stokes} in eq. (2.1). The idea is to determine if the steady Stokes stream function can be retrieved in a limiting case.

We express the unsteady stream function $\psi(r, \theta, t)$ by adding and subtracting $V_p(t)$

[2]The linearity of this equation overrides the challenges posed by its integro-differential nature, which is primarily computational in the case of the BBO/MRG equation, since it affords an analytical solution.

to/from the integrand:

$$\psi(r,\theta,t) = \sin^2\theta\left[\frac{1}{2r}V_p(t) + \frac{3V_p(t)}{2r}\int_0^t K(t-\tau;r)\,d\tau + \mathcal{R}(r,\theta,t)\right] , \tag{2.11}$$

where $\mathcal{R}$ is the residual term defined as

$$\mathcal{R}(r,\theta,t) = -\frac{3}{2r}\int_0^t (V_p(t) - V_p(\tau))K(t-\tau;r)\,d\tau \ .$$

We assess the asymptotic behaviour of the unsteady stream function as $t \to \infty$. For a settling sphere, $V_p(t) \to 1$ (or U_T dimensionally) as $t \to \infty$. Furthermore, we show (using *Mathematica*) that

$$\lim_{t\to\infty}\int_0^t K(\tau;r)\,d\tau = \frac{1}{2}(r^2-1) + O(1/\sqrt{t}) \ .$$

Assuming $\mathcal{R} \to 0$ as $t \to \infty$, the leading order behavior therefore is

$$\lim_{t\to\infty}\psi(r,\theta,t) \sim \sin^2\theta\Big(-\frac{1}{4r} + \frac{3}{4}r\Big) = \psi_{\text{Stokes}}(r,\theta) \ ,$$

which corresponds to the nondimensional steady Stokes stream function (eq. (2.1)). This suggests that the vortex due to the unsteady stream function drifts away to infinity as $t \to \infty$, at which point the streamlines given by ψ_{Stokes} prevail. However, the description of this route to steady state is valid only when $Re_p = 0$.

An analogous statement can be made in terms of perturbative expansion in small Stokes number S[3], where $S = a_p^2/\nu T_c$ for some characteristic timescale T_c. At finite t, to re-introduce S dependence, we re-scale the nondimensional time by T_c, which effectively replaces $t \to t/S$ in (eq. (1.9)), resulting in the modified PDE: $S\partial\boldsymbol{v}/\partial t = -\boldsymbol{\nabla}p + \boldsymbol{\nabla}^2\boldsymbol{v}$. Assuming the following decomposition for small S,

$$\psi(r,\theta,t) = \psi_{\text{steady}}(r,\theta) + \psi_{\text{correction}}(r,\theta,t) \ ,$$

it can be shown that the leading correction to the steady Stokes stream function is $\mathcal{O}(\sqrt{S})$, which is consistent with the order of magnitude at which its contribution to hydrodynamic force on particle, the BBH force, appears in the BBO eq. (2.10).

[3]Finite S at $t \to \infty$ is dual to the case of $S \to 0$ at finite t

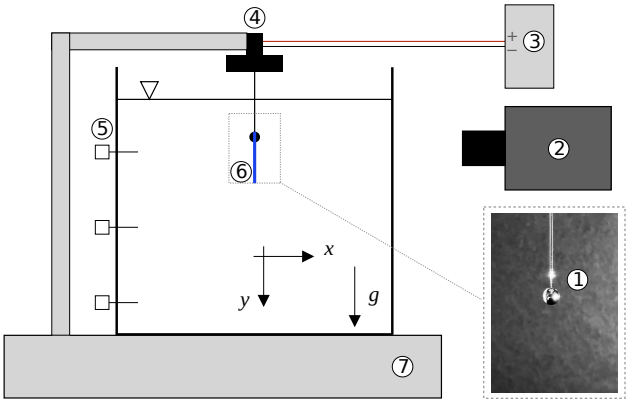

Figure 2.3: Experimental setup: (1) Particle attached to a magnetized needle, (2) High-speed camera, (3) Power supply, (4) Electromagnet, (5) Thermocouples, (6) PIV laser sheet, (7) Optical table. Image courtesy: *Tomek Jaroslawski*.

2.3 Experiments

In the experiments, we define a modified particle Reynolds number, $Re_p = d_p U_T/\nu$, based on terminal velocity and particle's diameter d_p (instead of radius a_p) for practical convenience, without affecting the conclusions of the theoretical analysis in section 2.2. We also compute the Oseen time, $T = \nu/U_T^2$, to track the theoretical validity of the unsteady Stokes model (as discussed in chapter 1). Accordingly, the dimensional time is scaled by the Oseen timescale in all the results shown in this section[4]. We also introduce a nondimensional control parameter $\beta = \rho_p/\rho_f$ which defines the particle-to-fluid density ratio. We now describe the experiments.

A series of controlled experiments under Stokesian conditions were conducted, which involved gravitational settling of rigid spheres from an initial stationary state, $\boldsymbol{V}_p(0) = \boldsymbol{0}$ and $\boldsymbol{v}(\boldsymbol{x}, 0) = \boldsymbol{0}$. The schematic representation of the experimental setup is shown in fig. 2.3. The experiments employed hardened 440C stainless steel (SS) spheres, with a density of $\rho_p = 8075\,\mathrm{kg/m^3}$, submerged in silicone oil with a nominal density of $\rho_f = 997\,\mathrm{kg/m^3}$ and kinematic viscosity 1000 cSt. The viscosity of the silicone oil was measured using a viscometer to account for temperature-dependent variations. At the experimental temperature of 19°C, the measured viscosity was 1140 cSt. We present the results of two representative configurations: of particle diameter $d_p = 3.18$ mm and 4.76 mm, which correspond to particle Reynolds numbers of 0.1 and 0.32, respectively. In both cases, the particle-to-fluid density ratio is $\beta = 8.1$. Additional experiments were also conducted for Reynolds numbers

[4]The nondimensional numbers Re_p and T provide only a ballpark estimate and their exact computed values are not significant by themselves.

of $Re_p = 0.76$ with $\beta = 8.1$, and $Re_p = 0.22$ with $\beta = 1.6$ (see section 2.C), achieved through modifications in particle diameter and material composition. The sphere was suspended in the fluid medium utilizing a magnetized tether, with a sting-to-sphere diameter ratio of 0.1 and $0.15d_p$ (for $d_p = 3.18$ and 4.76 mm, respectively) and positioned at a depth of 20 and $30d_p$ (for $d_p = 4.76$ and 3.18 mm, respectively) below the free surface to reduce any potential influence from surface and sting-induced effects. To avoid boundary effects, the field of view around the sphere, where experimental measurements were made, was enclosed in a cubic container of edge size $\sim 100d_p$[5]. Temperature of the silicone oil was continuously measured to ensure uniform thermal conditions during the experiment. The statistical error and repeatability of the experiment were quantified through reproducing the experiments 20 times. The mean velocity error was found to be 3% in the early stages where $t'/T < 0.1$, and dropped below 1% for the remainder of the sedimentation process. The uncertainty in the sphere diameter was $\pm 0.03d_p$, while the temperature measurement uncertainty was ± 0.5°C, resulting in an uncertainty in the silicone oil viscosity of ± 12 cSt. This uncertainty translates to a variation in the mean velocity derived from the BBO theory of less than 1%. Experimental noise was mitigated by smoothing raw trajectories with a Gaussian kernel of width $0.037T$, acting as a low-pass filter with a 200 Hz cut-off frequency.

The particle's trajectory was measured using a Phantom v2012 high-speed camera, capturing images at a frequency of 2 kHz, followed by a binarization algorithm to determine the trajectory of the sphere's centroid. To measure the particle-induced flow structures, Particle Image Velocimetry (PIV) was employed. The fluid medium was seeded with 10μm glass spheres. Utilizing a non-pulsed 450 nm blue laser, the light beam was directed through a series of optics to produce a thin light sheet with a thickness of less than 1 mm oriented in the $x - y$ plane and aligned along the centerline of the sphere. Flow velocity fields were computed using standard cross-correlation algorithms, with interrogation windows sized at 32×32 pixels in the first image and corresponding search windows of 64×64 pixels in the second image within each image pair. A 50% overlap was implemented to achieve the nominal spatial resolution of 16×16 pixels or 0.2×0.2 d_p.

2.4 Comparison between theory and experiment

The experiments across various parameter configurations confirmed that the sphere approached the terminal velocity given by the expression in eq. (2.2), as expected from previous studies. In addition, notable observations from our experiments include:

[5]Recall from section 1.1.2 that the unsteady Stokeslet, which is a fair description of the flow far from the sphere, decays as $1/r^3$.

1. The sphere's approach to the terminal velocity is algebraic, not exponential as suggested by the quasi-steady Stokes model that assumes Stokes' drag on the sphere.

2. A counterclockwise vortex forms in the fluid at the sphere's accelerating surface, drifting away from the sphere in the direction perpendicular to the fall. Broadly, two distinct behaviors were observed: at very small Re_p, the centers of the vortex and sphere lie on the same horizontal line during the approach to the steady state. On the other hand, at larger Re_p still < 1, the vortex drifts away by initially keeping pace with the sphere and later lagging vertically behind it during the approach to steady state.

In this section, we provide details of the experimental results and compare them against the predictions of the unsteady Stokes model.

2.4.1 Very small $Re_p \ll 1$

We discuss the representative case of $Re_p = 0.1$ which corresponds to $\beta = 8.1$ and $d_p = 3.18$ mm. The Oseen time $T \sim 1$ s and the terminal velocity $U_T \sim 0.034$ m/s.

Figure 2.4a displays the trajectory tracking results, namely the nondimensional vertical displacement y'/d_p of the particle at $Re_p = 0.1$ over nondimensional time t'/T. The figure compares theoretical predictions with and without the BBH force against experimental data. We observe that incorporating the BBH force yields predictions with reduced displacement, aligning closely with experimental observations, particularly during the early stages of sedimentation where the BBH force holds the most importance. Figure 2.4b depicts the non-dimensional vertical velocity $V_p'(t')/U_T$ as a function of t'/T, where the experimental data is derived through temporal differentiation (dy'/dt'). In the experimental $V_p'(t')/U_T$, a clear and distinctive algebraic relaxation rate is evident, which aligns closely with theoretical predictions when the BBH force is considered, in stark contrast to the exponential relaxation observed in its absence. Furthermore, fitting all 20 experimental velocity datasets with a power-law model yields an exponent of -0.495 ± 0.095 for a 95% confidence interval, thus reinforcing quantitative agreement with the unsteady Stokes model's theoretical prediction of $t^{-1/2}$. Agreement between theoretical predictions that include the BBH force and experimental observations was also established for lower β values (see section 2.C). This agreement manifests in both vertical displacement and velocity, as well as in the exponent of the relaxation rate, which remains consistent at $t^{-1/2}$.

We now discuss the flow structures that develop around the sphere. The PIV velocity vectors of the surrounding fluid, accompanied by plotting streamlines, are shown in fig. 2.4b,

spanning early stages ($t'/T < 1$) of the sedimentation process. Initially, a counterclockwise-rotating vortex emerges close to the particle, which represents a cross-sectional view of a 3D vortex ring on the axial plane. As sedimentation progresses, this vortex gradually shifts away from the sphere along the $x-$direction. The x-displacement results from the unsteady diffusive flow dynamics around the particle, attributed to the growth of a laminar boundary layer as the particle sediments. Figure 2.4c shows snapshots of the velocity vectors with streamlines plotted over different times during early sedimentation, based on the theoretical model presented in eq. (2.9). The unsteady Stokes model successfully captures the vortex formation, handedness, and its drift in the x-direction over time, unlike the steady Stokes model, which fails to predict vortex formation.

In this configuration ($d_p = 3.18\,\text{mm}$ and $Re_p = 0.10$), there is a distinct separation between the viscous and inertial timescales: $a_p^2/\nu \sim 10^{-3}$ and $\nu/U_T^2 \sim 1$ seconds, which differ by nearly three orders of magnitude. This allows for a clear delineation between the 'Stokes' regime where unsteady Stokes theory is adequate to describe the flow dynamics and the 'Oseen' regime where convective inertial corrections to the Stokes theory is warranted. Additionally, the particle attains steady state, achieving up to 90% of the terminal velocity within the Stokesian regime, before the onset of convective effects marked by the Oseen time. These factors contribute to the effectiveness of the unsteady Stokes model for the case of small Re_p. However, as discussed in the next subsection, for higher Re_p the theory demonstrates inadequacies in explaining the experimental results.

2.4.2 Larger Re_p, still less than 1

Here, we discuss the representative configuration of $\beta = 8.1$ and $d_p = 4.76$ mm which corresponds to $Re_p = 0.32$, Oseen time $T = 0.19$ s and terminal velocity $U_T = 0.08$ m/s.

At higher Reynolds number, the Oseen timescale T is smaller, resulting in a reduced physical time interval where $t'/T < 1$. Figure 2.5a illustrates the vertical velocity of a settling particle over time, demonstrating agreement between theoretical predictions and experimental data at all times during the settling process. The experimental results show that the BBO equation remains applicable up to $t'/T = 5$, i.e., beyond its formal range of validity of $0 < t'/T < 1$. The theory effectively models the algebraic relaxation rate observed in experiments during later times, as shown in the log-log plot in fig. 2.5a.

The flow velocity vectors, accompanied by plotting streamlines, are shown in fig. 2.5b. Similar to the $Re = 0.10$ case, the vortex core's vertical position closely follows the particle's displacement, with an increasingly apparent $x-$direction displacement over time. However, at later times, around $t'/T \approx 1$, the rate of $x-$direction displacement diminishes, coinciding with the onset of a vertical spatial lag between the vortex core and the sphere's center. An-

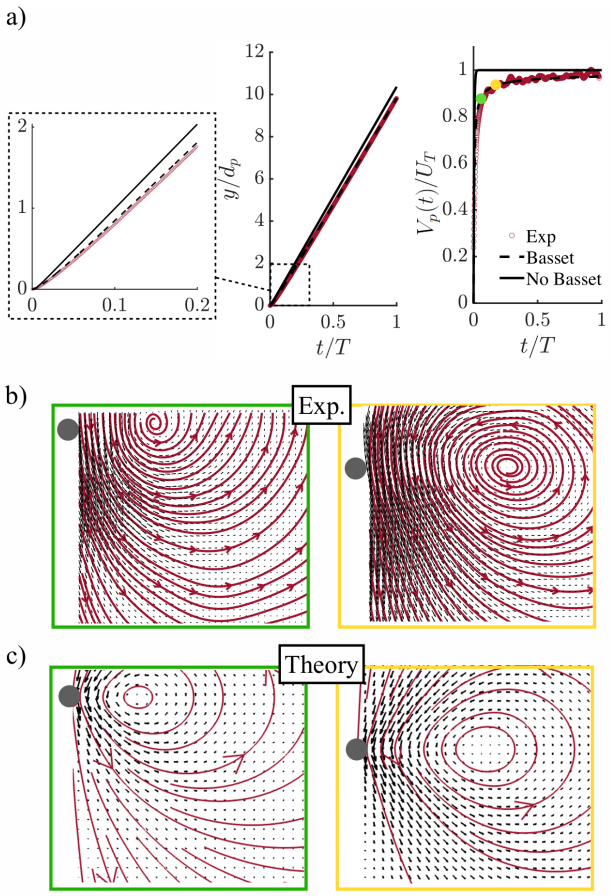

Figure 2.4: Results for $Re_p = 0.10$, with terminal velocity $U_T = 0.034$ m/s and Oseen timescale $T = 0.96$ s. (a) Vertical displacement and velocity of the particle (represented by gray circle, not to scale) over time. Solid and dashed lines are theoretical predictions excluding and including the BBH force, respectively. Experimental data are indicated by markers. (b) Experimental PIV snapshots (cross-section) and (c) theoretical predictions of the unsteady flow (eq. (2.9)) around the particle in the laboratory frame, with overlaid streamlines. Green and yellow points in (a) correspond to the snapshots in (b) and (c), respectively.

other noteworthy observation is the occurrence of asymmetry in the vortex structure around $t'/T \approx 2$, characterized by outward tilting. These late-time behaviors are not explained by the unsteady Stokes model and could be attributed to the increased influence of inertial effects due to convective inertia not accounted in the model. However, the low vortex strength at $t' > T$ makes its effect on the particle's motion weak, as confirmed by the agreement between experiment and theory at later times in particle motion. We hypothesize that, over a long period, the vortex will continue to move away from the sphere with a lag, and the streamlines will approach a steady Oseen flow solution, exhibiting fore-aft asymmetry (see fig. 2.1c).

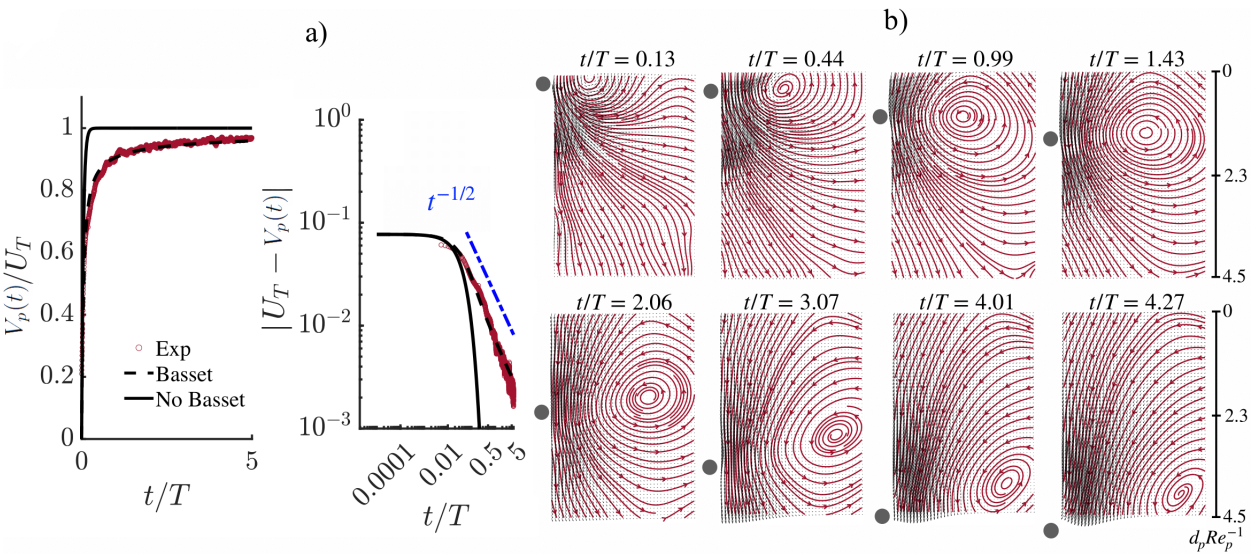

Figure 2.5: Results for $Re_p = 0.32$, with terminal velocity $U_T = 0.08$ m/s and Oseen timescale $T = 0.19$ s. (a) Vertical velocity versus time and a log-log plot of residual vertical velocity against time. The blue dot-dashed line indicates the theoretical relaxation rate of $t^{-1/2}$. Solid lines represent theoretical predictions without the BBH force, while dashed lines include it. Experimental data are shown with markers. (b) PIV snapshots of the unsteady flow field around the particle, with streamlines overlaid for short and intermediate times.

In fig. 2.6a, we show the vertical trajectories of the particle vortex core from both experiment and theory. Additionally, as an estimate for the convective inertial term $\boldsymbol{v} \cdot \nabla \boldsymbol{v}$, we show the vertical location of the maximum absolute value of $\boldsymbol{V}_p(t) \cdot \nabla \boldsymbol{v}$ in the field of view, where $\boldsymbol{V}_p(t)$ represents the particle's instantaneous velocity. For $Re_p = 0.10$, the vortex core exhibits horizontal alignment with the particle, as predicted by our unsteady Stokes model (see fig. 2.2). However, as Re_p increases to 0.32, the vortex core, beyond $t'/T \approx 2$, lags behind the particle, a behavior not predicted by our theory, in which fore-aft flow-symmetry is ensured. For both cases, the vertical location of the maximum in the convective term in the flow field follows the vertical location of the vortex, diverging from the particle's path for $Re_p = 0.32$. The x-displacement of the maximum convection location was found to be negligible, remaining closely aligned with the particle. To investigate the link with increased inertial effects, we tested a particle with $Re_p = 0.76$, which quickly transitioned out of the Stokes flow regime. We observed the same asymmetry in the vortex dynamics (see section 2.C), attributed to inertial effects. In both cases, the vertical location of the maximum convective term correlates with the vertical displacement of the vortex, diverging from the particle's path at $Re_p = 0.32$. This highlights a link between the vortex core's position and the point of maximum convection in the flow field. In fig. 2.6b, we compare the experimental $x-$displacement of the vortex with theoretical predictions. For both $Re_p = 0.10$ and

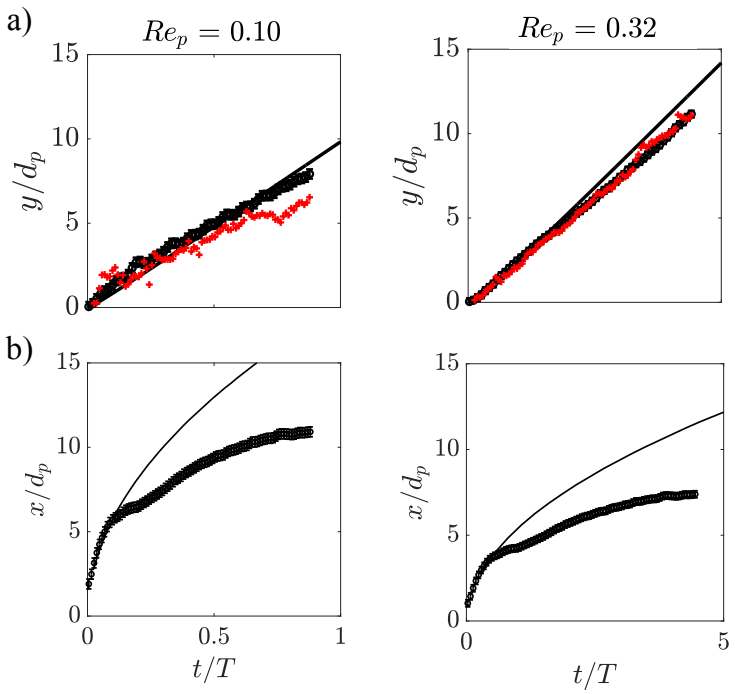

Figure 2.6: Experimental (a) vertical, and (b) horizontal trajectory of the vortex center (marked by black circle , •) compared with the theoretical model predictions (solid black line −). Red crosses × in (a) are the $y-$location of the maximum absolute value of $\boldsymbol{V}_p'(t') \cdot \boldsymbol{\nabla} \boldsymbol{v}'$. Error bars indicate pixel resolution in PIV data.

$Re_p = 0.32$, the theory accurately models experimental observations at early times but soon afterwards, a divergence between experiment and theory occurs. We do not know the reason for this deviation.

2.5 Conclusion

We have shown that the unsteady flow structures generated by a particle settling under gravity in Stokesian conditions are fundamentally different from those predicted by the quasi-steady models. However, a series expansion of eq. (2.9) for small S shows that the quasi-steady streamlines (eq. (2.1)) is recovered at the leading order, with unsteady contributions appearing as $\mathcal{O}(\sqrt{S})$ corrections. Thus, this reaffirms that a quasi-steady Stokes model may be appropriate for *very* small particles or slow processes, corresponding to very small S, where the error due to the neglect of the memory effects is small of $\mathcal{O}(\sqrt{S})$. However, for finite Stokes number, the unsteady Stokes model is warranted to capture the effects of fluid's slow relaxation.

The model reliably describes the transient flow structures at small particle Reynolds number, $Re_p \ll 1$, notably capturing the vortex formation, handedness and its outward

drift. This is attributed to the clear separation of timescales, distinguishing a well-defined 'Stokes' regime from the 'Oseen' regime where convective inertia (i.e., $\boldsymbol{v} \cdot \boldsymbol{\nabla} \boldsymbol{v}$), absent in our model, must be taken into account. However, as $Re_p \sim 1$, the model fails to capture the asymmetry in the flow, underscoring the need to account for convective inertial effects in the model.

The settling dynamics of the particles investigated in this chapter are consistent with theoretical predictions made by the unsteady Stokes model. Critically, our findings show that the BBO equation remains effective in predicting particle motion even beyond its formal limits, specifically past the Oseen timescale.

In particle-laden flows, particle dynamics are typically of primary interest. The BBO/MRG equation, which accurately predicts the particle dynamics, implicitly accounts for the effects of flow structures in the unsteady Stokes regime, which might seem to render the explicit analysis of the flow field unnecessary. However, these flow structures become important as they inform the nature of inter-particle interactions, and thereby guide the development of improved predictive models for particle-laden flows.

Appendix

2.A Derivation of the unsteady stream function

We eliminate pressure and uniform body forces by taking curl of eq. (2.5) to derive the following equation for the vector vorticity field:

$$\frac{\partial \boldsymbol{\omega}}{\partial t} = \boldsymbol{\nabla}^2 \boldsymbol{\omega}, \ \boldsymbol{\nabla} \cdot \boldsymbol{\omega} = 0 \ . \tag{2.12}$$

In axisymmetric, incompressible three-dimensional flows, the only surviving vorticity component is in the azimuthal direction,

$$\omega_\varphi = -\frac{1}{r \sin\theta} d^2 \psi \ ,$$

where the scalar operator d^2, different from the scalar Laplacian operator, is

$$d^2 = \frac{\partial^2}{\partial r^2} + \frac{\sin\theta}{r^2} \frac{\partial}{\partial \theta} \frac{1}{\sin\theta} \frac{\partial}{\partial \theta} \ .$$

The *vector* Laplacian in eq. (2.12) is related to the operator d^2 in the following way:

$$\nabla^2 \boldsymbol{\omega} = \nabla(\nabla \cdot \boldsymbol{\omega}) - \nabla \times \nabla \times \boldsymbol{\omega} = -\frac{1}{r \sin\theta} d^2 (d^2 \psi) e_\varphi \ .$$

Using the above, we derive the equation for the unsteady stream function (eq. (2.6)),

$$\left(\frac{\partial}{\partial t} - d^2 \right) d^2 \psi(r, \theta, t) = 0 \ , \tag{2.13}$$

subject to initial and boundary conditions given in eq. (2.7). The above PDE system is solved using Laplace transform. We assume the following for the solution form (from [1]):

$$\tilde{\psi}(r, \theta, s) = \sin^2\theta \left[\tilde{A}(s) r^2 + \frac{\tilde{B}(s)}{r} + \tilde{C}(s) \sqrt{r} K_{\frac{3}{2}}(r\sqrt{s}) \right] \ , \tag{2.14}$$

where s is the Laplace transform variable and $K_{\frac{3}{2}}(\cdot)$ is the modified Bessel function of the second kind. The scalar functions $\{\tilde{A}(s), \tilde{B}(s), \tilde{C}(s)\}$ are fixed by the boundary conditions:

$$\tilde{A}(s) = -\tilde{V}_p(s)/2,\ \tilde{B}(s) = \frac{1}{2}\tilde{V}_p(s)\left(1 + \frac{3}{s}(1+\sqrt{s})\right),\ \tilde{C}(s) = -\frac{3}{2}\tilde{V}_p(s)\sqrt{\frac{2}{\pi}}\frac{e^{\sqrt{s}}}{s^{1/4}}\ .$$

Here, $\tilde{V}_p(s)$ denotes the Laplace transform of $V_p(t)$. The real-space unsteady stream function is obtained using the above scalar functions in eq. (2.14) and inverting Laplace transform.

2.B Solution of the BBO equation for a settling particle

We reproduce the nondimensional solution for particle's settling velocity from [37]:

$$V_p(t) = \frac{\alpha}{\pi}\int_{-\infty}^{\infty}\int_0^t \frac{ike^{-k^2\tau}}{-k^2+ik\gamma+\alpha}\,d\tau\,dk = \frac{\alpha\gamma}{\pi}\int_{-\infty}^{\infty}\frac{1-e^{-k^2t}}{(-k^2+\alpha)^2+k^2\gamma^2}\,dk\ , \tag{2.15}$$

where $\alpha = R/S,\ \gamma = R\sqrt{3/S}$, with S defined in eq. (3.2) and $R = 3\rho_f/(2\rho_p+\rho_f)$. We recall that $V_p(t)$ is nondimensionalized by the terminal velocity U_T. The integral solution expression is uniformly valid for all non-negative scalars α and γ, and can be solved numerically. We use MATLAB's in-built function *integral* to compute $V_p(t)$. Alternatively, closed-form expressions from [84], involving error functions, can be used for different ranges of α, γ.

Using Laplace's method, we estimate the asymptotic behavior of the expression in eq. (2.15),

$$V_p(t) \sim 1 - \frac{\gamma}{\alpha}\frac{1}{\sqrt{\pi t}} + \ldots\ ,\ \text{as } t\to\infty\ , \tag{2.16}$$

showing that the sphere approaches terminal velocity at an algebraically slow rate of $t^{-1/2}$.

2.C Experiments at other parameters

We provide additional experimental results for a large Re_p configuration corresponding to ($\beta = 8.1,\ d_p = 6$mm, $Re_p = 0.76$), and a small Re_p configuration of ($\beta = 1.6,\ d_p = 9.67$mm, $Re_p = 0.22$). In the latter configuration, to achieve the low density ratio, our experimentalist collaborators used a 9.54 mm diameter wooden sphere, bored a small opening in it to insert a 3.18 mm SS sphere, and sealed it after, effectively increasing the sphere's volume.

1. $\beta = 8.1,\ d_p = 6\mathbf{mm},\ Re_p = 0.76$

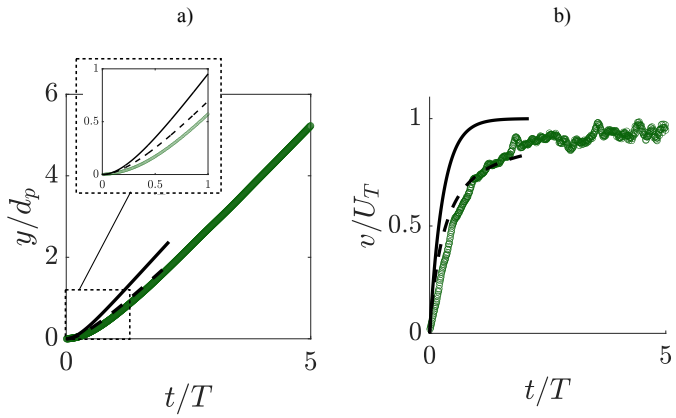

Figure 2.C.1: Comparison of particle's a) vertical displacement and b) vertical velocity as functions of time for $Re_p = 0.76$, where the terminal velocity is $U_T = 0.137$ m/s and the Oseen timescale is $T = 0.06$ s. Green markers: experiment, solid black line: theory without the BBH force, dashed line: theory with the BBH force.

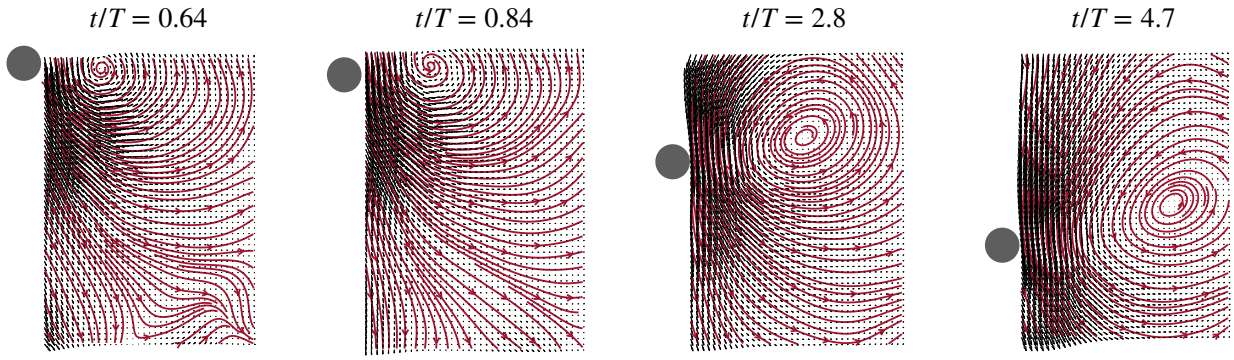

Figure 2.C.2: PIV snapshots of the unsteady streamlines generated by the particle (indicated by gray circle on the left) corresponding to fig. 2.C.1. Gravity acts vertically downwards.

2. $\beta = 1.6,\ d_p = 9.67\ \mathbf{mm},\ Re_p = 0.22$

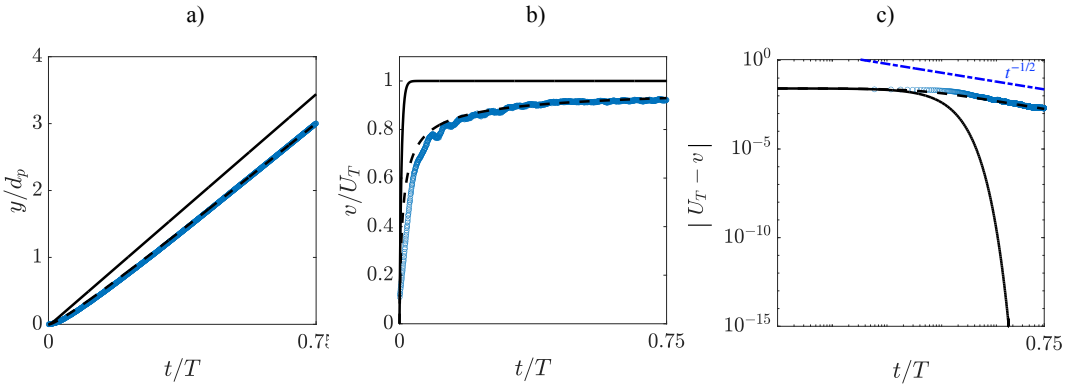

Figure 2.C.3: Comparison of particle's (a) vertical displacement and (b, c) vertical velocity as functions of time for $Re_p = 0.22$, where $U_T = 0.026$ m/s and Oseen timescale is $T = 1.69$ s. Blue markers: experiment, solid black line: theory without the BBH force, dashed line: theory with the BBH force. (c) The log-log plot of the residual vertical velocity versus time confirms the theoretical algebraic relaxation rate of $t^{-1/2}$.

Chapter 3

Explicit integrator for the Maxey-Riley-Gatignol equation

This chapter in large parts is reproduced verbatim from the published articles titled *Explicit Integrators for Nonlocal Equations: the case of the Maxey-Riley-Gatignol Equation* [Jaganathan *et al.*, Quart. Appl. Math. (2024)] and *The Basset-Boussinesq history force: its neglect, validity, and recent numerical developments* [Jaganathan *et al.*, Front. Phys. (2023)]. I acknowledge the co-authors on these articles for their contributions.

3.1 Introduction

Standard Runge-Kutta (RK) and related iterative integrators are powerful techniques to solve ordinary differential equations (ODEs) that describe dynamical systems. However, several physical systems with memory effects evolve nonlocally in time and thus are not directly expressible as dynamical systems. Memory effects appear when the present state of a system depends explicitly on its past states. They pose a challenge for numerical simulations, since standard algorithms are not designed for them. Another challenge, that often goes hand-in-hand with nonlocality, but can also occur by itself in differential equations, is when the solution cannot be expressed in Taylor series, e.g., when it scales with fractional powers of the independent variable. In such cases, the solution and/or terms in the differential equation may not be differentiable, which violates a key hypothesis in the derivation of standard numerical schemes. The Maxey-Riley-Gatignol (MRG) equation is a prototypical example posing these challenges. In this chapter, we provide an accurate and memory-efficient RK algorithm for the MRG equation, and discuss how our ideas and method can be extended to solve a broader class of equations with a memory term.

3.1.1 The Maxey-Riley-Gatignol (MRG) equation

As introduced in chapter 1, the MRG equation describes the motion of an isolated, finitely small spherical particle in the free-space nonuniform ambient flow field $\boldsymbol{u}^\infty : \mathbb{R}^d \times \mathbb{R}^+ \to \mathbb{R}^d$, where d is the dimension of the fluid-occupied space, in the unsteady Stokesian limit. It is also the generalization of the *Basset-Boussinesq-Oseen* (BBO) equation from chapter 2 to non-zero background flow field. The instantaneous state of the particle in this system is given by its position and velocity vectors, $[\boldsymbol{X}_p(t), \boldsymbol{V}_p(t)]^T$. Given its initial state $[\boldsymbol{X}_{p0}, \boldsymbol{V}_{p0}]^T$, the particle evolves according to eq. (1.23), written here in the nondimensional form:

$$\frac{d\boldsymbol{X}_p(t)}{dt} = \boldsymbol{V}_p(t), \tag{3.1a}$$

$$\frac{d\boldsymbol{V}_p(t)}{dt} + \alpha\boldsymbol{w}(t) + \gamma\Big(\frac{\boldsymbol{w}_0}{\sqrt{\pi t}} + \int_0^t \frac{d\boldsymbol{w}(\tau)/d\tau}{\sqrt{\pi(t-\tau)}}\,d\tau\Big) = R\frac{D}{Dt}\boldsymbol{u}^\infty(\boldsymbol{X}_p(t),t) + \boldsymbol{f}_{\mathrm{NH}}(\boldsymbol{X}_p(t),t), \tag{3.1b}$$

where $\boldsymbol{w}(t) := \boldsymbol{V}_p(t) - \boldsymbol{u}^\infty(\boldsymbol{X}_p(t),t)$ is the particle slip velocity, initialized as $\boldsymbol{w}_0 := \boldsymbol{w}(0) = \boldsymbol{V}_{p0} - \boldsymbol{u}^\infty(\boldsymbol{X}_{p0},0)$. The term proportional to γ in eq. (3.1b) is the BBH force, which we will refer to as the *memory term*, and the term proportional to α is the quasi-steady Stokes drag. The variables in eq. (3.1) correspond to physical variables which have been non-dimensionalized by a characteristic length scale L_c, a characteristic timescale T_c, and the velocity scale, $U_c = L_c/T_c$, the choice of each is dependent on the application. The non-negative dimensionless parameters are

$$R = \frac{3\rho_f}{2\rho_p + \rho_f}, \quad St = \frac{S}{3R}, \quad \alpha = \frac{1}{St}, \quad \gamma = \sqrt{\frac{3R}{St}}\,, \tag{3.2}$$

where we recall that ρ_f and ρ_p are the densities of the fluid and particle respectively, a_p is the particle radius, and ν is the fluid kinematic viscosity. The limits $R \to 0$ and $R = 1$ are for infinitely heavy ($\rho_p/\rho_f \to \infty$) and neutrally-buoyant ($\rho_p = \rho_f$) spheres, respectively. We introduce the *particle Stokes number*, St, which is related to S (see eq. (1.7) for definition) by $St = S/(3R)$[1]. While S measures the fluid's relaxation time, the particle Stokes number, St, reflects the particle's relaxation time to the background flow.

Rewriting the governing equation in its nondimensional form allows assessing the relative magnitudes of the different forces acting on the particle. Reduced forms of eq. (3.1b) are often considered in various applications. In the limit $St \to 0$, eq. (3.1b) reduces to $\boldsymbol{w} =$

[1]This is the commonly used definition of the Stokes number. However, we distinguish between S and St to reflect the different parameters that appear in the governing equations for the fluid and the particle, respectively.

$0 \implies \boldsymbol{V}_p(t) = \boldsymbol{u}^\infty(\boldsymbol{X}_p(t), t)$, which corresponds to a *tracer* particle that faithfully follows the background fluid trajectory.

REMARK 3.1. We revisit the definition of an *inertial* particle using the nondimensional MRG equation (eq. (3.1b)). In the limit $St \to 0$, the particle behaves as *inertia-free*, since both the nondimensional particle acceleration term $d\boldsymbol{V}_p/dt$, and the BBH force vanish, leaving an instantaneous force balance equation. When written in dimensional form, the dimensional particle acceleration, $m_p d\boldsymbol{V}_p'/dt'$, is absent from the force balance. For a fixed particle density, this may be equivalently interpreted as the particle having zero mass or zero size. Conversely, an inertial particle may be defined as one with $St > 0$.

For non-zero, finite St (i.e., $0 < St < \infty$), in the limit of $(\rho_p/\rho_f) \to \infty$ corresponding to $R \to 0$, the BBH force and the inertial force from the ambient flow in eq. (3.1b) become subdominant, leading to a simplified model for a *heavy* particle:

$$\frac{d\boldsymbol{V}_p(t)}{dt} + \alpha \boldsymbol{w}(t) = \boldsymbol{f}_{\mathrm{NH}}(\boldsymbol{X}_p(t), t) \ . \tag{3.3}$$

However, caution is needed here. Since the particle Stokes number St implicitly depends on R (see eq. (3.2)), the limit $R \to 0$ for non-zero finite St forces $S \to 0$ as well. Thus, this limit corresponds to an infinitesimally small particle, providing a model for a *heavy point* particle.

On the other hand, for finite ρ_p/ρ_f, the nominal relative strength of the BBH force compared to the quasi-steady Stokes drag is determined solely by S (check the ratio γ/α)[2]. Consequently, for non-zero R and small S, which could correspond to slow processes, the quasi-steady Stokes model for the particle, commonly known as the *reduced MRG equation*, is given by

$$\frac{d\boldsymbol{V}_p(t)}{dt} + \alpha \boldsymbol{w}(t) = R\frac{D\boldsymbol{u}^\infty}{Dt}(\boldsymbol{X}_p(t), t) + \boldsymbol{f}_{\mathrm{NH}}(\boldsymbol{X}_p(t), t) \ , \tag{3.4}$$

where the error due to ignoring the BBH force is $\mathcal{O}(\sqrt{S})$. This weak scaling suggests that the model is a good approximation for very small S whereas, $S \sim 1$ warrants retention of the memory term in the MRG equation.

These various simplifications of the MRG equation (eqs. (3.3) and (3.4)) capture the particle's leading-order dynamics for specific parameter limits and simplify both analytical and numerical handling due to omission of the BBH force. However, in many practical cases, these limits don't apply, and the full MRG equation with the BBH force needs to be considered.

[2]This is only a nominal estimate based on the assumption that the BBH force is an $\mathcal{O}(1)$ term, which is however not guaranteed during the dynamics.

The MRG equation belongs to the general class of fractional differential equations (FDEs). Indeed, the memory term is a fractional half-derivative in t, defined in the Riemann-Liouville sense by

$$\frac{d^{1/2}\boldsymbol{w}(t)}{dt^{1/2}} := \frac{\boldsymbol{w}_0}{\sqrt{\pi t}} + \int_0^t \frac{d\boldsymbol{w}(\tau)/d\tau}{\sqrt{\pi(t-\tau)}}\, d\tau \,. \tag{3.5}$$

The convolution operation in the above expression introduces nonlocality in time. The slowly-decaying memory kernel, $K_B(\tau) = 1/\sqrt{\pi\tau}$, is known as the *Basset* kernel. The weak, integrable singularity of the memory kernel at current-time acts such that the current state has the most 'vivid' effect, while the memory of earlier states slowly 'fades away' with time. In addition, there is an initial time singularity at $t = 0$ due to $1/\sqrt{t}$ for non-zero $\boldsymbol{w}_0$. The BBH force may also be expressed as a total derivative owing to the following identity,

$$\frac{d^{1/2}\boldsymbol{w}(t)}{dt^{1/2}} = \frac{d}{dt}\int_0^t \frac{\boldsymbol{w}(\tau)}{\sqrt{\pi(t-\tau)}}\, d\tau \,, \tag{3.6}$$

which is often used in constructing numerical methods for the MRG equation (discussed in section 3.1.3).

For the rest of the chapter, we rewrite the MRG system in a compact form for the new state variables $[\boldsymbol{X}_p(t), \boldsymbol{w}(t)]^T$ as:

$$\frac{d\boldsymbol{X}_p(t)}{dt} = \boldsymbol{w}(t) + \boldsymbol{u}^\infty(\boldsymbol{X}_p(t), t) \,, \tag{3.7a}$$

$$\frac{d\boldsymbol{w}(t)}{dt} = -\alpha\boldsymbol{w}(t) - \gamma\frac{d^{1/2}\boldsymbol{w}(t)}{dt^{1/2}} + \boldsymbol{N}(\boldsymbol{w}(t), t), \tag{3.7b}$$

where the memory term appears as a half-derivative in time, initial state is $[\boldsymbol{X}_{p0}, \boldsymbol{w}_0]^T$, and the nonlinear and external forces are bundled into the vector-valued function $\boldsymbol{N}$ where

$$\boldsymbol{N}(\boldsymbol{w}(t), t) = \Big(R - 1\Big)\frac{D}{Dt}\boldsymbol{u}^\infty(\boldsymbol{X}_p(t), t) - \boldsymbol{w}\cdot\boldsymbol{\nabla}\boldsymbol{u}^\infty(\boldsymbol{X}_p(t), t) + \boldsymbol{f}_{\mathrm{NH}}(\boldsymbol{X}_p(t), t) \,.$$

Note that $\boldsymbol{u}^\infty(\boldsymbol{x}, t)$ and functions of it are evaluated at the particle position, $\boldsymbol{X}_p(t)$, which makes the system nonlinear. We assume necessary smoothness of the underlying flow field $\boldsymbol{u}^\infty(\boldsymbol{x}, t)$. We remind the reader that while we address the numerical treatment of eq. (3.7b), the equation for the particle position eq. (3.7a) is co-evolved. Owing to its local nature, the particle position can be integrated, once the velocity is known, using any standard integrator. Hence, we do not discuss it any further.

3.1.2 Numerical considerations for the MRG equation

Closed-form solutions to the equation exist only for some specific cases, such as the unidirectional settling under the action of gravity (addressed in chapter 2), free-relaxation of a particle in quiescent fluid, and a particle in Couette flow and oscillatory background flow [37]. More generally, such as in turbulent flows, due to the nonlinear dependence of the force on the particle's instantaneous position, a numerical approach is warranted to obtain solution to the MRG equation. However, when solving numerically on a discrete time-grid $\{t_n = n\Delta t\}$, the MRG equation poses several challenges:

1. Since at every time instant we need to perform an integral from the initial time to the present, the operational costs grow quadratically with simulation time instead of the more typical linear growth seen in ODEs.

2. Since we have to store all past states at every time instant, the memory storage requirement grows linearly with time instead of staying constant. This is also reflected in a related cost to restart the simulation from an arbitrary state: the state of the particle at a given time can no longer be prescribed as the new initial condition to restart the simulation, instead the entire trajectory up to the current time needs to be provided. As a result, long-time and multi-particle simulations become prohibitively expensive.

3. The memory term in eq. (3.5) warrants care when handling the singular kernel numerically.

4. The solution to the MRG equation is not differentiable at $t = 0$, i.e., it lacks a well-defined Taylor series expansion around $t = 0$.

The BBH force is often neglected from particle dynamics due to above challenges, especially in multi-particle and long-time simulations. Further, due to the BBH force, the MRG equation does not represent a dynamical system [36]. Indeed, the state of the particle at any given instant, is insufficient to uniquely determine its subsequent evolution in position-velocity space. Instead, the entire trajectory of the particle up to the current state is required to evolve to a new state. Consequently, standard numerical integrators, such as Runge-Kutta methods, cannot be used to solve the MRG equation without incurring significantly higher computational and memory storage costs compared to their intended usage to solve ODEs.

3.1.3 Review of existing numerical approaches

The computational barriers have been progressively bridged in earlier works with numerical strategies that operate broadly on ideas of truncating or approximating the BBH force.

Exceptionally, Prasath et al. (2019) [37] provided a local PDE reformulation where the MRG equation is prescribed as a boundary forcing to a one-dimensional diffusion problem. Their reformulation resulted in an implicit time integrator with spectral accuracy. We classify these numerical solution approaches by identifying the overarching strategy they use to address the computational challenges, and briefly review them below.

1. **Full quadrature:** Daitche [86] developed a general scheme to compute the memory term to arbitrarily high degrees of accuracy. Using the identity in eq. (3.6), the integrated form of the MRG equation for the particle's evolution between t_n and t_{n+1} may be written as

$$\begin{aligned}\boldsymbol{w}(t_{n+1}) = \boldsymbol{w}(t_n) - \gamma\left(\int_0^{t_{n+1}} \frac{\boldsymbol{w}(\tau)}{\sqrt{\pi(t_{n+1}-\tau)}}\,d\tau - \int_0^{t_n} \frac{\boldsymbol{w}(\tau)}{\sqrt{\pi(t_n-\tau)}}\,d\tau\right) \\ + \int_{t_n}^{t_{n+1}} \Big(-\alpha\boldsymbol{w}(\tau) + \boldsymbol{N}(\boldsymbol{w}(\tau),\tau)\Big)\,d\tau\ .\end{aligned} \tag{3.8}$$

   Typically, quadrature routines use polynomial interpolation of the integrand to derive numerical approximations for the integral. However, while using this standard approach in the case of the BBH force, care is warranted at the integral's limits due to the current-time singularity of the *Basset* kernel. Hence, [86] employed a Lagrange-polynomial interpolant only for the slip-velocity part of the integrand, retaining the memory kernel (and singularity) as is. The resulting integrals are then evaluated exactly. Here, the degree of the interpolating polynomial determines the order of accuracy. The quadrature for the integrals involving the memory kernel in eq. (3.8) is given by

$$\int_0^{t_n} \frac{\boldsymbol{w}(\tau)}{\sqrt{\pi(t_n-\tau)}}\,d\tau = \sum_{m=1}^{n}\int_{t_{m-1}}^{t_m} \frac{\boldsymbol{w}(\tau)}{\sqrt{\pi(t_n-\tau)}}\,d\tau \approx \sqrt{\Delta t}\sum_{m=1}^{n}\mu_m^n \boldsymbol{w}(t_{n-m})\ , \tag{3.9}$$

   where $\{\mu_m^n\}$ are scheme-specific, *time-dependent* weights which can be pre-computed and are explicitly provided by [86] for $\mathcal{O}(\Delta t), \mathcal{O}(\Delta t^2), \mathcal{O}(\Delta t^3)$-accurate schemes. We note the persisting need to retain the past values of the slip-velocities to compute the quadrature. Hence, the growing memory and operational cost is unavoidable in this approach. However, higher-accuracy schemes come at essentially no additional cost.

   Another class of full quadrature schemes, of varying accuracy, designed specifically for fractional-differential equations are described in the works of [87, 88]. These methods are similar to exponential-integrators introduced by [3] but adapted to fractional derivatives. While they reduce operational costs, which grow slower than quadratically but faster than linearly, memory storage costs still increase with simulation time. Additionally, many existing methods, including these, do not address the lack of a well-defined Taylor

series expansion near $t = 0$, which becomes a source of reduced error convergence rates.

2. **Window-based approaches:** This class of methods involves splitting the integral in the BBH force into one over the *distant past*, and another for the *recent past*. The motivation is to accurately treat the current-time singularity, and approximate the memory kernel in the distant past to reduce operational costs. A general construction is given by

$$\int_0^{t_n} \frac{1}{\sqrt{\pi(t_n-\tau)}} \frac{d\boldsymbol{w}(\tau)}{d\tau}\, d\tau \approx \boldsymbol{F}_{tail}(t_n) + \boldsymbol{F}_{win}(t_n) \tag{3.10}$$

where the integral is approximated following a decomposition into tail and recent window:

$$\boldsymbol{F}_{tail}(t_n) = \int_0^{t_n - t_{win}} K_{tail}(t_n-\tau)\frac{d\boldsymbol{w}(\tau)}{d\tau}\, d\tau \ , \ \boldsymbol{F}_{win}(t_n) = \int_{t_n - t_{win}}^{t_n} K_{win}(t_n-\tau)\frac{d\boldsymbol{w}(\tau)}{d\tau}\, d\tau \ . \tag{3.11}$$

Here, $t_{win} = M_w \Delta t$, $M_w \in \mathbb{N}$ is the recent-past window-size and a free-parameter of the method. The different approaches are essentially distinguished by their choice of these approximate kernels K_{win}, K_{tail}.

As the current-time singularity always occurs in the window $[t_n - t_{win}, t_n]$, the form of the kernel (hence singularity) is usually retained in this window. Thus, one sets $K_{win}(\cdot) = K_B(\cdot)$ and thereafter employs a quadrature scheme similar to [86]. For instance, [89] assumed constant slip-acceleration whereas [90] used a linear interpolant of the slip-acceleration. In another instance, instead of constructing a quadrature, [91] approximated the integral in the recent time-window by the series representation of the Riemann-Liouville half-derivative.

In the tail window $[0, t_n - t_{win}]$, one seeks fast-converging approximate kernels for the Basset kernel, K_B. Dorgan & Loth [92] and Bombardelli [91] ignored the tail, effectively truncating the integral by setting $K_{tail}(\cdot) = 0$. On the other hand, a new class of *exponential methods* emerged, e.g., [90] where $K_{tail}(\cdot)$ is given by a sum of decaying exponentials that approximate K_B in $[0, t_n - t_{win}]$. The resulting tail integral for method-specific positive constants $\{a_i, t_i\}$ and known functional forms of $\{\check{\alpha}, \check{\beta}\}$ is given by

$$\begin{aligned} \boldsymbol{F}_{tail}(t_n) = \sum_{i=1}^{m} \boldsymbol{F}_i(t_n) &= \sum_{i=1}^{m} \int_0^{t_n - t_{win}} a_i K_i(t_n-\tau)\frac{d\boldsymbol{w}(\tau)}{d\tau}\, d\tau, \\ &= \sum_{i=1}^{m} \int_0^{t_n - t_{win}} a_i \check{\alpha}(t_i) e^{-\check{\beta}(t_i)(t_n-\tau)}\frac{d\boldsymbol{w}(\tau)}{d\tau}\, d\tau \ . \end{aligned} \tag{3.12}$$

In particular, $\boldsymbol{F}_i$ follows a dynamical evolution given by,

$$\boldsymbol{F}_i(t_n) = e^{-\check{\beta}(t_i)\Delta t}\boldsymbol{F}_i(t_n - \Delta t) + a_i\check{\alpha}(t_i)\int_{t_n - t_{win} - \Delta t}^{t_n - t_{win}} e^{-\check{\beta}(t_i)(t_n - \tau)}\frac{d\boldsymbol{w}(\tau)}{d\tau}\, d\tau \ . \tag{3.13}$$

Note the recursive nature of this method, which is a consequence of the exponential-form approximation. This suggests that $\boldsymbol{F}_i(t)$ are dynamical variables that satisfy linear equations forced by the slip-acceleration. Parmar et al. [93] essentially pursue this idea to obtain a differential equation for each approximate force $\boldsymbol{F}_i(t)$. The quadrature is greatly curtailed by requiring small t_{win} and the exponential approximation is obtained following [94] but otherwise their method is similar to that described above.

For window-based approaches, the parameters m and t_{win} must be chosen carefully, and often the criterion is problem-specific. For the physical system of interest in [91], t_{win} is determined based on the time beyond which the particle-state correlations were found to be weak. A minimization problem for an error-like quantity to determine an optimal t_{win} may also be setup [90, 93, 95].

3. **Formulation as a partial differential equation**: A different approach was introduced by [37] who showed that the governing MRG equation, in its entirety, can be posed as a dynamic boundary-condition for a suitable 1D diffusion equation over a half-line - a system for which much is known and solvable. Prasath et al. [37] essentially exploit the fact that the Dirichlet-to-Neumann operator for the diffusion equation on half-line is (up to a sign) the Riemann-Liouville half-derivative. Whereas the window-based methods hinted at or constructed dynamical systems that approximate the MRG equation, [37] describe an exact reformulation of the MRG equation that is *local-in-time*. They introduced a diffusing quantity $\boldsymbol{q}(\zeta, t)$ in a pseudo-space coordinate $\zeta > 0$. The slip-velocity $\boldsymbol{w}(t)$ is related to $\boldsymbol{q}$ by $\boldsymbol{q}(0, t) := \boldsymbol{w}(t)$. Under these definitions, they proposed the following PDE system,

$$\boldsymbol{q}_t = \boldsymbol{q}_{\zeta\zeta}, \tag{3.14a}$$

$$\boldsymbol{q}(\zeta > 0, t = 0) = \boldsymbol{0}, \tag{3.14b}$$

$$\boldsymbol{q}_t(0, t) + \alpha\boldsymbol{q}(0, t) - \gamma\boldsymbol{q}_\zeta(0, t) = \boldsymbol{N}(\boldsymbol{q}(0, t), t), \tag{3.14c}$$

$$\lim_{t\to 0}\boldsymbol{q}(0, t) = \boldsymbol{w}_0 \ , \tag{3.14d}$$

where $\boldsymbol{q}_\zeta(0, t)$ represents the BBH force, and the subscripts t and ζ refer to partial derivatives. The MRG equation manifests as a generalized Robin boundary-condition in eq. (3.14c).

Using the above reformulation, one derives an expression for $\boldsymbol{q}(0,t)$ (equivalently the slip-velocity) for $t_n < t \leq t_{n+1}$ given $\boldsymbol{q}(0,t_n)$ with the introduction of a new dynamical quantity called the 'history function', denoted by $\check{\boldsymbol{H}}(k,t)$,

$$-\frac{\pi}{2}\boldsymbol{q}(0,t) = \int_0^\infty e^{-k^2(t-t_n)}\mathrm{Im}\Big(k\check{\boldsymbol{H}}(k,t_n)\Big)\,dk + \int_0^{t-t_n} \boldsymbol{N}(\boldsymbol{q}(0,t_n+\tau))\left[\int_0^\infty \mathrm{Im}\Big(\frac{ke^{-k^2(t-t_n-\tau)}}{ik\gamma - k^2 + \alpha}\Big)\,dk\right]d\tau, \tag{3.15a}$$

$$\check{\boldsymbol{H}}(k,t_{n+1}) = e^{-k^2\Delta t}\check{\boldsymbol{H}}(k,t_n) - \int_0^{\Delta t} e^{-k^2(\Delta t-\tau)}\left\{\boldsymbol{q}(0,t_n+\tau) + \frac{\boldsymbol{N}(\boldsymbol{q}(0,t_n+\tau))}{ik\gamma - k^2 + \alpha}\right\}d\tau\ . \tag{3.15b}$$

At $t = 0$, the history function is known analytically and for $t_n > 0$, $\check{\boldsymbol{H}}(k,t_n)$ is represented using Chebyshev polynomials. One assumes the slip-velocity $\boldsymbol{q}(0,t)$, $t \in [t_n, t_{n+1}]$ also has a Chebyshev expansion. Given $\check{\boldsymbol{H}}(k,t_n)$, [37] solve eq. (3.15a) using Newton's method for the Chebyshev coefficients of $\boldsymbol{q}(0,t)$. Then they update the history function using eq. (3.15b) to solve for the slip-velocity in the next time-step. The highlight of the scheme is that no approximation is made to the kernel. Moreover, by including $\check{\boldsymbol{H}}(k,t)$ as a dynamical variable, the operational cost, the memory requirement, and the cost to restart the simulation become independent of time.

3.1.4 An overview of the proposed method

Our approach to solve the MRG equation merges a modified version of Cox & Matthews' exponential time-differencing (ETD) method [3] for time-stepping with the introduction of time-evolving auxiliary variables to address nonlocality, leading to a Markovian embedding [96–99] of the original equation into a larger state-space. The current work builds on the ideas in [37] to develop *explicit* integration schemes, of various orders of accuracy, for the MRG equation.

Remark 3.2. In [37], the authors established a relationship between the MRG equation and the diffusion equation. Indeed the spectral representation we use in this chapter is a consequence of that relationship. However, as we will see, the essential requirement to eliminate memory effects, and thereby derive numerical integrators, is simply the existence of a spectral representation.

In order to illustrate our idea, we begin with a nonlinear integral equation, instead of the original differential representation for the underlying dynamics (Section 3.2 provides

details on transforming the MRG equation into an integral equation). Further, to simplify the exposition, we consider the scalar case. Thus, suppose $w : [0, \infty) \to \mathbb{R}$ is a sufficiently smooth solution to the integral equation

$$w(t) = \chi(t)w_0 + \int_0^t \chi(t-\tau)N(w(\tau), \tau)d\tau \tag{3.16}$$

where N is a nonlinear function of w and $\chi(t)$ is the solution to the associated linear equation. For equations with memory effects, it is often the case that the linear solution lacks the semigroup property, i.e., $\chi(t+\tau) \neq \chi(t)\chi(\tau)$. Consequently, $w(t)$ necessarily depends on $w(\tau)$ *for all* $\tau \leq t$, *i.e.*, the solution depends on the full trajectory and not just the present state. To introduce the auxiliary variables that address the nonlocality (and eventually the rising memory costs), we employ a particularly convenient 'spectral representation' of the solution to the linear problem. A function $\chi(t)$ is said to have a *spectral representation* if it has the form

$$\chi(t) = \int_\Gamma e^{f(k)t}g(k)dk \tag{3.17}$$

where Γ is some contour over the $k - \mathbb{C}$ plane for some functions f, g of the complex variable k. Typically, f, g are analytic functions. Up to a switch in the order of integration, we find the integral equation for $w(t)$ can be written as

$$w(t) = w_0 \int_\Gamma e^{f(k)t}g(k)dk + \int_\Gamma \int_0^t e^{f(k)(t-\tau)}g(k)N(w(\tau), \tau)d\tau\, dk \ .$$

If we define

$$H(k,t) = w_0 e^{f(k)t}g(k) + \int_0^t e^{f(k)(t-\tau)}g(k)N(w(\tau), \tau)d\tau \ ,$$

then we infer

$$\frac{dH}{dt} = f(k)H + g(k)N(w(t), t), \quad \text{where } w(t) = \int_\Gamma H(k,t)dk \ , \tag{3.18}$$

with initial state $H(k, 0) = w_0 g(k)$, which is an exact local-in-time reformulation of the integral equation for $w(t)$ in terms of a new infinite-dimensional state-variable $H(\cdot, t)$ (considered as a function of $k \in \Gamma \subset \mathbb{C}$). Note that the equation for $H(\cdot, t)$ is a dynamical system which naturally arises from the spectral representation of the kernel of the integral equation $\chi(t)$.

The two equations, eq. (3.16) and eq. (3.18), are equivalent, and are exact representations of the dynamics of $w(t)$. One may consider a discretization of either representation to develop a numerical method. A direct discretization of eq. (3.16) is considered in [87] and leads to generalized ETD methods for FDEs. In [100], RK integrators for generic multi-term FDEs

are provided. These methods, however, do not address the growing memory cost associated with the nonlocal terms present in FDEs. Alternatively, one may work with the local version, eq. (3.18), which warrants an additional spectral discretization to compute the integral over Γ. In section 3.6, we provide evidence suggesting that a direct discretization of eq. (3.18) in the context of the MRG equation leads to an overall inferior numerical method.

Our proposed approach for the MRG equation involves a simultaneous discretization of both eq. (3.16) and eq. (3.18) that retains the best features of either representation. Our work may also be considered a window-based method but our 'window' is motivated by the exact spectral representation as opposed to an ad hoc design parameter. We closely follow the procedure of Hochbruck & Ostermann [101] to construct an RK algorithm for time-stepping the resultant local system. Unlike the standard RK derivations which assume a Taylor series expansion for the unknown solution, we are forced to employ expansions in non-negative powers of $t^{1/2}$ for the solution. This is a consequence of the smoothness properties of the solution to the MRG equation. However, it also captures a feature of the physics, namely the role of the initial slip velocity w_0.

In section 3.2, we develop the ideas for our numerical procedure. The specifics of the RK numerical schemes for the MRG equation are provided in section 3.3. In section 3.4, we present an error analysis for the RK schemes. In section 3.5, we present numerical experiments to verify the expected convergence rates.

3.2 Semigroup property and Markovian embedding

The central idea of Markovian embedding is to allow ideas from standard numerical time-stepping methods (based on local evolution rules) to work efficiently for nonlocal equations as well. Here we want to construct our Markovian embedding for the MRG equation such that the standard ETD method can be favorably adapted. In this section, we begin with a discussion on the iterative ETD method and identify a key property, namely the semigroup property, that makes it work for ODEs. Following this, we address the lack of the semigroup property in the MRG equation and construct a Markovian embedding as a fix.

3.2.1 Semigroup property and the ETD method

In the context of this study, a real-valued function $S : \mathbb{R}^+ \to \mathbb{R}$ is said to have the semigroup property if $S(t+\tau) = S(t)S(\tau)$, $\forall t, \tau \in \mathbb{R}^+$ where the right-hand side is a product of real numbers. Additionally, one sets $S(0) = 1$ (the multiplicative identity) and requires some smoothness of the function S. We refer the reader to [102] for more rigorous definitions of the semigroup property for solutions to differential equations.

We now discuss the construction of the ETD method [3] where the semigroup property plays an important role. We consider eq. (3.7b) when $\gamma = 0$:

$$\frac{dw}{dt} = -\alpha w + N(w,t),\ w(0) = w_0. \tag{3.19}$$

The solution to the linear part of the equation is $w_0 \exp(-\alpha t)$. Hence, we can identify the function $S(t) = \exp(-\alpha t)$ which evidently has the semigroup property. The solution to eq. (3.19) can be written in the following Duhamel form,

$$w(t) = e^{-\alpha t} w_0 + \int_0^t e^{-\alpha(t-\tau)} N(w(\tau),\tau)\, d\tau\ , \tag{3.20a}$$

$$\implies w(t+\Delta t) = e^{-\alpha \Delta t} w(t) + \int_0^{\Delta t} e^{-\alpha(\Delta t-\tau)} N(w(t+\tau), t+\tau)\, d\tau\ . \tag{3.20b}$$

We highlight here that the semigroup property of the exponential function allowed the derivation of the local iterative rule eq. (3.20b) from eq. (3.20a). Assuming sufficient smoothness for the functions w and N, different approximations for the integral term in eq. (3.20b), which is now localized around t, lead to different numerical schemes. If we denote the numerical approximation to the solution at time t_n by w_n, a canonical explicit, multi-step scheme (such as the ETD-Adam Bashforth method) for a fixed choice of integer $m \leq n$ is given by

$$w_{n+1} = e^{-\alpha \Delta t} w_n + \Delta t \sum_{j=1}^{m} W_j N(w_{n+1-j}, t_{n+1-j}).$$

Here the choice of nodes and corresponding weights $(\{t_{n+1-j}\}, \{W_j\})$ defines a scheme with a certain p-order local accuracy $|w_n - w(t_n)| \sim \mathcal{O}(\Delta t)^{p+1}$.

On the other hand, a canonical explicit, multi-stage (single-step) scheme of $\check{s}$-stages such as the ETD-Runge Kutta method (ETD-RK) is given by

$$w_{nj} = e^{-\alpha c_j \Delta t} w_n + \Delta t \sum_{l=1}^{j-1} \tilde{W}_{jl} N(w_{nl}, \tau_{nl}),$$

$$w_{n+1} = e^{-\alpha \Delta t} w_n + \Delta t \sum_{j=1}^{\check{s}} W_j N(w_{nj}, \tau_{nj})\ ,$$

where $\{w_{nj}\}$ are numerical solutions progressively constructed at intermediate times between two consecutive time-steps $\{\tau_{nj} = t_n + c_j \Delta t\}$ for $0 \leq c_j \leq 1$. The solution at t_{n+1} is constructed from these intermediate evaluations in the $\Delta t-$neighborhood of t_n for different choices of weights $\{W_j, \tilde{W}_{jl}\}$ (see [3] for exact expressions). A multi-stage scheme such as

RK-ETD is a numerical Markovian[3] method since the information in the Δt-neighborhood required to compute w_{n+1} is constructed from only one prior information at t_n.

3.2.2 Lack of semigroup property and the MRG equation

Consider now an integral equation such as eq. (3.20a) but where the linear solution *does not* have the semigroup property. In other words, in the place of the exponential function, we have a function $\mathcal{T}(t)$ such that $\mathcal{T}(t+\tau) \neq \mathcal{T}(t)\mathcal{T}(\tau)$. Then, for every time t_{n+1}, we have instead

$$\begin{aligned} w(t_{n+1}) &= \mathcal{T}(t_{n+1})w_0 + \int_0^{t_{n+1}} \mathcal{T}(t_{n+1}-\tau)N(w(\tau),\tau)\,d\tau, \\ &= \mathcal{R}_{\text{history}}(t_n; t_{n+1}) + \int_0^{\Delta t} \mathcal{T}(\Delta t-\tau)N(w(t_n+\tau), t_n+\tau)\,d\tau\ , \\ \text{where, } \mathcal{R}_{\text{history}}(t_n; t_{n+1}) &:= \left(\mathcal{T}(t_{n+1})w_0 + \int_0^{t_n} \mathcal{T}(t_{n+1}-\tau)N(w(\tau),\tau)\,d\tau\right)\ . \end{aligned} \tag{3.22}$$

Subject to smoothness requirements as before, the integral over $[0, \Delta t]$ can be replaced by numerical approximations as in the RK-ETD schemes. However, unlike in eq. (3.20b), the lack of semigroup property leaves a residual expression denoted by $\mathcal{R}_{\text{history}}(t_n; t_{n+1})$ which is nonlocal and represents the influence of the solution *up to* time t_n on the solution at time t_{n+1}.

When $\mathcal{T}$ has the semigroup property, $\mathcal{R}_{\text{history}}(t_n; t_{n+1}) = \mathcal{T}(\Delta t)w_n$. But without this property, $\mathcal{R}_{\text{history}}$ involves an integral over the entire history of the solution. To evolve the solution by just one additional time-step, we need to integrate the full trajectory up to the current time, implying we have no notion of locality. Linear FDEs possess such solutions that lack the semigroup property. This is indeed also the case with the solution to the linear MRG equation.

We recall the MRG equation written in compact form eq. (3.7). It suffices to consider the MRG equation in its scalar form without loss of generality for the discussions to follow. We begin by identifying the solution to the linear MRG equation (set $N = 0$). We denote by $\chi(t; \alpha, \gamma)$ the function satisfying the linear MRG equation with parameters α, γ and the initial condition set to 1. Hence,

$$\frac{d\chi}{dt} + \gamma \frac{d^{1/2}\chi}{dt^{1/2}} + \alpha\chi = 0, \quad \chi(0; \alpha, \gamma) = 1.$$

[3]We use the term 'Markovian' only to indicate the *memoryless* property: a future state depends only on the current state, however defined. No further connection is made to Markov process in the stochastic models.

One may use the inverse Laplace transform to obtain the spectral representation of the function χ for $\alpha, \gamma > 0$ (of the form in eq. (3.17)):

$$\chi(t;\alpha,\gamma) = \mathcal{L}^{-1}\Big[\frac{1}{s+\gamma\sqrt{s}+\alpha}\Big](t) \;\; = \frac{i}{\pi}\int_{-\infty}^{\infty} \frac{e^{-k^2 t}k}{-k^2+ik\gamma+\alpha}dk \;, \tag{3.23}$$

where the second equality, resulting in the integral over k, can be obtained by a suitable parameterization of the associated Bromwich contour for the inverse Laplace transform (Section 3.A). Depending on the sign of the discriminant of the quadratic expression in the denominator, $(\gamma^2 - 4\alpha)$, different closed-form expressions for the function χ may be obtained [79]. However, we retain its spectral representation. Since the semigroup property ought to hold for all $t \geq 0$, one may readily verify the lack of it by evaluating the function χ in eq. (3.23) at an arbitrary pair of t_1, t_2. Note that this is true even for $\alpha = 0$.

Remark 3.3. The lack of the semigroup property is not uncommon. Indeed, consider the second-order scalar ODE:

$$\frac{d^2w}{dt^2} - \alpha w = N(w(t), t).$$

The solution can be written in integral form as

$$w(t) = C_1 e^{\sqrt{\alpha}t} + C_2 e^{-\sqrt{\alpha}t} + \frac{1}{2\sqrt{\alpha}}\int_0^t (e^{\sqrt{\alpha}(t-\tau)} - e^{-\sqrt{\alpha}(t-\tau)})N(w(\tau),\tau)\,d\tau \;.$$

In the above description, w is the sole state variable and we have a non-Markovian process. Equivalently, the solution for the linear equation lacks the semigroup property. The linear solution for the above Cauchy problem is a linear combination of exponential functions. Whereas a single exponential function satisfies the semigroup property, a *linear combination* does not. A natural approach taken to study this example, analytically or numerically, is to write it as a Markovian system of two state-variables, $[w, dw/dt]^T$, each with its own dynamical evolution equation. We present this example to highlight the fact that functions lacking the semigroup property can arise naturally in physics. But we also stress that a Markovian embedding is a natural and common approach to address these kinds of problems. Indeed, our approach can also be thought of as a Markovian embedding but into a state-space of much higher dimension. For another example and similar interpretation, see [103][4].

[4] In [103], the author discusses a second order equation for a particle undergoing random acceleration: $d^2\phi/dt^2 = \eta(t)$, where η is a white noise and ϕ represents position. He argues that the process is non-Markovian since the value of $\phi(t+\Delta t)$ depends on both $\phi(t)$ and $\phi(t-\Delta t)$. A similar behavior prevails in our deterministic example, inferred through the lack of the semigroup property.

3.2.3 Markovian embedding of the MRG equation

Using the solution to the linear MRG equation $\chi(t;\alpha,\gamma)$, the solution to the nonlinear MRG equation can be expressed in the following integral equation form:

$$w(t) = \chi(t;\alpha,\gamma)w_0 + \int_0^t \chi(t-\tau;\alpha,\gamma)N(w(\tau),\tau)\,d\tau\ . \tag{3.24}$$

Remark 3.4. In ETD methods, the primary motivation for expressing the dynamical equation in integral form is to exactly integrate the stiff linear part while using numerical approximations for the non-stiff nonlinear term. In eq. (3.24), the integral form addresses the singularity, rather than the stiffness, of the linear MRG operator: $d/dt + \gamma d^{1/2}/dt^{1/2} + \alpha$. Notably, the integral kernel χ is well-behaved compared to the singular behavior of the original differential operator.

Following the discussion in section 3.2.2, we have for the solution $w(t)$ at time $t = t_{n+1}$ the following

$$w(t_{n+1}) = \mathcal{R}^{\chi}_{\text{history}}(t_n;t_{n+1}) + \int_0^{\Delta t} \chi(\Delta t-\tau;\alpha,\gamma)N(w(t_n+\tau),t_n+\tau)\,d\tau\ , \tag{3.25}$$

$$\text{where } \mathcal{R}^{\chi}_{\text{history}}(t_n;t_{n+1}) := \chi(t_{n+1};\alpha,\gamma)w_0 + \int_0^{t_n} \chi(t_{n+1}-\tau;\alpha,\gamma)N(w(\tau),\tau)\,d\tau\ ,$$

We note that the above are exact statements and do not involve any numerical approximation yet.

The expression for the solution at t_{n+1} in eq. (3.25) contains a residual term that captures the influence of the history of past states in the interval $[0,t_n]$ on $w(t_{n+1})$. We proceed to show, along the lines of the discussion in section 3.1.4, that we can introduce a co-evolving state variable, denoted by H and with its own dynamical equation, that can be used to construct an exact local representation of $\mathcal{R}^{\chi}_{\text{history}}$. The key requirement is that the spectral representation for the function χ, eq. (3.23), exists which allows a Markovian embedding of the MRG equation.

Remark 3.5. The representation of the MRG solution according to eq. (3.25) enables the simultaneous discretization approach suggested in section 3.1.4. A direct temporal discretization is applied to the most recent interval $[t_n,t_{n+1}]$ while a spectral discretization is used for the past history $[0,t_n]$.

Let $H(k,t)$ be a function of a real number k and time t related to the residual term

$\mathcal{R}^{\chi}_{\text{history}}$ in eq. (3.25) in the following manner

$$\mathcal{R}^{\chi}_{\text{history}}(t_n; t_{n+1}) = \int_{-\infty}^{\infty} H(k, t_n) e^{-k^2 \Delta t}\, dk \ . \tag{3.26}$$

Substitution of the spectral representation of the function χ, eq. (3.23), into the above definition of $\mathcal{R}^{\chi}_{\text{history}}$ yields the following definition for the newly introduced variable $H(k,t)$:

$$H(k,t) := \frac{i}{\pi}\Big(\frac{k e^{-k^2 t}}{-k^2 + ik\gamma + \alpha} w_0 + \int_0^t \frac{k e^{-k^2(t-\tau)}}{-k^2 + ik\gamma + \alpha} N(w(\tau), \tau)\, d\tau\Big). \tag{3.27}$$

Since the function H encodes the influence of past states on the current state, we refer to it as the history function. $H(\cdot, t)$ is a complex-valued function of the real number k and hence is an infinite-dimensional object.

From the form of the history function H in eq. (3.27), one can infer it has Markovian dynamics evolving according to the following ODE and initial condition,

$$\frac{dH}{dt} + k^2 H = \frac{i}{\pi} \frac{k N(w(t), t)}{(-k^2 + ik\gamma + \alpha)}, \quad H(k, 0) = \frac{i}{\pi} \frac{k}{(-k^2 + ik\gamma + \alpha)} w_0 \ . \tag{3.28}$$

Thus, upon the introduction of the history function as a new state variable which co-evolves with $w(t)$, we obtain the complete state that evolves 'locally' from t_n to t_{n+1} according to

$$\begin{aligned} w(t_{n+1}) &= \int_{-\infty}^{\infty} H(k, t_n) e^{-k^2 \Delta t}\, dk + \int_0^{\Delta t} \chi(\Delta t - \tau; \alpha, \gamma) N(w(t_n + \tau), t_n + \tau) d\tau \ , \\ H(k, t_{n+1}) &= e^{-k^2 \Delta t} H(k, t_n) + \frac{i}{\pi} \int_0^{\Delta t} \frac{k e^{-k^2(\Delta t - \tau)}}{(-k^2 + ik\gamma + \alpha)} N(w(t_n + \tau), t_n + \tau)\, d\tau \ . \end{aligned} \tag{3.29}$$

We re-emphasize that there has been no numerical approximation yet. Equation (3.29) is an equivalent way to write eq. (3.25) (which is simply the integral version of eq. (3.7b)).

We prefer to work with real-valued functions and note that $H(-k,t) = \overline{H(k,t)}$ (overbar indicates complex conjugate, see eq. (3.27). To this end, we introduce the following simplifying re-definitions of variables and functions :

$$k\sqrt{\Delta t} \to k, \quad \text{Re}\Big(\frac{2}{\sqrt{\Delta t}} H(k/\sqrt{\Delta t}, t)\Big) \to H(k,t).$$

Next, we prefer working with the function $\chi(t; \alpha = 0, \gamma)$ which has an explicit form in terms of the complementary error function. This allows us to better handle integrals involving the history function that will appear in the subsequent sections. Therefore, we absorb the linear term proportional to α in eq. (3.7) into the nonlinear term. Hence, we introduce the

following definitions:

$$\bar{\gamma} = \gamma\sqrt{\Delta t}, \quad \chi(t;\gamma) := \chi(t;0,\gamma) = e^{\gamma^2 t}\mathrm{erfc}(\gamma\sqrt{t}) \ , \quad N_\alpha(w) = N(w) - \alpha w \ . \tag{3.30}$$

Under the above transformations, we rewrite the evolution rule for the new inflated state eq. (3.29) in the integral-equation form:

$$w(t_{n+1}) = \int_0^\infty H(k,t_n)e^{-k^2}\, dk + \int_0^{\Delta t} \chi(\Delta t - \tau;\bar{\gamma}) N_\alpha(w(t_n+\tau), t_n+\tau)\, d\tau, \tag{3.31a}$$

$$H(k,t_{n+1}) = e^{-k^2}H(k,t_n) + \int_0^{\Delta t} \frac{2\tilde{\gamma}e^{-k^2(1-\tau/\Delta t)}}{\pi(k^2+\bar{\gamma}^2)} N_\alpha(w(t_n+\tau), t_n+\tau)\, d\tau. \tag{3.31b}$$

where H is now a real-valued function. One may note on comparing eq. (3.31a) with eq. (3.25) in the original framework that we have effectively replaced the nonlocal residual term with a local-in-time term. This, of course, has come at the cost of introducing eq. (3.31b) for H. The new state description $[w(t), H(k,t)]^T$ is larger compared to the original description. However, owing to the local evolution rules for $[w(t), H(k,t)]^T$, standard algorithms such as RK-ETD can be adapted for time-stepping. The associated memory and computational costs to advance the state become independent of simulation time. Thus, to find the Markovian embedding, we only needed the spectral representation for the function χ. In the next section, we describe numerical time-integration schemes to evolve the new Markovian state according to eq. (3.31).

3.3 Explicit multi-stage time-integrator for the MRG equation

We summarize our progress so far. We begin with eq. (3.7b) that prescribes the evolution of the slip velocity for an idealized inertial particle in a viscous fluid. We intend to find numerical approximations to this equation on a discrete time-grid with Δt representing the temporal discretization. We recall the following notation from eq. (3.30),

$$\bar{\gamma} = \gamma\sqrt{\Delta t}, \quad \chi(t;\gamma) = e^{\gamma^2 t}\mathrm{erfc}(\gamma\sqrt{t}) \ , \quad N_\alpha(w) = N(w) - \alpha w \ .$$

Note $w, N(w), N_\alpha(w)$ are typically $d-$dimensional real-valued vectors in the MRG equation. Based on the discussions in the previous section, the solution to the embedded MRG equation at time t_{n+1} satisfies eq. (3.31) where $H(k,t_n)$ is also a $d-$dimensional real-valued vector for each $k \in \mathbb{R}$.

In this section, we outline the multi-stage time-integrator for the MRG equation rewritten under the Markovian embedding according to eq. (3.31). We provide details of the derivation

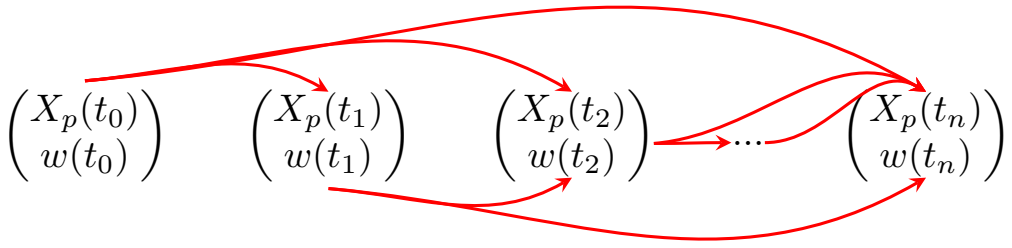

(a)

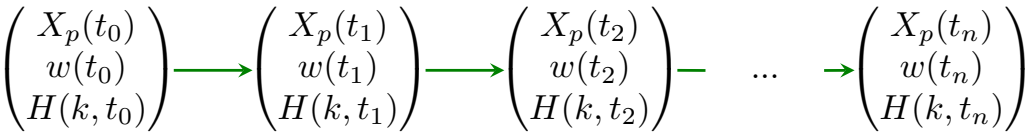

(b)

Figure 3.2.1: A schematic for the Markovian embedding procedure for the MRG equation (Section 3.3). (a) Non-local inter-state interaction in the original representation, eq. (3.7). Interaction between no two states is the same. (b) Local interaction via eq. (3.31) due to inflated state description with the introduction of new 'history function', $H(k,t)$ All local interactions are identical.

in section 3.4. We refer to these integrators as RK-χTD schemes as they are counterparts to the RK-ETD schemes of [3]. We introduce grid functions $w_n, H_n(k)$ which are the numerical approximations of their exact counterparts $w(t_n), H(k,t_n)$ respectively. In addition, we have $\{w_{ni}\}$ which are numerical approximations of the exact solution constructed at intermediate stages, $\tau_{ni} = t_n + c_i\Delta t$.

We propose the following $\check{s}-$stage, explicit RK-χTD scheme for advancing the inflated state from t_n to t_{n+1}, given $[w_n, H_n(k)]^T$, for all $n \geq 0$,

$$w_{n1} = w_n, \tag{3.32a}$$

$$w_{nj} = \int_0^\infty H_n(k) e^{-c_j k^2}\, dk + \Delta t \sum_{i=1}^{j-1} a_{ji}(\Delta t) N_\alpha(w_{ni}, \tau_{ni}), \quad 2 \leq j \leq \check{s}, \tag{3.32b}$$

$$w_{n+1} = \int_0^\infty H_n(k) e^{-k^2}\, dk + \Delta t \sum_{i=1}^{\check{s}} b_i(\Delta t) N_\alpha(w_{ni}, \tau_{ni}), \tag{3.32c}$$

$$H_{n+1}(k) = e^{-k^2} H_n(k) + \frac{2}{\pi} \frac{\bar{\gamma}}{\bar{\gamma}^2 + k^2} \Delta t \sum_{i=1}^{\check{s}} d_i(k) N_\alpha(w_{ni}, \tau_{ni}), \tag{3.32d}$$

where $[a_{ji}]$ is the $\check{s} \times \check{s}$ *RK matrix*, $\{b_i\}, \{d_i(k)\}$ are scheme-specific *weights*, and $\{0 \leq c_i \leq 1\}$

are the *explicit RK nodes*. The initial conditions for the solver are:

$$[w_0, H_0(k)]^T = \left[w_0, \frac{2}{\pi}\frac{\bar{\gamma}}{k^2+\bar{\gamma}^2}w_0\right]^T \ . \tag{3.33}$$

The *Butcher tableau* representation for the nodes and weights in eq. (3.32) is,

$$\begin{array}{c|ccccc} c_1 = 0 & & & & & \\ c_2 & a_{21} & & & & \\ . & ... & & & & \\ c_{\check{s}} & a_{\check{s}1} & a_{\check{s}2} & ... & a_{\check{s},\check{s}-1} & \\ \hline & b_1 & b_2 & ... & & b_{\check{s}} \\ & d_1(k) & d_2(k) & ... & & d_{\check{s}}(k) \end{array} \tag{3.34}$$

We set $c_1 = 0$ and $a_{i,j\geq i} = 0$ to construct an explicit scheme. The above representation differs slightly from the standard *Butcher* representation in that there is an extra row of information for the functions d_i corresponding to the weights for the evolution of the history function eq. (3.32d). For a user-defined choice of nodes c_i, an $\check{s}-$stage scheme has $\check{s}(\check{s}+3)/2$ unknown coefficients to be fixed. We introduce the following shorthand notations for the recurring functions used in defining the scheme-specific weights-

$$\begin{gathered} \phi_{m,n} = \int_I \chi(c_n(1-\tau);\bar{\gamma})\tau^m \, d\tau \ , \quad \phi_m = \int_I \chi(1-\tau;\bar{\gamma})\tau^m \, d\tau \ , \\ \psi_m(k) = \int_I e^{-k^2(1-\tau)}\tau^m \, d\tau, \end{gathered} \tag{3.35}$$

where interval $I = [0,1]$, n is an integer index (≥ 1) labelling the RK nodes, and m is a positive real number. These parameters are pre-computed once $\Delta t, \bar{\gamma}$ are specified.

3.3.1 Two-stage, first-order RK-χTD method

The two-stage, explicit RK method is constructed using the following order conditions:

$$\sum_{j=1}^{2} c_j^{(i-1)/2} b_j = \phi_{(i-1)/2}, \quad 1 \leq i \leq 2 \ , \tag{3.36a}$$

$$\sum_{j=1}^{2} c_j^{(i-1)/2} d_j(k) = \psi_{(i-1)/2}(k), \quad 1 \leq i \leq 2 \ , \tag{3.36b}$$

$$a_{21} = c_2\phi_{0,2} \ , \tag{3.36c}$$

where c_2 is a free parameter, leading to the following one-parameter family of schemes,

$$\begin{array}{c|cc} 0 & & \\ c_2 & c_2\phi_{0,2} & \\ \hline & \phi_0 - \frac{1}{c_2^{1/2}}\phi_{1/2} & \frac{1}{c_2^{1/2}}\phi_{1/2} \\ & \psi_0(k) - \frac{1}{c_2^{1/2}}\psi_{1/2}(k) & \frac{1}{c_2^{1/2}}\psi_{1/2}(k) \end{array} \tag{3.37}$$

We choose $c_2 = 1$ to obtain a global error that scales linearly with Δt.

3.3.2 Four-stage, second-order RK-χTD method

This four-stage scheme can be constructed analogous to the two-stage scheme by satisfying the following order conditions using four intermediate stages-

$$\sum_{j=1}^{4} c_j^{(i-1)/2} b_j = \phi_{(i-1)/2}, \quad 1 \le i \le 4, \tag{3.38a}$$

$$\sum_{j=1}^{4} c_j^{(i-1)/2} d_j(k) = \psi_{(i-1)/2}(k), \quad 1 \le i \le 4, \tag{3.38b}$$

$$\sum_{i=1}^{j-1} a_{ji} = c_j \phi_{0,j}, \quad 2 \le j \le 3, \tag{3.38c}$$

$$b_3 a_{32} c_2^{1/2} = b_3 c_3^{3/2} \phi_{\frac{1}{2},3} + b_2 c_2^{3/2} \phi_{\frac{1}{2},2}, \tag{3.38d}$$

$$\sum_{j=1}^{3} a_{4j} c_j^{(i-1)/2} = c_4^{(i+1)/2} \phi_{(i-1)/2,4}, \quad 1 \le i \le 3 \tag{3.38e}$$

where once again, besides setting $c_1 = 0$, the choice of rest of the nodes as free parameters leads to the following three-parameter family of schemes-

$$\begin{array}{c|cccc} 0 & & & & \\ c_2 & c_2\phi_{0,2} & & & \\ c_3 & c_3\phi_{0,3} - a_{32} & \frac{b_3 c_3^{3/2}\phi_{\frac{1}{2},3} + b_2 c_2^{3/2}\phi_{\frac{1}{2},2}}{b_3 c_2^{1/2}} & & \\ c_4 & c_4\phi_{0,4} - a_{42} - a_{43} & \frac{c_4^2\phi_{1,4}}{c_2} - \frac{c_3}{c_2}a_{43} & \frac{c_2^{1/2} c_4^{3/2}\phi_{\frac{1}{2},4} - c_4^2\phi_{1,4}}{(c_2 c_3)^{1/2} - c_3} & \\ \hline & b_1 & b_2 & b_3 & b_4 \\ & d_1(k) & d_2(k) & d_3(k) & d_4(k) \end{array} \tag{3.39}$$

In the above, b_i's, d_i's are obtained by solving the matrix equations, eqs. (3.38a) and (3.38b), once a choice for the nodes c_j is made. With the b_i, d_i at hand, we compute a_{ij} from right-to-left (see eq. (3.34) for Butcher tableau notation). It is important to choose the c_j's carefully such that the matrices in eq. (3.38) are invertible. We use the following choice for the nodes- $(0, 0.25, 0.9, 1)$. The estimated convergence rate is $(\Delta t)^2$.

3.4 Derivation of the numerical scheme and error analysis

Following Hochbruck & Ostermann [101], our construction of the schemes in section 3.3 relies on the following representation of the exact solution at arbitrary times (a generalization of eq. (3.31a)):

$$w(t_n + \theta\Delta t) = \int_0^\infty e^{-\theta k^2} H(k, t_n)\, dk + \int_0^{\theta\Delta t} \chi(\theta\Delta t - \tau; \bar{\gamma}) N_\alpha(w(t_n + \tau), t_n + \tau)\, d\tau \ , \quad (3.40)$$

where $\theta \in (0, 1]$. We derive the RK-quadrature formulae to approximate the time-integral over $[0, \theta\Delta t]$ up to a desired accuracy. The additional task is the computation of the history integral over k in eq. (3.40). Our strategy is to ensure that the error due to approximation of the history integrals is subdominant to that due to approximation of the time-integrals (see section 3.4.2). Thus, when we derive the RK weights in section 3.4.1, we retain the semi-infinite integral for $H(k, t_n)$ in the representation of the history integral.

In deriving the RK-quadrature formulae, we seek an expansion for the nonlinear function $N_\alpha(w(t), t)$ in the neighborhood of a time-grid point $t = t_n$. We assume a function $\check{N}_\alpha$ such that $\check{N}_\alpha(t) = N_\alpha(w(t), t)$. Typically, one would use a Taylor series expansion of $\check{N}_\alpha(t)$ around $t = t_n$ to derive the quadrature but the MRG equation warrants a different expansion. We highlight that the function $\chi(t; \bar{\gamma})$ has a series expansion in powers of $t^{1/2}$ around $t = 0$:

$$\chi(t \to 0; \bar{\gamma}) \sim 1 - \frac{2}{\sqrt{\pi}} \bar{\gamma} \sqrt{t} + \bar{\gamma}^2 t + ...$$

which implies lack of smoothness at $t = 0$. However, there is a regular expansion in integer powers of t at later times $t > 0$. Using standard arguments, one can show that this series expansion implicitly holds for the solution function $w(t)$ as well as for $N_\alpha(w)$ (see eq. (3.24)). This allows us to write the following expansion for the function N_α around $t = t_n$:

$$N_\alpha(w(t_n + \tau), t_n + \tau) = \check{N}_\alpha(t_n + \tau) = \sum_{m=0}^{\infty} C_m(t_n) \tau^{m/2}, \quad \forall n \ , \quad (3.41)$$

with coefficients C_m that are functions of the 'base point' t_n. Note that the above represen-

tation uniformly captures both the short-time and the long-time behavior: at $t_n = 0$ these coefficients are non-zero, capturing the singular behavior of the MRG solution accurately, while at later-times the odd-indexed coefficients become zero, recovering a regular Taylor series expansion.

In section 3.D, we present two toy problems to illustrate the need for standard and non-standard series expansions depending on the smoothness of the solution.

3.4.1 Computation of the RK matrix and weights

The state variable whose error we want to control is the slip velocity $w(t)$. Therefore, we introduce the primary error function $e_n = w_n - w(t_n)$, and the auxiliary error functions, $E_{ni} = w_{ni} - w(\tau_{ni})$ and $e_n^H(k) = H_n(k) - H(k, t_n)$, which denote the difference between exact state variables and their numerical counterparts. We subtract eq. (3.31a) from eq. (3.32c) to get the following master equation for the primary error function for any n,

$$e_{n+1} = \int_0^\infty e^{-k^2} e_n^H(k)\, dk + \Delta t \sum_{i=1}^{\check{s}} b_i \Big[N_\alpha(w_{ni}, \tau_{ni}) - N_\alpha(w(\tau_{ni}), \tau_{ni}) \Big] + \delta_{n+1} \ . \tag{3.42}$$

The different contributions to the primary error function are: (i) the defect term δ_{n+1} represents error solely due to the RK approximation of the exact time-integral, (ii) the terms proportional to $N_\alpha(w_{ni}, \tau_{ni}) - N_\alpha(w(\tau_{ni}), \tau_{ni})$ represent error due to the differential action of the nonlinear function N_α on exact and the numerical counterpart of the state variable, and (iii) the integral term contains the error due to numerical approximation of the history function. We derive conditions called *order conditions* that fix the RK matrix and weights by controlling error from each contribution. This control is designed such that the numerical method eq. (3.32) converges with order p, i.e., the error function $e_n \sim \mathcal{O}(\Delta t^p)$ as $\Delta t \to 0$.

(i) First, we estimate the defect term δ_{n+1} in terms of Δt. The RK weights $\{b_i\}$ are fixed by controlling this defect. We evaluate the numerical scheme eq. (3.32c) at the exact state, i.e., we substitute $w_{ni} = w(\tau_{ni}), w_n = w(t_n), H_n(k) = H(k, t_n)$, yielding,

$$w(t_{n+1}) = \int_0^\infty H(k, t_n) e^{-k^2}\, dk + \Delta t \sum_{i=1}^{\check{s}} b_i N_\alpha(w(\tau_{ni}), \tau_{ni}) - \delta_{n+1} \tag{3.43}$$

where the defect δ_{n+1} reflects error due to the RK-quadrature. We subtract the above from the exact expression for $w(t_{n+1})$ in eq. (3.31a) and use a truncation of the series expansion

in eq. (3.41) to get the following expression for the defect term:

$$\begin{aligned}\delta_{n+1} &= \Delta t \sum_{i=1}^{\check{s}} b_i N_\alpha(w(\tau_{ni}), \tau_{ni}) - \int_0^{\Delta t} \chi(\Delta t - \tau; \bar{\gamma}) N_\alpha(w(t_n + \tau), t_n + \tau)\, d\tau \\ &= \sum_{m=1}^{p_1} C_{m-1}(t_n) \Delta t^{\frac{m+1}{2}} \left[\sum_{i=1}^{s} b_i c_i^{(m-1)/2} - \phi_{(m-1)/2}(\bar{\gamma}) \right] + \mathcal{O}(\Delta t^{\frac{p_1}{2}+1}) \ ,\end{aligned} \tag{3.44}$$

where p_1 is a positive integer indicating the extent of truncation. The expression in the parenthesis, parameterized by index m, are generators of p_1-number of order conditions. The order conditions eqs. (3.36a) and (3.38a) result from setting these expressions for $m \leq p_1 = \check{s}$ to zero. As a result, across the two schemes in section 3.3, we have

$$\delta_{n+1} \sim \mathcal{O}(\Delta t^{\frac{\check{s}}{2}+1}) \ . \tag{3.45}$$

(*ii*) Next, we estimate the error due to the differential nonlinear action of the function N_α. The RK matrix, $[a_{ij}]$, is fixed by controlling this contribution. We recall the stage error function, $E_{ni} = w_{ni} - w(\tau_{ni})$, and state the following relation (Section 3.B):

$$N_{n,i}^{\text{diff}} := N_\alpha(w_{ni}, \tau_{ni}) - N_\alpha(w(\tau_{ni}), \tau_{ni}) = J_n E_{ni} + \mathcal{O}(E_{ni}\sqrt{\Delta t}) \tag{3.46}$$

where $J_n = \partial N_\alpha / \partial w$ at $t = t_n$. Substituting this in the second term on the right-hand side in eq. (3.42) results in the leading order contribution from the term $\Delta t \sum_{i=1}^{\check{s}} b_i J_n E_{ni}$. Therefore, we estimate the stage error function, E_{ni}, by subtracting exact solution at the intermediate stage, τ_{ni} (set $\theta = c_i$ in eq. (3.40)), from the numerical expression eq. (3.32b):

$$\begin{aligned}E_{nj} &= \int_0^\infty e^{-c_j k^2} e_n^H(k)\, dk + \Delta t \sum_{i=1}^{j-1} a_{ji} N_{n,i}^{\text{diff}} + \delta_{nj}, \quad j > 1 \\ &= \int_0^\infty e^{-c_j k^2} e_n^H(k)\, dk + \Delta t \sum_{i=1}^{j-1} a_{ji} (J_n E_{ni} + \mathcal{O}(E_{ni}\sqrt{\Delta t})) + \delta_{nj},\end{aligned} \tag{3.47}$$

where δ_{nj} reflects error due to RK-quadrature at the intermediate stage. Note that $E_{n1} = e_n$, $\delta_{n1} = 0$. Order analysis of the stage errors, E_{nj}, follows similarly to eq. (3.42) due to identical error decomposition. Also note, due to recursive construction, the second term on the right in eq. (3.47) is subdominant to the rest of the terms. Thus, it is sufficient to check the contributions of δ_{nj} and e_n^H to the stage error E_{nj}.

We examine the term $\Delta t \sum_{i=1}^{\check{s}} b_i J_n \delta_{ni}$. An expression for δ_{nj} (for $j > 1$) can be obtained

by repeating the procedure followed for estimating δ_n:

$$\delta_{nj} = \sum_{m=1}^{p_{2,j}} C_{m-1}(t_n)\Delta t^{\frac{m+1}{2}} \left[\sum_{i=1}^{j-1} a_{ji} c_i^{(m-1)/2} - c_j^{(m+1)/2} \phi_{(m-1)/2,j}(\bar{\gamma}) \right] + \mathcal{O}(\Delta t^{\frac{p_{2,j}}{2}+1}) \ , \quad (3.48)$$

where $\{p_{2,j}\}$ are positive integers. Using the above expression, we collect terms of different powers of Δt in the expression $\Delta t \sum_{i=1}^{\check{s}} b_i J_n \delta_{ni}$ and set the coefficients to zero up to the desired order. For certain choices of $\{p_{2,j} < \check{s}\}$ (see table 3.4.1), these generate the order conditions eq. (3.36c) for the 2-stage scheme and eqs. (3.38c) to (3.38e) for the 4-stage scheme. The resultant contribution can be shown to be

$$\Delta t \sum_{i=1}^{\check{s}} b_i (N_\alpha(w_{ni}, \tau_{ni}) - N_\alpha(w(\tau_{ni}), \tau_{ni}) \sim \mathcal{O}(e_n^H(k)\Delta t) + \mathcal{O}(\Delta t^{\frac{\check{s}}{2}+1}) \ . \quad (3.49)$$

(*iii*) Finally, we estimate the error due to numerical approximation of the history function. This fixes the weight functions $\{d_i(k)\}$. We derive an equation for the history error function, $e_n^H(k) = H_n(k) - H(k, t_n)$, by subtracting eq. (3.31b) from eq. (3.32d) :

$$e_{n+1}^H(k) = e^{-k^2} e_n^H(k) + \frac{2}{\pi} \frac{\bar{\gamma}}{k^2 + \bar{\gamma}^2} \Delta t \sum_{i=1}^{\check{s}} d_i(k) N_{n,i}^{\text{diff}} + \delta_{n+1}^H(k) \ . \quad (3.50)$$

We begin by estimating the history-defect term, δ_{n+1}^H, whose expression is derived by subtracting eq. (3.32d) evaluated at the exact state variables from eq. (3.31b) :

$$\delta_{n+1}^H(k) = \sum_{m=1}^{p_3} C_{m-1}(t_n)\Delta t^{\frac{m+1}{2}} \left[\sum_{i=1}^{\check{s}} d_i(k) c_i^{(m-1)/2} - \psi_{(m-1)/2}(k) \right] + \mathcal{O}(\Delta t^{\frac{p_3}{2}+1}) \ , \quad (3.51)$$

where p_3 is a positive integer. Setting the expression in the parenthesis to zero for $m \leq p_3 = \check{s}$ generates as many order conditions for $d_i(k)$ for every k. Therefore, we solve for $d_i(k)$'s (eqs. (3.36b) and (3.38b)). So far, we have fixed all the parameters in our RK scheme, namely $a_{ij}, b_i, d_i(k)$. Demanding that any further conditions be satisfied would result in contradiction from the already derived order conditions. As a result, we assess eq. (3.50) under the constraints of the derived order conditions.

Let $\rho(k) := (2/\pi)(\bar{\gamma}/(k^2 + \bar{\gamma}^2))$. Using the history error function in eq. (3.50) recursively, we get

$$e_{n+1}^H(k) = e^{-(n+1)k^2} e_0^H(k) + \rho(k)\Delta t \sum_{m=0}^{n} \sum_{i=1}^{\check{s}} d_i(k) e^{-mk^2} N_{n-m,i}^{\text{diff}} + \sum_{m=0}^{n} e^{-mk^2} \delta_{n+1-m}^H(k), \quad (3.52)$$

where the first term has no contribution since $e_0^H(k) = 0$ by imposition of the exact initial condition. Further, since eq. (3.51) and $(n+1)\Delta t = t_{n+1}$, the last term can be shown to be $\mathcal{O}(\Delta t^{\frac{\breve{s}}{2}})$. Using eq. (3.46) and a similar argument as before that the major contribution to E_{ni} in $\Delta t \sum_{i=1}^{\breve{s}} d_i(k) J_n E_{ni}$ comes from $e_n^H(k)$ and δ_{ni}, the second term in eq. (3.52) can be shown to be (see section 3.C for contribution from δ_{ni}):

$$\begin{aligned}\Delta t \sum_{m=0}^{n} \sum_{i=1}^{\breve{s}} d_i(k) e^{-mk^2} N_{n-m,i}^{\text{diff}} &\sim \Delta t \sum_{m=0}^{n} \sum_{i=1}^{\breve{s}} d_i(k) e^{-mk^2} J_{n-m} E_{n-m,i} \\ &\sim \Delta t \sum_{m=0}^{n} \sum_{i=1}^{\breve{s}} d_i(k) e^{-(n-m)k^2} \mathcal{D}_{m,i} + \mathcal{O}(\Delta t^{\frac{\breve{s}}{2}})\end{aligned} \tag{3.53}$$

where $\mathcal{D}_{m,i} = J_m \int_0^\infty e^{-c_i q^2} e_m^H(q)\, dq$. Combining the above estimates, eq. (3.52) reduces to

$$e_{n+1}^H(k) = \rho(k) \Delta t \sum_{i=1}^{\breve{s}} d_i(k) \widetilde{\mathcal{D}}_{n,i} + \mathcal{O}(\Delta t^{\frac{\breve{s}}{2}}) \,. \tag{3.54}$$

where $\widetilde{\mathcal{D}}_{n,i} = \int_0^\infty e^{-c_i q^2} \Big(\sum_{m=0}^{n} e^{-k^2(n-m)} J_m e_m^H(q) \Big)\, dq$. Using mathematical induction for different n, we can show the following,

$$e_{n+1}^H(k) \sim \mathcal{O}(\Delta t^{\frac{\breve{s}}{2}}) \implies \int_0^\infty e^{-k^2} e_n^H(k)\, dk \sim \mathcal{O}(\Delta t^{\frac{\breve{s}}{2}}) \,. \tag{3.55}$$

As a result of the contributions discussed above, we have $e_{n+1} \sim \mathcal{O}(\Delta t^{\frac{\breve{s}}{2}})$.

Table 3.4.1: Parameters used to control the defects $(\delta_n, \{\delta_{nj}\}, \delta_n^H)$ for $(\Delta t)^p$-accurate RK schemes.

$\breve{s}$	p_1	j	$p_{2,j}$	p_3	p
2	2	2	1	2	1
4	4	2	2	4	2
		3	2		
		4	3		

3.4.2 Computation of the history integral

We use the Clenshaw-Curtis quadrature to approximate the history integrals in the scheme eq. (3.32). As a prerequisite, we map the semi-infinite interval $k \in [0, \infty)$ to $\tilde{k} \in [-1, 1]$ under the transformation $k = \sqrt{\bar{\gamma}}(1+\tilde{k})/(1-\tilde{k})$. We expand the resulting integrand in this

interval in the basis of Chebyshev polynomials of the first kind, $\{T_m\}$. In summary,

$$\int_0^\infty e^{-k^2} H_n(k)\, dk = \int_{-1}^1 e^{-k(\tilde{k})^2} H_n(k(\tilde{k})) \frac{dk}{d\tilde{k}}\, d\tilde{k} =: \int_{-1}^1 F_n(\tilde{k})\, d\tilde{k} \approx \sum_{m=1}^{M+1} \mu_m F_n(\tilde{k}_m) \ ,$$

where $\{\tilde{k}_m = \cos(\theta_m)\}$ are the Chebyshev nodes computed at linearly-spaced $\theta_m = \pi(m-1)/M$, and $\{\mu_m\}$ are the associated weights. This procedure yields spectral accuracy with respect to the number of quadrature points, $M+1$. We note that this quadrature is a recurring operation of a *fixed* cost, performed at every time-iterate as the integrand contains a dynamically evolving state variable, $H_n(\cdot)$.

The RK weights derived in the previous section assumed that there is no quadrature error incurred in computing the history-error integral (first term on the right-hand side in eq. (3.42)). We show that it is effectively justified as long as quadrature error is subdominant to the time-stepping error from the RK-quadrature for time-integrals. We estimate the error due to the approximation of the history integral in the schemes. We define an associated error quantity, ζ_n, with the following decomposition:

$$\begin{aligned}
\zeta_n &:= \sum_{m=1}^{M+1} \mu_m F_n(\tilde{k}_m) - \int_0^\infty e^{-k^2} H(k, t_n)\, dk \ , \\
&= \int_0^\infty e^{-k^2} (H_n(k) - H(k, t_n))\, dk + \Big(\sum_{m=1}^{M+1} \mu_m F_n(\tilde{k}_m) - \int_0^\infty e^{-k^2} H_n(k)\, dk \Big), \\
&= \int_0^\infty e^{-k^2} e_n^H(k)\, dk + \zeta_n^Q \ ,
\end{aligned}$$

where ζ_n^Q is the error solely due to the quadrature approximation of the history-error integral (in our case the Clenshaw-Curtis quadrature) while the remaining integral term is what appears in the master error eq. (3.42). In principle, any quadrature can be used, and the associated convergence property will be reflected in ζ_n^Q. This justifies our assumption that this quantity virtually sets the "machine precision" for the scheme. The effect of the quadrature error in computing the history integral is shown in the error convergence plots in fig. 3.5.1e and fig. 3.5.2.

3.5 Numerical results

In this section, we test the error bounds for the first- and second-order Runge-Kutta schemes for the MRG equation described in sections 3.3.1 and 3.3.2 for two model problems.

3.5.1 Oscillating-in-time force

We consider the scalar MRG equation eq. (3.7b) with a time-oscillating force, $N(t) = \sin(\omega t)$, decoupled from the position dynamics, for $t \in (0, T]$, subject to the initial condition $w(0) = w_0$. This example has the following closed-form analytical solution expression (section 4.3 in [37]):

$$w(t) = \chi(t; \alpha, \gamma) w_0 + \int_0^\infty \frac{2\gamma k^2}{\pi \left((-k^2 + \alpha)^2 + k^2\gamma^2\right)} \left(\frac{k^2 \sin(\omega t) - \omega \cos(\omega t) + \omega e^{-k^2 t}}{k^4 + \omega^2} \right) dk \ , \tag{3.56}$$

where the semi-infinite $k-$ integral may be computed numerically using any available standard high-accuracy quadrature package. We used MATLAB's built-in numerical integrator function *integral* to generate the exact solution data. We numerically evolve the forced MRG equation over discrete times $t_n = n\Delta t$ using the two schemes given in section 3.3 for a chosen set of parameters. According to the construction of the schemes, the two- and four-stage scheme should generate first- and second-order rates of convergence for global error, respectively. This is verified in fig. 3.5.1c, where the error is measured in the l_2-norm

$$l_2\text{-error} = \left(\Delta t \sum_{n=1}^{N_T} |w_n - w(t_n)|^2 \right)^{1/2} . \tag{3.57}$$

where $T = N_T \Delta t$.

Additionally, in fig. 3.5.1d, we measure the computational effort demanded by the schemes to improve in accuracy. We use CPU time taken to run the simulation up to $T = N_T \Delta t$ as proxy to estimate the operational cost (FLOPs) incurred by the schemes, and plot it against the global error. In the non-Markovian treatment of the equation in the original formalism (eq. (3.7)), the CPU time scales quadratically with the number of time-iterates, N_T, equivalently, Δt^{-2}. In contrast, in our Markovian reformulation, we recover the linear scaling for a canonical dynamical system (equivalently, Δt^{-1}).

3.5.2 Particle in 2D Lamb-Oseen vortex

The Lamb-Oseen vortex, a canonical structure in turbulent flows, provides a vector example of a particle moving according to the MRG equation in a 2D stationary flow field, without gravity. This problem, in addition to the vector equations for the particle slip velocity w coupled via the flow vector field, requires simultaneous evolution of the particle position vector $\boldsymbol{X}_p$ to determine the instantaneous nonlinear forcing of the flow at the particle location. We solve the MRG system eq. (3.7) using the schemes in section 3.4 in the interval

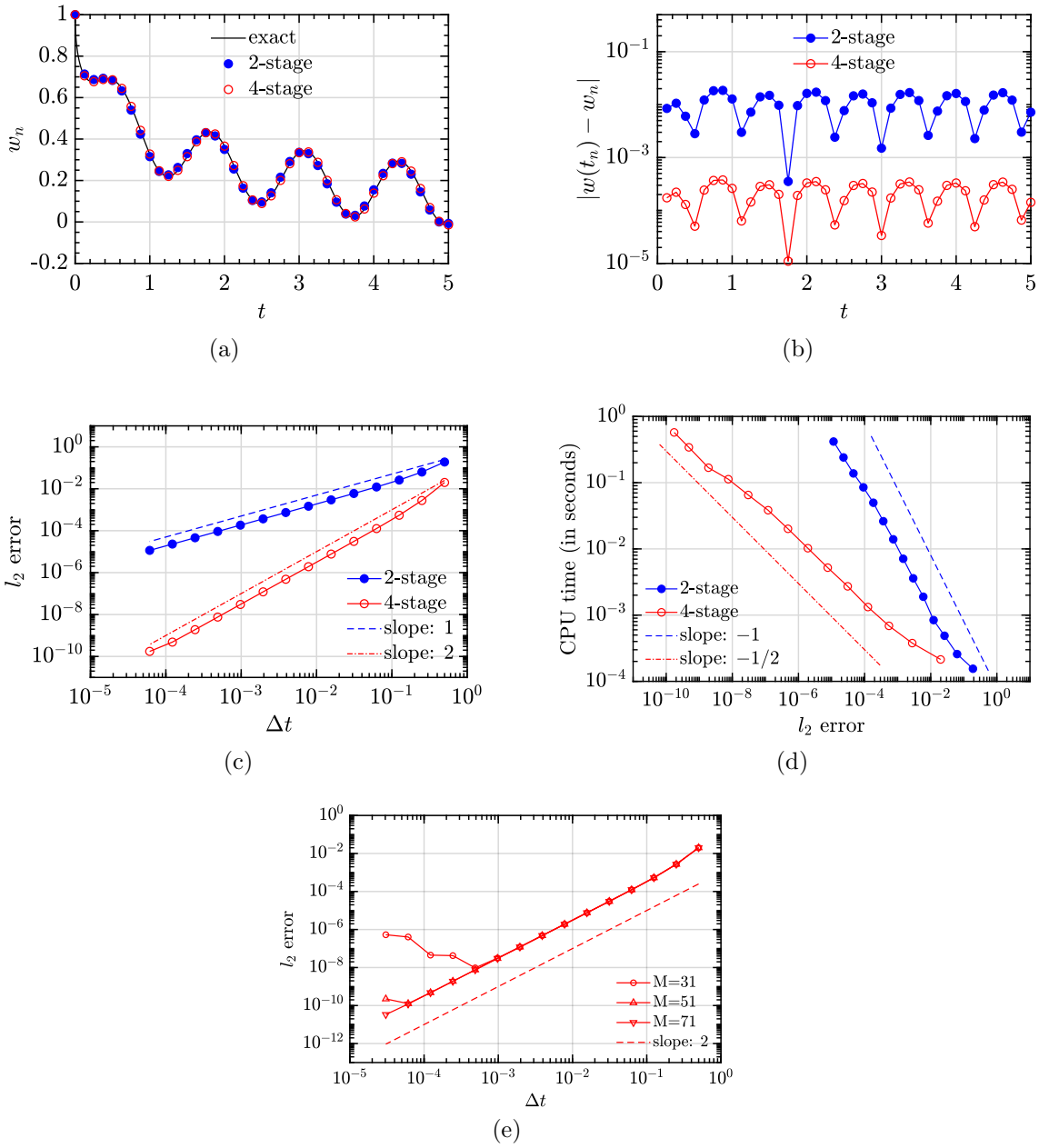

Figure 3.5.1: Scalar MRG equation forced with $N = \sin(\omega t)$, subject to initial condition, $w_0 = 1$, for the parameters $(\alpha, \gamma, \omega, T) = (0.33, 1, 5, 5)$, solved using the 2- and 4-stage schemes (eqs. (3.36) and (3.38)). $M = 51$ quadrature points were used to compute the history integral. (a) Comparison of exact and the numerical solutions for $\Delta t = 2^{-3}$. (b) Error as a function of time for $\Delta t = 2^{-3}$. (c) Scaling of error with time-step Δt. The errors are measured against the analytical solution (3.56) in the l_2-norm. (d) Scaling of CPU time with error. As per the schemes, l_2 error $\sim \Delta t^p$, where p is the order of accuracy, and operational cost $\sim \Delta t^{-1}$, which is verified by the slopes of the lines. (e) Dependence of error on the number of quadrature points M used in computing the history integral.

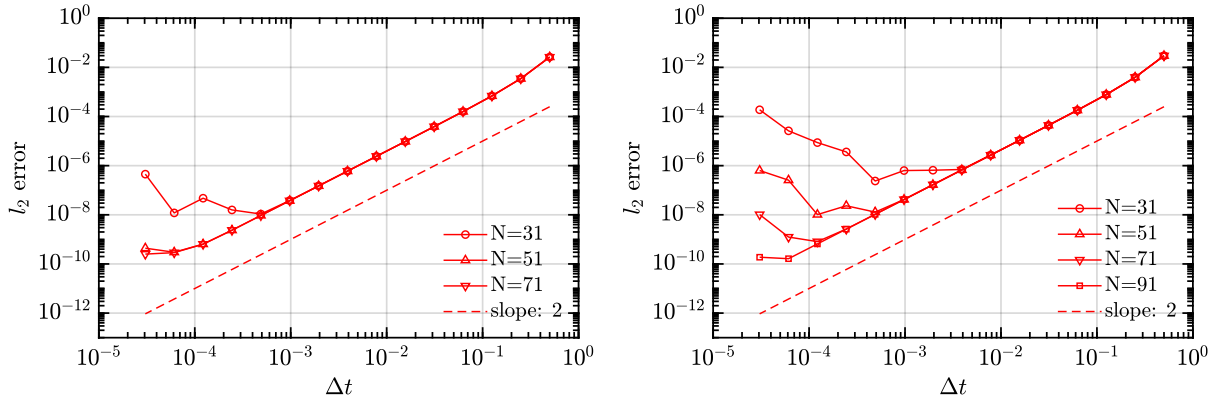

(a) $\gamma = 1/3$ ($\rho_p/\rho_f \sim 10$) (b) $\gamma = 1/30$ ($\rho_p/\rho_f \sim 10^3$)

Figure 3.5.2: Dependence of error convergence on the parameter shown for two representative γ's: smaller γ typically requires more quadrature nodes M to compute the history integral accurately. The quadrature error ζ_Q sets the 'machine precision' for the scheme, which can be favorably lowered by increasing the number of quadrature points for a given γ.

$t \in [0, T]$, subjected to initial conditions $[\boldsymbol{X}_{p0}, \boldsymbol{w}_0]^T$, and a 2D stationary Lamb-Oseen vortex, $u_\theta^\infty(r) = (1 - e^{-r^2})/r$, as the background flow, where $r = |\boldsymbol{x}| = (x_1^2 + x_2^2)^{1/2}$ and the subscript θ denotes the azimuthal direction.

Due to lack of an analytical solution expression for the slip velocity, we treat the numerical solution obtained at a finer grid resolution to be the true solution. We then define error in computing the slip velocity as the departure from the fine grid solution. Figure 3.5.3 verifies the expected error convergence rates for the two schemes eqs. (3.36) and (3.38).

The codes used for the examples in this section are available on GitHub at `https://github.com/jagannathan-divya/rk4mrg`.

3.6 An alternative Markovian embedding procedure

We revisit the alternative Markovian embedding construction in section 3.1.4 involving a direct discretization of the $H-$ equation to demonstrate the computational advantage of the construction in section 3.3.

Upon comparing the definitions of $w(t)$ in eqs. (3.18) and (3.29), one may infer the following relation for the history function in the alternative embedding eq. (3.18):

$$w(t_{n+1}) = \mathcal{R}^{\chi}_{\text{history}}(t_{n+1}; t_{n+1}) = \int_{-\infty}^{\infty} H(k, t_{n+1})\, dk \ . \tag{3.58}$$

We point out that the two different history functions H satisfy the same differential equation, but differ in their relation to the slip velocity $w(t)$. In eq. (3.29), H is introduced specifi-

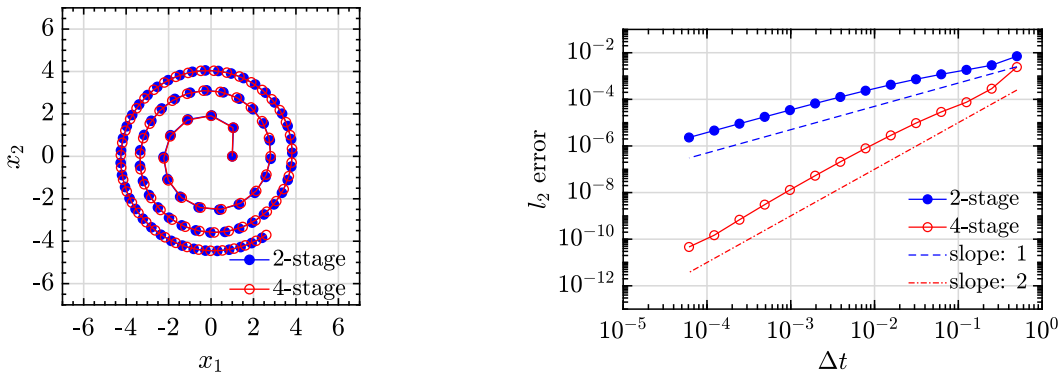

(a) (b)

Figure 3.5.3: Numerical advection of a particle in 2D stationary Lamb-Oseen vortex starting at $\boldsymbol{X}_{p0} = (1, 0)$, with non-zero initial slip velocity $\mathbf{w}_0 = (1, 0)$, for the parameters $(\alpha, \gamma) = (1, 1)$ using our 2-stage and 4-stage schemes. $M = 51$ (Chebyshev) quadrature points were used to compute the history integral. (a) Trajectory of the particle evolved up to $T = 200$ with $\Delta t = 2^{-3}$. (b) Scaling of error with time-step Δt for simulations run up to $T = 5$. Here, the errors are defined for the magnitude of slip velocity vector, $|\mathbf{w}|$, and measured in the l_2-norm against a fine-resolution numerical solution computed using our 4-stage scheme with $\Delta t = 2^{-16}$ and $M = 101$.

cally to account for the influence of past states on the present state, whereas in eq. (3.18) (equivalently eq. (3.58)) the function H accounts for all the states up to the present state. The rapid decay of the Gaussian multiplier in eq. (3.29) allows a *smaller* finite-dimensional approximation for H, keeping a low overall operational cost. In contrast, the lack of fast decay of the integrand in eq. (3.58) suggests that a quadrature approximation of the integral in eq. (3.58) will require a larger number of basis functions.

To show this, we introduce the following re-definitions,

$$\mathrm{Re}(H(k,t)) \to H(k,t), \quad N_\alpha(w) = N(w) - \alpha w \ , \tag{3.59}$$

where the first reassignment here is due to $\int \mathrm{Im}(H(k,t))\, dk = 0$ (see eq. (6.5)). We then consider the expansion of the history function in the basis of Hermite functions, $\{\Psi_m\}$,

$$H(k,t) = \sum_{m=0}^{M} \mu_{2m}(t)\Psi_{2m}(k) \ ,$$

where μ_m is an $(M+1) \times 1$ vector of time-dependent weights corresponding to the even-indexed Hermite functions. The odd-indexed Hermite functions do not contribute to the integral in eq. (3.58) due to their odd-symmetry. Substituting the Hermite expansion into

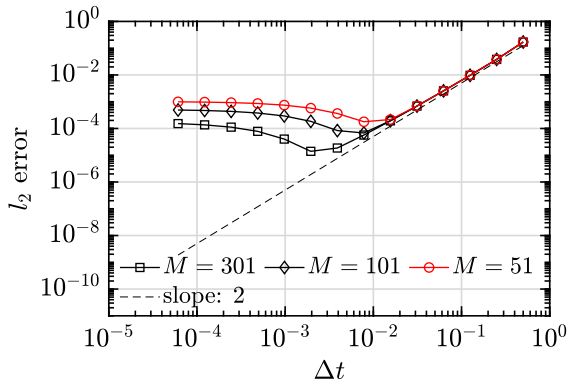

Figure 3.6.1: Repeat of numerical experiment in section 3.5.1 under the *alternative* Markovian embedding procedure (section 3.6) using ETD2RK (Eq. 81, 82 in [3]). M is the number of Hermite functions used to compute the history integral. Compare the red (open circle) curves here and in fig. 3.5.1c, both corresponding to $M = 51$.

eq. (3.28) with the re-definitions eq. (3.59), and taking suitable inner-products, we derive the following evolution rule for the Hermite coefficient-vector in the Duhamel form:

$$\boldsymbol{\mu}(t+\Delta t) = e^{-\mathbb{L}\Delta t}\boldsymbol{\mu}(t) + \boldsymbol{\eta}\int_0^{\Delta t} e^{-\mathbb{L}(\Delta t-\tau)} N_\alpha(w(t+\tau), t+\tau)\, d\tau, \tag{3.60}$$

where $\mathbb{L}$ is an $(M+1)\times(M+1)$ tri-diagonal matrix with elements $L_{mn} = \int k^2 \Psi_m(k)\Psi_n(k)dk$, and $\eta_{2m} = \gamma/\pi \int \Psi_{2m}(k)/(k^2+\gamma^2)\, dk$ is an $(M+1)\times 1$ vector. The exponential matrix, $e^{-\mathbb{L}\Delta t}$, is $\mathbb{V}e^{-\Lambda\Delta t}\mathbb{V}^{-1}$, where Λ is the diagonal matrix with eigenvalues of the matrix $\mathbb{L}$, and $\mathbb{V}$ is the corresponding eigenvector matrix. Equation (3.60) can be numerically solved using the RK-ETD method of [3]. The slip velocity can then be reconstructed by:

$$w(t+\Delta t) = \sqrt{2\pi}\sum_{m=0}^{M} \mu_{2m}(t+\Delta t)(-1)^m \Psi_{2m}(0)\ .$$

We repeat the numerical experiment in section 3.5.1 for the above construction using the second-order accurate ETD2RK scheme [3]. In fig. 3.6.1, we note that upon increasing the number of basis functions, the error in slip velocity converges with the rate $\mathcal{O}(\Delta t^2)$ over a range of Δt that only slowly widens before eventually saturating. In comparison, the 4-stage RK-χTD scheme eq. (3.38) derived under the Markovian embedding procedure required significantly fewer quadrature points to maintain the second-order accuracy over a much larger range of Δt (see fig. 3.5.1c).

The codes used for the example in this section are available on GitHub at `https://github.com/jagannathan-divya/rk4mrg`.

3.7 Conclusions and discussion

We have derived explicit integration schemes for the MRG equation via the introduction of a co-evolving state variable which we call the history function. We have further established their formal rates of convergence and presented some numerical experiments to verify the same. Both the introduction of the co-evolving state variable and the derivation of the numerical integration scheme relied crucially on the spectral representation of the solution to the linear equation. The ideas presented here generalize to any equation with memory effects which can be expressed in the following form along with the spectral representation of the linear solution operator along some contour Γ in the complex-k plane:

$$w(t) = \mathcal{T}(t)w_0 + \int_0^t \mathcal{T}(t-\tau)N(w(\tau),\tau)\,d\tau, \quad \mathcal{T}(t) = \int_\Gamma e^{f(k)t}g(k)\,dk\ . \tag{3.61}$$

This form includes many FDEs where the non-local term appears linearly, including notably the MRG equation. The form of the integrand in the definition of T in (3.61) determines the evolution equation for the co-evolving history function $H(k,t)$,

$$\frac{dH(k,t)}{dt} = f(k)H(k,t) + g(k)N(w(t),t)\ , \tag{3.62}$$

whereas the smoothness in t for the function $\mathcal{T}$ determines the kind of expansions (integer or fractional powers of t) involved in the derivation of the RK scheme. The resultant numerical schemes are local in time, self-starting, incur fixed memory cost throughout the simulation, and do not introduce any arbitrary design parameters (besides the step-size Δt). Typical numerical methods for equations with memory effects have computational costs that grow quadratically with simulation time, whereas our approach has the linear growth seen in equations without memory-effects due to the Markovian embedding.

We summarize the findings of this chapter:

- We propose a method to numerically integrate the MRG equation by embedding the equation into a larger Markovian system. We derive an RK method for the resulting system of equations. The explicit integrator thus constructed -
  - (a) is local in time, incurring operational costs that grow only linearly with simulation time,
  - (b) has constant memory storage and simulation restart cost,
  - (c) can admit non-zero initial conditions without loss of accuracy, and
  - (d) can be derived with tunable order of accuracy in the step-size Δt.

- We adapt the ideas of exponential time-differencing (ETD) in [3] to equations which do not possess a semigroup structure for the linear problem, while still maintaining a constant memory storage cost.

- Our method follows naturally from the existence of an exact spectral representation for the linear solution operator. Both the Markovian embedding and the need for expansions in powers of $t^{1/2}$ in the RK derivation are consequences of the spectral representation relevant to the MRG equation.

- Our method generalizes to other equations with memory effects, which includes FDEs, subject to the existence of the relevant spectral representation. We emphasize that the spectral representation for the linear solution (and its associated properties) dictates the development of the numerical method.

A comment on the use of the history function in the place of a non-local expression is in order. At first sight, it seems that both involve variables in infinite-dimensional space. However, the history function makes an impossible calculation viable as higher modes in its wave-number space lead to squared-exponentially smaller contributions, so a truncation is possible. This feature is true of any physical system, where viscous and other dissipative effects will erase out higher spatial wave-numbers. In any particulate flow, for example in atmospheric clouds, the number of particles is so large that a continuously increasing memory requirement would be difficult to accommodate, whereas our local representation makes it easier to contemplate.

Memory effects in evolution equations can appear nonlinearly. Indeed, this is the case for the evolution of moving boundary in the classical Stefan problem for phase change. Another notable example is the generalization of the MRG equation for finite Reynolds number presented in [16]. While these kinds of equations are not directly amenable to the method introduced in this chapter, suitable adaptations of the present method will work. The extension of the present method to problems with nonlinear non-local effects is considered in chapter 6.

Appendix

3.A Spectral representation of $\chi(t;\alpha,\gamma)$ using inverse Laplace transform

We have

$$\chi(t;\alpha,\gamma) = \mathcal{L}^{-1}\Big[\frac{1}{s+\gamma\sqrt{s}+\alpha}\Big](t) = \frac{1}{2\pi i}\int_{a-i\infty}^{a+i\infty} \frac{e^{st}}{s+\gamma\sqrt{s}+\alpha}\, ds$$

where the complex contour $(a - i\infty, a + i\infty)$ is the standard Bromwich's vertical contour such that all the singularities of the function $1/(s+\gamma\sqrt{s}+\alpha)$ lie to the left of it. We use the following parametric representation for complex s on this contour -

$$s = a(1 + i\tan\theta), \quad \theta \in (-\pi/2, \pi/2)\ .$$

Then one may show the following for $\sqrt{s}$:

$$\sqrt{s} = (\sqrt{a\sec\theta})e^{i\theta/2} =: ik \implies s = -k^2$$

where k is a complex number. Following the above representation in θ it can be shown that k lies on yet another complex contour ∂D^- in the lower half complex plane defined by:

$$k_I^2 - k_R^2 = a, \text{ and } k_I < 0$$

where k_R, k_I are the real and imaginary parts of k respectively. Thus, we have now

$$\chi(t;\alpha,\gamma) = \frac{i}{\pi}\int_{\partial D^-} \frac{e^{-k^2 t}k}{-k^2 + ik\gamma + \alpha}\, dk\ .$$

Further, the above integral can be deformed to the real line using the Cauchy's integral theorem and an application of Jordan's lemma. It involves using the information that none of the poles of the complex integrand for $\alpha, \gamma > 0$ lie in the lower half of the complex $k-$

plane. Finally, we have:

$$\chi(t;\alpha,\gamma) = \frac{i}{\pi}\int_{-\infty}^{\infty} \frac{e^{-k^2 t}k}{-k^2 + ik\gamma + \alpha}\, dk,$$

which is the claim we made in eq. (3.23).

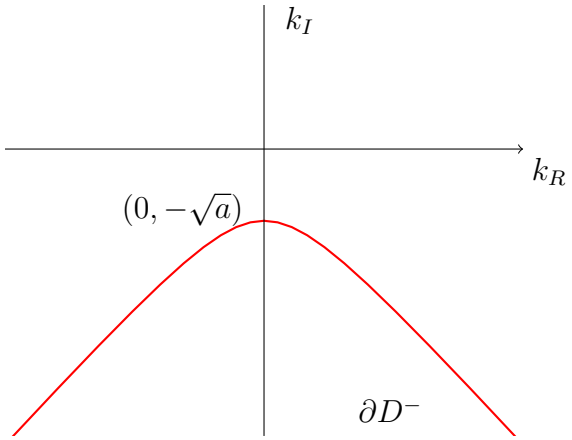

Figure 3.A.1: Contour ∂D^- (continuous red).

3.B Action of nonlinearity N_α on the numerical solution

We assumed the smooth mapping of the function $N_\alpha(w(t), t)$ to $\check{N}_\alpha(t)$. This does not hold when the first argument is w_{ni}, which is only an approximation to the true variable $w(t_{ni})$. We estimate the effect of this approximation on the nonlinear action. Recall that $w_{ni} = w(\tau_{ni}) + E_{ni}$ where E_{ni} is the stage error function. Therefore,

$$N_\alpha(w_{ni}, \tau_{ni}) = N_\alpha(w(\tau_{ni}) + E_{ni}, \tau_{ni})\ .$$

We Taylor-expand the nonlinear function around $(w(\tau_{ni}), \tau_{ni})$ which yields,

$$\begin{aligned} N_\alpha(w(\tau_{ni}) + E_{ni}, \tau_{ni}) &= N_\alpha(w(\tau_{ni}), \tau_{ni}) + E_{ni}\left.\frac{\partial N_\alpha}{\partial w}\right|_{w(\tau_{ni}),\tau_{ni}} + \mathcal{O}(E_{ni}^2), \\ &= \check{N}_\alpha(\tau_{ni}) + E_{ni}\left.\frac{\partial N_\alpha}{\partial w}\right|_{w(\tau_{ni}),\tau_{ni}} + \mathcal{O}(E_{ni}^2). \end{aligned}$$

The derivative $\partial N_\alpha/\partial w$ is yet another function of w, thus we define $G(w(t)) := \partial N_\alpha/\partial w$. Further, we assume a smooth function exists such that $G(w(t)) = \check{G}(t)$. This function inherits the behaviour of N_α with a similar series expansion as in (3.41). This allows us to

write the following, for some constant c,

$$\frac{\partial N_\alpha}{\partial w}\Big|_{w(\tau_{ni}),\tau_{ni}} = G(w(\tau_{ni})) = \check{G}(\tau_{ni}) = \check{G}(t_n) + c\sqrt{\Delta t} + ...$$

Thus we have the estimate claimed in (3.46) once we identify $\check{G} = J_n$

$$N_\alpha(w(\tau_{ni}) + E_{ni}, \tau_{ni}) = \check{N}_\alpha(\tau_{ni}) + \check{G}(t_n)E_{ni} + \mathcal{O}(E_{ni}\sqrt{\Delta t}) \ .$$

3.C Error estimate in the history function integral

We want to verify the following estimate for the 2-stage and 4-stage schemes:

$$\rho(k)\sum_{m=0}^{n}\left(\Delta t\sum_{i=1}^{\check{s}} d_i(k)J_m\delta_{mi}\right) \sim \mathcal{O}(\Delta t^{\frac{\check{s}}{2}}) \ . \tag{3.63}$$

Recall that $\{d_i\}$'s are fixed already at this point via the order conditions eqs. (3.36b) and (3.38b), so we cannot impose any further independent conditions on them. Instead, we assess the sum given the $\{d_i\}$'s. Recall also that $\delta_{n1} = 0$ for all n. We verify (3.63) separately for $\check{s} = 2$ and $\check{s} = 4$. We introduce a shorthand for the expressions

$$\sum_{i=1}^{j-1} a_{ji}c_i^{\frac{l-1}{2}} - c_j^{\frac{l+1}{2}}\phi_{(l-1)/2,j}(\bar{\gamma}) =: [OC]_{j,l}$$

which become order conditions when they are zero for some j, l.

(i) $\check{s} = 2$

$$\Delta t\sum_{i=1}^{\check{s}=2} d_i(k)\delta_{mi} = (\Delta t)d_2(k)\sum_{l=1}^{p_{2,2}=1} C_{l-1}(t_m)\Delta t^{\frac{l+1}{2}}[OC]_{2,l} + \mathcal{O}(\Delta t^{q(m)}) \ .$$

In the two-stage scheme, $[OC]_{2,1} = 0$ via (3.36c). The leading behaviour of the remainder however is time-dependent. We recall that the coefficients C_l for the odd index are zero for $t > 0$. This means that for $m = 0$, we have $q(0) = 5/2$ while for $m > 0$, we have $q(m) = 3$. As a result, for large enough n,

$$\sum_{m=0}^{n} J_m\Delta t\sum_{i=1}^{2} d_i(k)\delta_{mi} \sim \mathcal{O}(\Delta t^2)$$

which is a better estimate than required in the relation 3.63.

(ii) $\check{s} = 4$

$$\Delta t \sum_{i=1}^{\check{s}=4} d_i(k)\delta_{mi} \sim \Delta t \sum_{i=2}^{4} d_i(k) \sum_{l=1}^{p_{2,i}} C_{l-1}(t_m)(\Delta t)^{\frac{l+1}{2}} [OC]_{i,l} \tag{3.64}$$

Here, the leading contribution proportional to $C_1(t_m)(\Delta t)^{5/2}$ comes due to non-zero expressions $[OC]_{i,2}$. Once again, this contribution becomes zero for $m > 0$. Note that the other expressions $[OC]_{i,l}$ in (3.64) are zero due to the order conditions (3.38c) and (3.38e). Thus, we have the following which verifies (3.63) for $\check{s} = 4$,

$$\sum_{m=0}^{n} J_m \Delta t \sum_{i=1}^{4} d_i(k)\delta_{mi} \sim \mathcal{O}(\Delta t^2) \ .$$

3.D Standard versus non-standard RK schemes

Consider scalar initial value problems of the following general form:

$$\frac{dx}{dt} = f(x,t), \quad x(0) = x_0 \ ,$$

where $x(t)$ is the unknown dynamical variable we wish to solve for.

Toy problem 1: Consider $f(x,t) = -x + t$. The exact solution to this problem is:

$$x(t) = x_0 e^{-t} + (t-1) + e^{-t} \ .$$

We may check that the above solution has a well-defined Taylor-series expansion centered around any $t \geq 0$. We numerically solve this ODE using the standard RK schemes and assess the performance (see fig. 3.D.1). The standard schemes perform as expected with the promised convergence rates.

Toy problem 2: Consider now $f(x,t) = -x + \sqrt{t}$. The expression for the exact solution in the variation-of-parameters form is:

$$x(t) = e^{-t}x_0 + \int_0^t e^{-(t-\tau)}\sqrt{\tau}\, d\tau = e^{-t}x_0 + \sqrt{t} - \text{Dawson}(\sqrt{t}) \ . \tag{3.65}$$

The expansion of Dawson function around $t = 0$ goes as:

$$\text{Dawson}(y) \sim y - \frac{2}{3}y^3 + \frac{4}{15}y^5 + ...$$

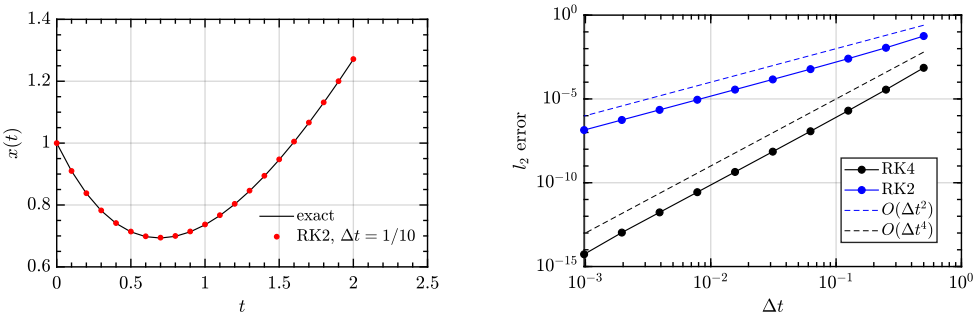

(a) (b)

Figure 3.D.1: Toy problem $dx/dt = -x + t$ solved using standard RK schemes. (a) Solution up to $T = 2$. (b) Consistent error convergence rates for RK2 and RK4.

From the above, we deduce the following leading order behavior of the solution around $t = 0$,

$$x(t) \sim x_0 - x_0 t + \frac{2}{3}t^{3/2} + \frac{1}{2}x_0 t^2 - \frac{4}{15}t^{5/2} + ...$$

Consequently, around $t = 0$, f then goes as:

$$f(x,t) = -x(t) + \sqrt{t} \sim -x_0 + \sqrt{t} + x_0 t - \frac{2}{3}t^{3/2} - \frac{1}{2}x_0 t^2 + \frac{4}{15}t^{5/2} + ...$$

The above expression evidently doesn't have well-defined derivatives at $t = 0$. Therefore it cannot be expressed in Taylor series around $t = 0$. However, for all other $t > 0$, the solution (eq. (3.65)) can be expanded about a point in Taylor series. We now put to test

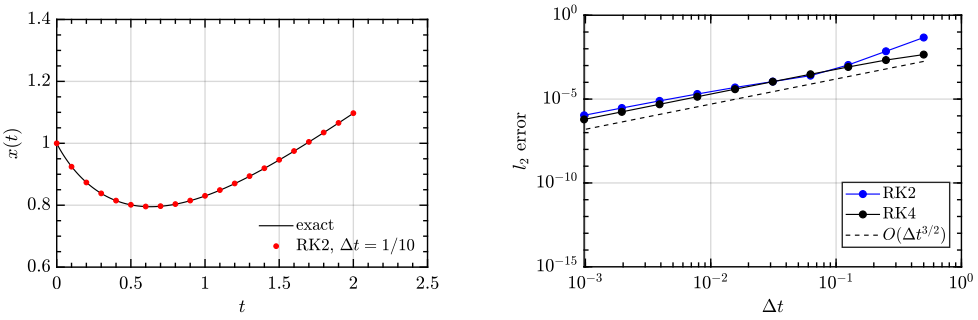

(a) (b)

Figure 3.D.2: Toy equation $dx/dt = -x + \sqrt{t}$ solved using the standard RK schemes. (a) Solution up to $T = 2$. (b) Error convergence at a reduced rate of $\Delta t^{3/2}$ instead of $(\Delta t)^2$ and $(\Delta t)^4$ expected of RK2 and RK4, respectively.

the standard RK algorithm to numerically solve toy problem 2. We observe in fig. 3.D.2 that the standard RK schemes suffer a reduced rate of error convergence. This is attributed

to the assumption made in these schemes of a well-defined Taylor-series expansion for the solution at all times including $t = 0$. However, the function f in toy problem 2 does not have a Taylor-series expansion at $t = 0$. The large error suffered in the construction of solution at the first time-step $t_1 = \Delta t$ lingers throughout the simulation despite the smaller error in the solutions at other times.

Chapter 4

Fate of inertial particles with memory effects in rotating vortical flows

This chapter is based on the article titled *Trapping and extreme clustering of finitely dense inertial particles near a rotating vortex pair* [Kapoor *et al.*, J. Fluid Mech.]. Saumav Kapoor is the first author. Our contributions are distinguished as follows: Saumav Kapoor conducted the study on the two vortex and particle model where the particle dynamics was evolved with the reduced MRG equation without the BBH force. I was responsible for the results which include the BBH force. Some figures which will form a part of Saumav Kapoor's thesis have been used here for comparison. All results which are without the BBH force are to be credited to Saumav Kapoor. Wherever it is unclear, Saumav's contribution has been highlighted in the respective figure caption.

4.1 Introduction

Turbulent flows with suspended inertial particles of varying relative densities are common in both natural and industrial systems, such as dust in protoplanetary disks and air-drying systems of powdered fertilizers and pesticides. In such scenarios, particles—typically denser than the surrounding fluid—can exhibit clustering, which is a precursor to inter-particle collisions. These collisions are critical for various natural phenomena including raindrop formation [9, 10], reproduction among small organisms [5] and planet formation [105, 106].

Understanding and predicting particle dispersion and transport in particle-laden turbulent flows is an outstanding problem of significance. The multiscale nature of turbulence makes it challenging to find a physical model universally valid across scales for probing such systems. Particle-resolved simulations may be performed, however, they require exceptionally high computational power and time, often providing little physical intuition.

Instead, we can make progress by studying inertial particle dynamics in simplified, model flows that mimic key structures of turbulent flows. This approach isolates relevant length and timescales, informing appropriate particle models that capture the dominant physics.

In this chapter, we investigate the dynamics of inertial particles, characterized by particle Stokes number St and density parameter R (for definitions, see 3.2), in a rotating system of vortices. We now motivate our interest in such vortical regions and their vicinity. Intense vortices, generated by vortex stretching, are the building blocks of turbulent flows [107]. Suspended inertial particles often sample these prevalent structures, influencing their clustering behavior. It is commonly understood that particles heavier than the suspending fluid centrifuge out of vortical flow regions and cluster in high-strain regions [61–64]. An explanation for this was provided by Haller & Sapsis in [108] for inertial particles with small particle Stokes number, $St \ll 1$. In the field description of particle velocity $\boldsymbol{V}_p(t) \rightarrow \boldsymbol{V}_p(\boldsymbol{x}, t)$, an approximation that is allowed when $St \ll 1$, its divergence at any spatial point $\boldsymbol{x}$ is given by,

$$\boldsymbol{\nabla} \cdot \boldsymbol{V}_p(\boldsymbol{x}, t) = -St\Big\{|\boldsymbol{S}(\boldsymbol{x}, t)|^2 - |\boldsymbol{R}(\boldsymbol{x}, t)|^2\Big\} \ . \tag{4.1}$$

Here, $\boldsymbol{S}$ and $\boldsymbol{R}$ are the strain-rate and rotation-rate tensors of the ambient incompressible flow field, $\boldsymbol{u}^\infty$, respectively, and $|.|$ is the Euclidean matrix norm. A positive divergence implies the evacuation of the neighborhood, while a negative divergence implies clustering. Haller & Sapsis [108] showed that the net divergence from any region encompassed by a closed streamline is positive. Using this argument, we may conclude that particles of $St \ll 1$ will evacuate the vicinity of an isolated vortex and constantly move away from it.

In the presence of background rotation, however, the criterion 4.1 is modified. Ravichandran, et al. in [109] showed that,

$$\underset{\sim}{\boldsymbol{\nabla}} \cdot \underset{\sim}{\boldsymbol{V}}_p(\underset{\sim}{\boldsymbol{x}}, t) = -St\Big\{|\underset{\sim}{\boldsymbol{S}}(\underset{\sim}{\boldsymbol{x}}, t)|^2 - |\underset{\sim}{\boldsymbol{R}}(\underset{\sim}{\boldsymbol{x}}, t)|^2 + 2\Omega^2\Big\} \equiv StQ_{\text{rot}} \ , \tag{4.2}$$

where Ω is the constant angular speed of the frame of reference, and the quantities with $\underset{\sim}{(.)}$ are written in the rotating frame. The above condition also defines the Okubo-Weiss parameter Q_{rot} in the rotating frame. Based on 4.2, even particles with small St can cluster into regions within closed streamlines, suggesting that the vicinity of vortices may host particle clusters. This highlights the role of systemic rotation in particle clustering, and motivates our investigation of particle clustering in rotating vortical systems.

For the rest of the chapter, we switch back to the Lagrangian description of the particle velocity, $\boldsymbol{V}_p(t)$.

We present a toy problem for particles in a simple two-dimensional vortical flow with systemic rotation: inertial particles near a co-rotating pair of Lamb-Oseen vortices, to study

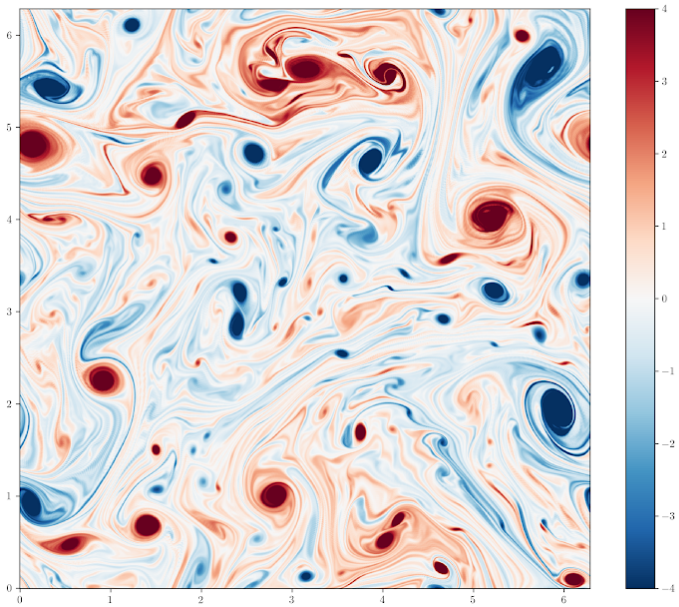

Figure 4.1.1: Snapshot of vorticity field (color indicating strength) from a forced two-dimensional turbulence simulation in a periodic box. Regions containing co-rotating pair of vortices form our domain of interest to study clustering and trapping of inertial particles. Image credit: Rajarshi.

particle trapping and clustering tendencies. Our choice of the Lamb-Oseen vortex is legitimate, as it mimics a typical vortex seen in two-dimensional turbulence [110, 111]. Figure 4.1.1 shows a snapshot from a typical two-dimensional turbulence simulation, showing prevalence of co-rotating vortex pairs, identified by pairs of identically colored patches of vorticity. The toy problem approach highlights general physical features of particle clustering and trapping, and is not to considered a predictive tool.

4.2 Our model and governing equations

Our background flow consists of a pair of co-rotating Lamb-Oseen vortices of identical strength Γ and core-width b, with their centres separated by a distance d_{sep} (see fig. 4.2.1(a)). In accordance to the Biot-Savart law, these vortices revolve around each other on a circle of diameter d_{sep}, with an angular speed $\Omega = \Gamma/\pi d_{\text{sep}}^2$, while maintaining a constant mutual angular separation of π. The corresponding time period of rotation is $T_c = 2\pi/\Omega$.

The width of the vortices is assumed sufficiently small compared to their separation, i.e., $b \ll d_{\text{sep}}$. The basis for this assumption is as follows: two identical vortices which are initially separated undergo merger in four stages [112]. In the first diffusive stage, they maintain their individual Gaussian structure and mutual separation while executing uniform motion on a

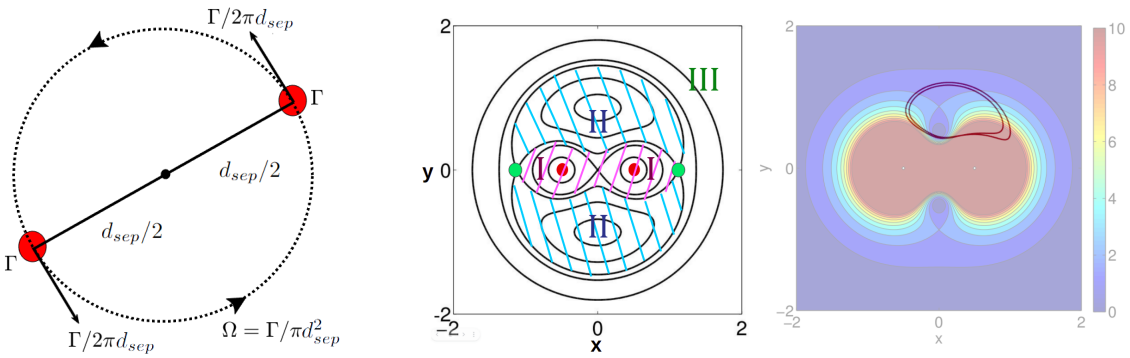

Figure 4.2.1: (a) Schematic showing two identical vortices (marked at their centers by red dots) executing circular motion at a constant rate. (b) Vortex locations and representative tracer-particle trajectories (closed orbits shown in black lines) are shown in the rotating frame of reference. Region II is the primary host for the attracting orbits of inertial particles. (c) Negative of the Okubo-Weiss parameter Q_{rot} overlaid by a representative limit cycle (attractor) of inertial particle trajectories. This schematic will also appear in the thesis of Saumav Kapoor.

circle. In two-dimensional flows, as the flow Reynolds number, $Re = \Gamma/\nu$, is made arbitrarily large, the first stage of merger can last for an arbitrarily long time. Once the vortices diffuse to a radius of about 0.3 times their separation, the second stage of merger begins, and the large-scale motion is no longer periodic. Therefore, to simplify our study, we assume a high enough flow Reynolds number such that the vortices execute circular motion with constant angular velocity during our simulation time.

The separation length d_{sep}, the time period of rotation $T_c = 2\pi/\Omega$, and their ratio $U_c = d_{\text{sep}}/T_c$ provide natural length, time, and velocity scales to nondimensionalize the system. In the nondimensional form, the ambient flow field is given by

$$\boldsymbol{u}^{\infty}(\boldsymbol{x},t) = \pi \boldsymbol{e}_z \times \left[(1 - e^{-|\boldsymbol{x}-\boldsymbol{X}|^2/b^2}) \frac{\boldsymbol{x}-\boldsymbol{X}}{|\boldsymbol{x}-\boldsymbol{X}|^2} + (1 - e^{-|\boldsymbol{x}+\boldsymbol{X}|^2/b^2}) \frac{\boldsymbol{x}+\boldsymbol{X}}{|\boldsymbol{x}+\boldsymbol{X}|^2} \right], \tag{4.3}$$

where the instantaneous vortex centres are at $\pm\boldsymbol{X}$ with $\boldsymbol{X} = (\cos(2\pi t)/2,\ \sin(2\pi t)/2)$, and $\boldsymbol{e}_z$ is the unit vector perpendicular to the plane of the vortices. The nondimensional vortex width is set to $b = 0.1$ throughout our analysis, without loss of generality.

We are interested in the dynamics of inertial particles in the above unsteady background flow in the absence of gravity. A majority of studies [109, 113–115] on inertial particles have focused on either heavy point-like particles ($\rho_p/\rho_f \to \infty$) or particles with very small inertia (finite ρ_p/ρ_f, $St << 1$). These cases afford simplified MRG models, given by eqs. (3.3) and (3.4), neglecting the nontrivial Basset-Boussinesq history (BBH) force to describe their

dynamics. However, for finite ρ_p/ρ_f and finite-time relaxation of fluid, the effects of the BBH force could become significant, and are expected to be pronounced for near-neutrally buoyant particles ($\rho_p \sim \rho_f$). Thus, we model the particle dynamics using the Maxey-Riley-Gatignol (MRG) equation, incorporating the BBH force. To isolate the history force's effects, we also compare results with the *reduced* MRG equation, which neglects this term.

Consistent with the conditions under which the MRG equation is derived (section 1.1.4), we assume negligible particle Reynolds number, i.e, $Re_p = a_p|\boldsymbol{V}_p'(t) - \boldsymbol{u}'^{\infty}(\boldsymbol{X}_p', t)|/\nu \ll 1$, based on particle's slip velocity and radius a_p, and $a_p/d_{\text{sep}} \ll 1$ to ignore Faxén corrections. We recall that $[\boldsymbol{X}'_p(t),\ \boldsymbol{V}'_p(t)]^T$ represents the instantaneous state of the particle. We also assume negligible shear Reynolds number, neglecting any lift dynamics. Further, we assume that the particles are in dilute suspension, allowing us to neglect their mutual interaction as well as their effect on the flow (one-way coupling). The dynamics of the *non-interacting* inertial particles in the ambient flow of co-rotating Lamb-Oseen vortex pair, under the above assumptions, is governed by the MRG equation. For completeness, we reproduce the nondimensional MRG eq. (3.1) from chapter 3 here with the parameters,

$$\frac{d\boldsymbol{X}_p(t)}{dt} = \boldsymbol{V}_p(t), \tag{4.4a}$$

$$\frac{d\boldsymbol{V}_p(t)}{dt} + \frac{1}{St}\boldsymbol{w}(t) + \sqrt{\frac{3R}{St}}\Big(\frac{\boldsymbol{w}_0}{\sqrt{\pi t}} + \int_0^t \frac{d\boldsymbol{w}(\tau)/d\tau}{\sqrt{\pi(t-\tau)}}\,d\tau\Big) = R\frac{D}{Dt}\boldsymbol{u}^{\infty}(\boldsymbol{X}_p(t), t)\ , \tag{4.4b}$$

where we recall that $\boldsymbol{w}(t) = \boldsymbol{V}_p(t) - \boldsymbol{u}^{\infty}(\boldsymbol{X}_p(t), t)$ is the particle slip velocity, the nondimensional parameters R, S are as defined in eq. (3.2), and $\boldsymbol{u}^{\infty}$ is the ambient flow from eq. (4.3).

Figure 4.2.2 shows snapshots of a particle ensemble evolved according to the MRG equation with the BBH force near the rotating vortex pair in the laboratory frame.

The dynamics are more insightful in the frame of reference rotating with the nondimensional angular velocity of the vortex pair. The background flow field in the rotating frame transforms according to $\boldsymbol{u}^{\infty}(\boldsymbol{x}) - 2\pi\boldsymbol{e}_z \times \boldsymbol{x} \to \boldsymbol{u}^{\infty}(\boldsymbol{x})$. In this co-rotating frame, the background flow is steady, and the stationary vortices are centred at $(\pm 1/2, 0)$. The representative streamlines of the stationary flow are shown in fig. 4.2.1(b), which also defines the horizontal and vertical coordinates.

We can identify three distinct regions based on the behavior of tracer particles in fig. 4.2.1(b). Region I is the close vicinity of the vortices; tracer particles seeded in this region execute closed trajectories around the closest vortex. In region II, which is of primary interest to us, the tracer particles move on closed orbits passing through their initial positions, and are, on average, equally influenced by the two vortices. Region III is the far-field, where tracers

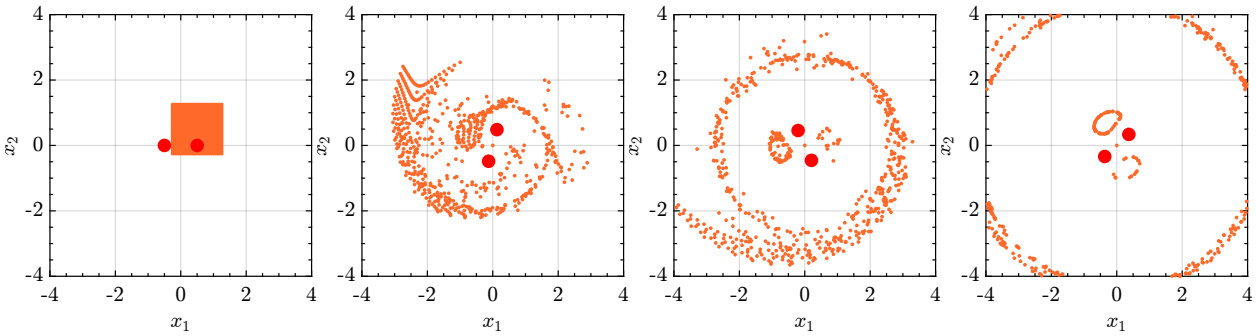

Figure 4.2.2: Evolution of particle ensemble (orange dots) using the MRG equation near a rotating vortex pair (marked by big red filled circles), for $St = 0.4$, $R = 0.5\,(\rho_p/\rho_f = 2.5)$, at four progressive time instances shown in the laboratory frame. Some particles have attracted to a limit cycle (right-most panel), which co-rotates with the vortex pair. Majority have centrifuged out.

execute closed orbits encircling both vortices, as they increasingly perceive the system as a single vortex of twice the strength.

In fig. 4.2.1(c), we show the modified Okubo-Weiss parameter, Ω_{rot}, which is most negative in the red region. According to the condition 4.1, heavy particles with $St \to 0$ are more likely to cluster in this red region. Overlaid is a typical limit cycle for finitely-dense inertial particles with finite St, showing that they can cluster outside the region predicted by 4.1. Comparing the location of the closed streamlines in fig. 4.2.1(b) with the limit cycle in fig. 4.2.1(c) reveals that inertial particles can cluster within closed streamlines enclosing a elliptic fixed point in the rotating frame.

4.2.1 Simulation details and numerical methods

We perform numerical simulations of inertial particles for a range of particle Stokes number and density ratios. Without the BBH force, the MRG equation simplifies to a nonlinear ODE, which we solve using a standard fourth-order Runge-Kutta scheme to obtain particle trajectories. The time-step is chosen between $\Delta t = 10^{-3}$ and 10^{-4}. However, when the BBH force is retained, the MRG equation is a nonlinearly forced integro-differential equation, posing numerical challenges discussed in section 3.1.2. We therefore use the explicit time-integrator developed for the MRG equation in chapter 3. We solve eq. (4.4) using the second-order RK-χTD scheme given in section 3.3.2 (with $10^{-4} < \Delta t < 10^{-3}$) in the laboratory frame, and then transform the variables to their counterparts in the rotating frame.

To detect an attractor (fixed points and limit cycles), we initially place $\mathcal{O}(10^3)$ particles on a uniform grid in the region $[-1.5, 1.5] \times [0, 1.5]$ in position space (see fig. 4.2.2(a)). The

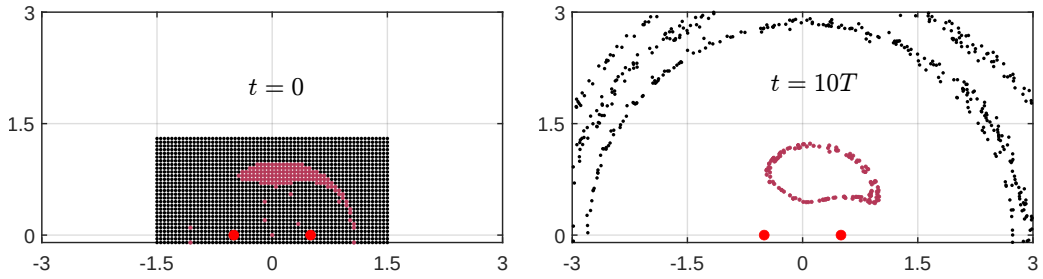

Figure 4.2.3: Typical evolution of an ensemble of inertial particles ($\rho_p/\rho_f > 1$) in the position space, in the rotating frame of an identical vortex pair. The particles are uniformly seeded near the vortex pair as shown in (a). Particles after 10 time periods of rotation, evolved under reduced MRG equation, are shown in (b). A fraction of particles (colored maroon) get trapped to an attractor such as a fixed point or a limit cycle. However, a majority of particles (colored black) are centrifuged out in spiraling orbits. The former set of particles forms our primary focus. This figure forms a part of Saumav Kapoor's thesis and is shown here for clarity.

initial particle velocity in the rotating frame is set to zero, and the trajectories are evolved over a sufficiently long time until convergence onto an attractor. The properties of the attractor are calculated using the last 5% of each trajectory. Fixed points are identified when the particle's velocity in the rotating frame goes to zero. To detect limit cycles, we note that at its extremities in the horizontal x-direction, we must have the x component of the particle velocity $V_{px} = 0$ in the rotating frame. We count the number of distinct x locations at which $V_{px} = 0$ and divide by two to get the period of the limit cycle. When every such location is distinct, we have a chaotic attractor. Without the BBH force, a few tens of nondimensional time are typically sufficient for particles to converge to an attractor, whereas with the inclusion of the BBH force the system takes longer to converge. However, we note that within a few nondimensional times the attractors are clearly delineated, even for the cases including the BBH force (see fig. 4.2.3(b)), but we run simulations for longer times for near-perfect convergence.

Simulating large ensembles of particles to obtain attractors would have been computationally prohibitive with brute-force methods to compute the BBH force. However, using RKχTD from chapter 3, simulating a single particle for $\mathcal{O}(10^6)$ time iterations typically took under a third of a minute, making it feasible to simulate large particle ensembles of size $\mathcal{O}(10^3)$.

Figure 4.2.3 shows a typical evolution of an ensemble of particles in the position space in the rotating frame. In fig. 4.2.3(a), we have a uniformly seeded particle ensemble with $R = 0.84, St = 0.22$, each particle colored either in maroon or black. Figure 4.2.3(b) shows

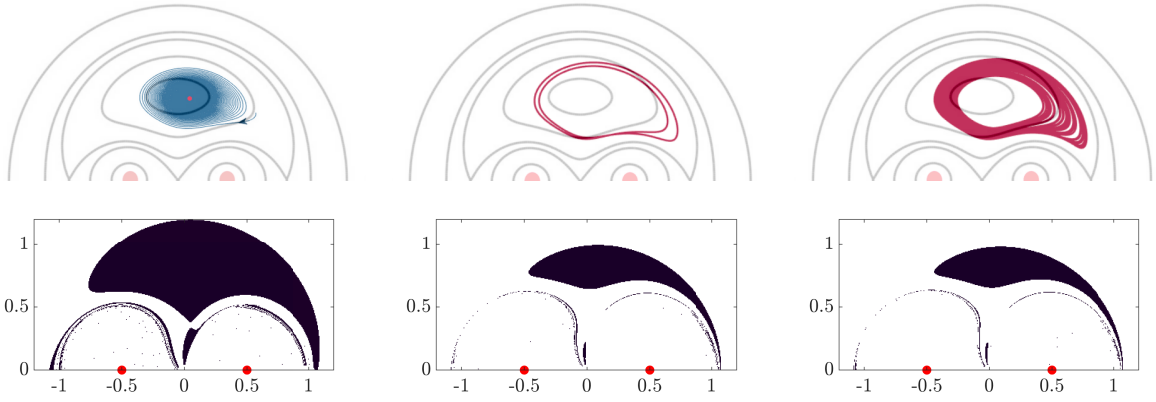

(a) $St = 0.09$ (b) $St = 0.22$ (c) $St = 0.24$

Figure 4.3.1: Typical asymptotic states shown in maroon (top) and their corresponding basins of attraction (bottom) for a finitely dense inertial particle with density factor $R = 0.84\,(\rho_p/\rho_f \approx 1.3)$ and varying particle Stokes number St, without the BBH force. Red dots indicate the vortex centres in the rotating frame. In (a) the particle spirals (shown in blue) into a fixed point attractor, whereas in (b) and (c) the particle is trapped into a limit cycle of period 2 and a strange attractor respectively. The orbits are overlaid on the separatrices of the background flow for clarity of their scale and location. Mirror-symmetric patterns exist in the lower half-plane. This figure forms a part of Saumav Kapoor's thesis and is shown here for clarity.

their respective positions after 10 time periods of rotation: the maroon patch of particles has converged to an attractor (a limit cycle here) whereas the black patch of particles has centrifuged out spirally. Since we are interested in clustering and trapping behavior of particles, the centrifuging particles are excluded from our study and the results therein.

4.3 Particle trapping dynamics and Results

We focus on region II in fig. 4.2.1(b), where attracting orbits of various descriptions, including fixed points and limit cycles, are contained, potentially trapping particles for long times. We study the parameter space defined by $0 < St < 1$ and $0 < R < 1$, corresponding to inertial particles that are finitely denser than the ambient fluid. To highlight the fundamental differences, we briefly review the idealized case of heavy particles ($\rho_p/\rho_f \to \infty$) for comparison. Particles of a fixed St and R are initially placed in a dense uniform grid across a region of interest, and their asymptotic behavior is categorized.

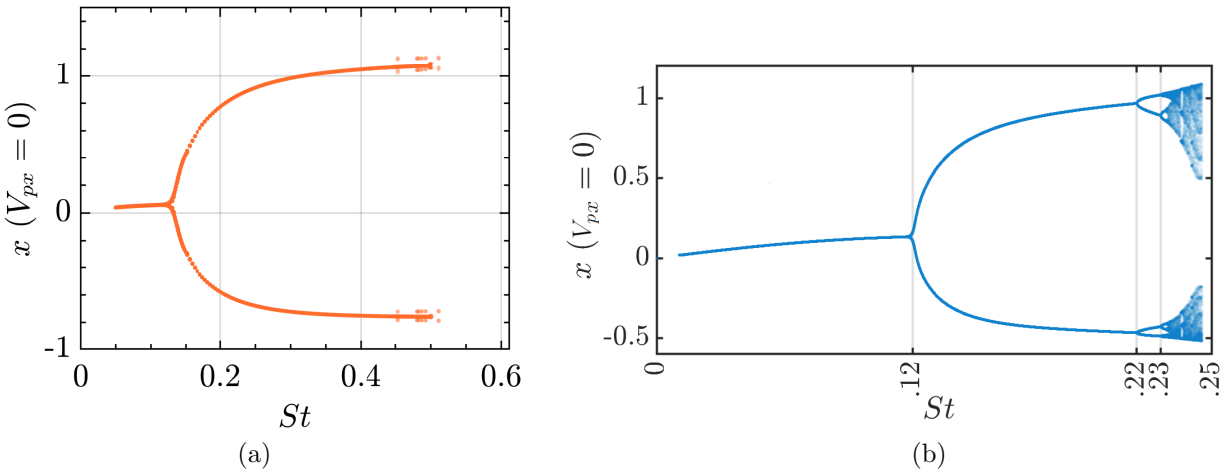

Figure 4.3.2: Bifurcation diagrams for $R = 0.84$ ($\rho_p/\rho_f \approx 1.3$) shown (a) with and (b) without the BBH force. The $y-$axis plots the horizontal extremities of the attractor where $V_{px} = 0$. Trapping prevails for wider range of St, with the BBH force. In both cases, an attracting fixed point exists below $St \sim 0.12$. With the BBH force, a period-1 limit cycle exists for $0.12 \lesssim St \lesssim 0.5$, with particles escaping beyond $St_{\text{crit}} \approx 0.5$. Without the BBH force, a period-1 limit cycle prevails for $0.12 \lesssim St \lesssim 0.22$, followed by period-2 and more complex limit cycles. Beyond a lower critical $St_{crit} \sim 0.25$, all particles escape. This figure will be part of Saumav Kapoor's thesis as well.

4.3.1 Low particle-to-fluid density ratio ($1 < \rho_p/\rho_f < 2$)

We examine the trapping behavior of particles with a large density parameter R, corresponding to small particle-to-fluid density ratio, using the prototypical case of $R = 0.84$ ($\rho_p/\rho_f \approx 1.3$), both with and without the BBH force. The top panels in fig. 4.3.1 show typical attractors for particles of increasing particle Stokes numbers evolved without the BBH force in the rotating frame: a fixed point, a period-2 limit cycle and a chaotic (strange) attractor. The fixed point in fig. 4.3.1(a) represents a point undergoing periodic motion along a circle in the laboratory frame. Similarly, the limit cycle observed in the rotating frame fills an annular region in the laboratory frame. All particles starting within the corresponding basins of attraction (BoA) shown in the lower panels of fig. 4.3.1 asymptotically reach their respective attractors and never leave the vicinity.

Figure 4.3.2 shows bifurcation diagrams for $R = 0.84$ with and without the BBH force, identifying attractors for different St, if present. The y-axis records a relevant feature of the attractor for each St–specifically, the horizontal extremities where the particle's horizontal velocity vanishes. Alternatively, the local maxima of the time series for the particle's horizontal position on the attractor can be used to generate these diagrams.

Particles with large inertia exit the vicinity of the vortex pair–indicated by the absolute

truncation of the bifurcation diagrams at higher St. This truncation occurs at the critical particle Stokes number, St_{crit}, beyond which no particles remain trapped. Notably, the $St_{crit} \approx 0.25$ for the case without the BBH force, and is significantly greater at $St_{crit} \approx 0.5$ when the BBH force is included. For small to moderate St, particles can either get trapped indefinitely in the vicinity of the vortex pair or spend varying amounts of time in the vicinity before escaping. Figure 4.3.2(b) shows that for particles evolved without the BBH force, a fixed attracting point exists below $St \approx 0.12$. Beyond this threshold, limit cycles of varying complexities emerge, leading to a period-doubling route to escape as St increases. In contrast, the influence of the BBH force in fig. 4.3.2(a) is self-evident. Interestingly, the bifurcation from a fixed point to a limit cycle occurs at a similar particle Stokes number with and without the BBH force. However, the period-1 limit cycle persists under the effect of the BBH force up to $St_{crit} \approx 0.5$, where the period-doubling route is left incomplete. The wider range of St for which particles remain trapped with the BBH force highlights its importance in modeling particle dynamics.

The area of the basin of attraction (BoA) is a measure of the fraction of particles which get trapped onto an attractor. It is calculated as the area bounding the initial locations of the particles that get trapped on the attractor. Figure 4.3.3 compares the size of BoA measured for a range of Stokes numbers at $R = 0.84$ ($\rho_p/\rho_f \approx 1.3$), with and without the BBH force. Both with and without the BBH force, particles with larger inertia, characterized by higher St, have greater propensity to leave the vicinity, marked by the shrinking size of BoAs in fig. 4.3.3. Notably, besides missing the significant trapping of particles of larger inertia, the fraction of particles trapped is grossly underestimated at all particle Stokes numbers by neglecting the BBH force.

We conclude our discussion on the particle trapping dynamics for the prototypical case corresponding to $R = 0.84$.

4.3.2 Moderate particle-to-fluid density ratio ($2 < \rho_p/\rho_f < 10$)

We now move on to higher particle densities, i.e., smaller R. Figure 4.3.4 shows the bifurcation diagrams corresponding to $R = 0.2$ ($\rho_p/\rho_f = 7$) and $R = 0.5$ ($\rho_p/\rho_f = 2.5$). Changing the density ratio introduces unexpected features in the dynamics. In fig. 4.3.4(d), corresponding to $R = 0.5$ ($\rho_p/\rho_f = 2.5$), we see period-doubling bifurcation followed by unusual period-halving bifurcations back to a fixed point at higher particle Stokes number. For the same density ratio, the inclusion of the BBH force affects the dynamics to exhibit a period-doubling bifurcation route to chaos, as shown in fig. 4.3.4(b). Interestingly, even at this density ratio, the BBH force does not significantly change the particle Stokes number at which the first bifurcation occurs: going from fixed point to limit cycle. At the larger density

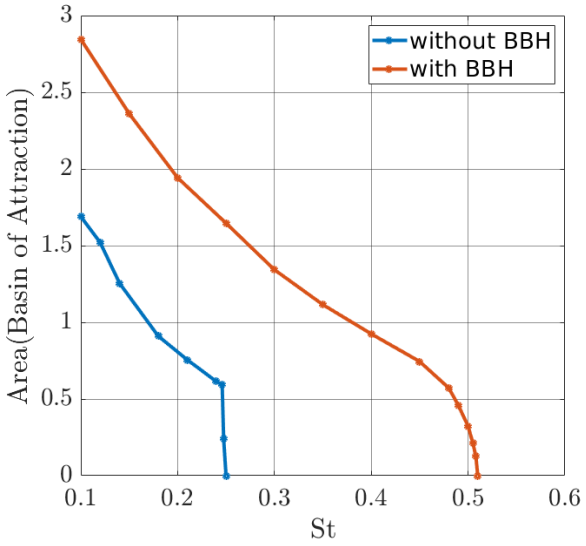

Figure 4.3.3: Variation of the area of the basin of attraction with the Stokes number for $R = 0.84$ ($\rho_p/\rho_f \approx 1.3$), with and without the BBH force. This figure will be a part of Saumav Kapoor's thesis as well.

ratio of ~ 7 (fig. 4.3.4(c)), particles are trapped only for two small, distinct ranges of St. In contrast, with the inclusion of the BBH force, fig. 4.3.4(a) shows a widespread trapping across a broad range of St, with a period-halving bifurcation, recovering a fixed point as the sole attractor at large $St < St_{\text{crit}}$.

Another non-standard feature observed in the bifurcation diagrams for inertial particles in this moderate range of density parameters is the existence of intermittent gaps i.e., particle Stokes numbers for which no particles are trapped in the vicinity of the vortices. Figure 4.3.4(a) shows two such windows, a wide window around $St \sim 0.2$ and a narrower one around $St \approx 0.55$. This non-monotonic trend of trapping behavior with increasing St, going back and forth between attractors of different complexities, is remarkably non-intuitive and warrants further investigation.

These examples illustrate a general trend about inertial particles in our system: the long-time behavior of inertial particles with the BBH force at a given density parameter R is in broad qualitative agreement with the behavior without BBH at a higher R. In other words, a denser particle with the BBH force behaves qualitatively like a lighter particle without the BBH force over time.

4.3.3 Heavy limit ($\rho_p/\rho_f \to \infty$)

The idealized case of the infinitely dense particles in co-rotating vortices was studied by Angilella (2010) in [4] upon neglecting the BBH force. The author analytically showed

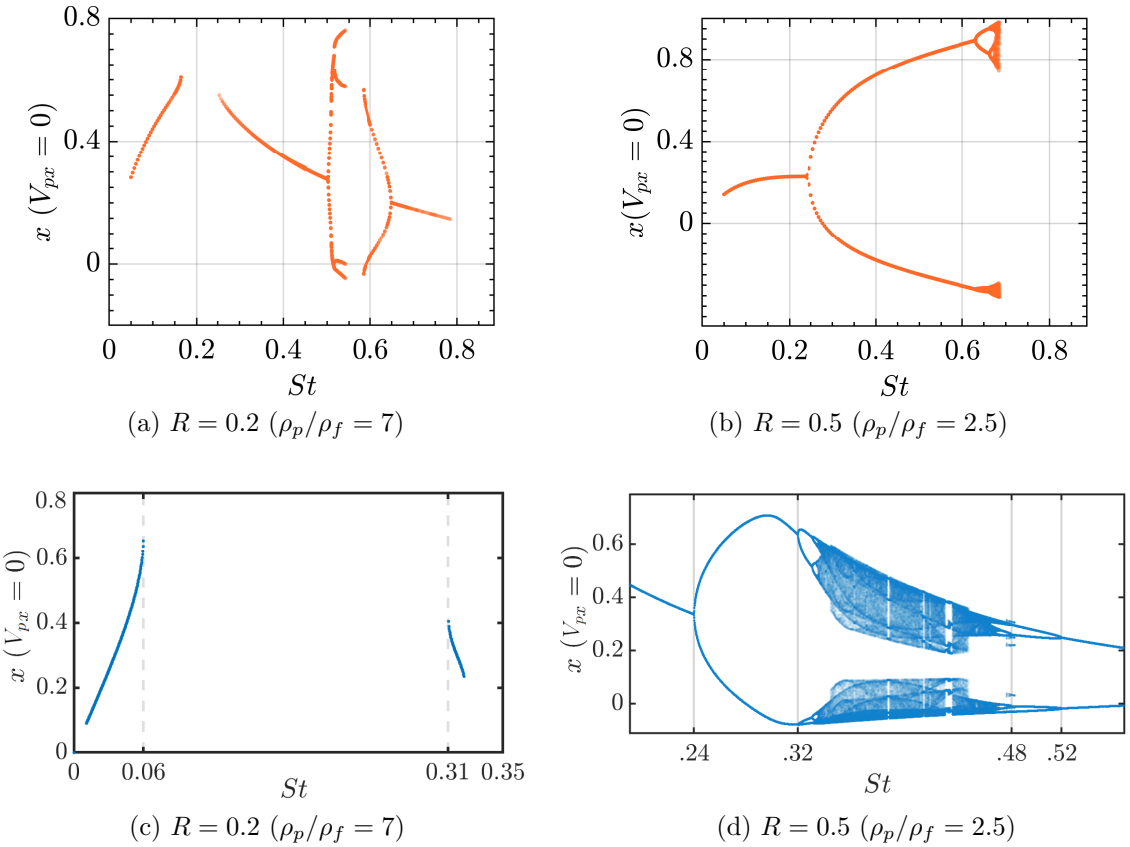

(a) $R = 0.2$ $(\rho_p/\rho_f = 7)$ (b) $R = 0.5$ $(\rho_p/\rho_f = 2.5)$

(c) $R = 0.2$ $(\rho_p/\rho_f = 7)$ (d) $R = 0.5$ $(\rho_p/\rho_f = 2.5)$

Figure 4.3.4: Bifurcation diagrams for inertial particles with higher density-ratios, shown with the BBH force in the top panels and without in the bottom panels. This figure will be a part of Saumav Kapoor's thesis too.

the existence of a fixed point up to $St_{cr} = (2 - \sqrt{3})/2\pi$ and no attractor beyond. We repeated the calculations with the BBH force included for $\rho_p \gg \rho_f$, and found the critical particle Stokes number unchanged. Supporting this, in fig. 4.3.5, we show the bifurcation diagram obtained by numerically integrating the particle trajectories with the BBH force for $R = 10^{-4}$. For a finite St, this limit is practically equivalent to the case in [4], where the BBH force is neglected. Our results show good agreement with the analytical expressions for the attractor location and the critical Stokes number given therein.

We note a qualitative difference in the influence of the BBH force between idealized infinitely dense particles and physical finitely dense particles, such as $R = 0.2$ $(\rho_p/\rho_f = 7)$ (fig. 4.3.4(a). The BBH force significantly affects finitely dense particles, particularly when their densities are comparable to that of the ambient fluid. This underscores the importance of including the BBH force as a significant factor in studies of solid-liquid systems, such as microplastics in the ocean.

Summarizing the complexity of particle dynamics discussed thus far for exemplar pa-

rameters, we provide a phase plot in fig. 4.3.6, which characterizes the trapping behavior across density ratios and particle Stokes number without the BBH force. Figure 4.3.6(a)

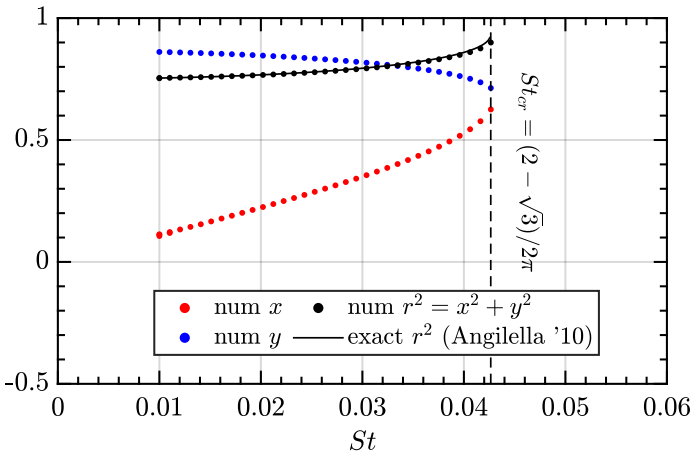

Figure 4.3.5: Critical particle Stokes number St and the location of fixed-point attractor for $R = 10^{-4}$ with the BBH force. Analytical results of Angilella (2010) in [4] are shown by (i) solid black line for the analytical expression for location of the attracting point, r, and (ii) dashed black line for the analytical critical Stokes number beyond which no stable attracting point exists. Our numerical results (dots) at small R recover both.

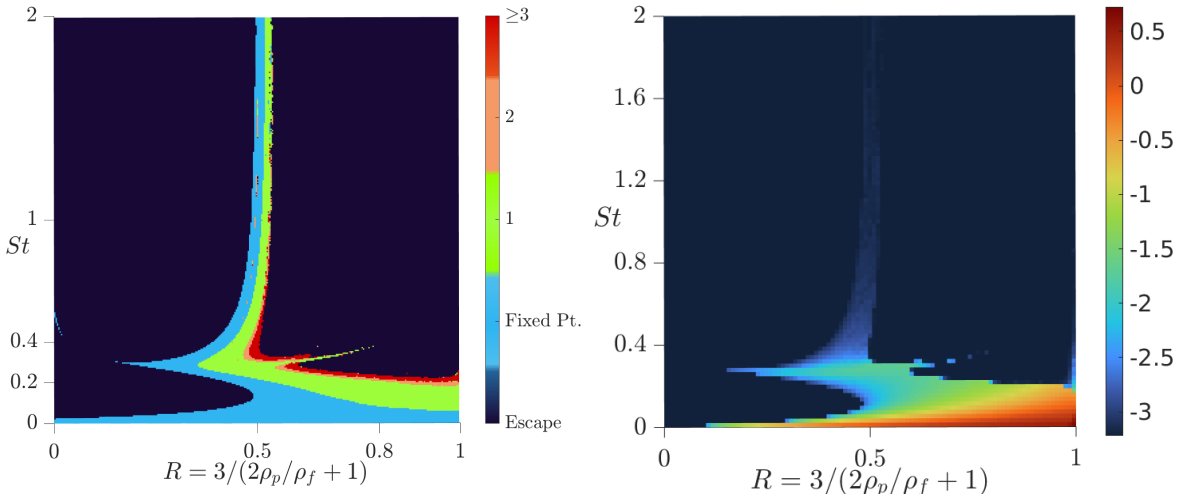

Figure 4.3.6: Phase plots for inertial particles evolved without the BBH force based on (a) the period of the attracting orbit, and (b) the logarithm of the size of the basin of attraction. The regime occupied by limit cycles of period 2 and above is very narrow. Particles of near-neutral densities tend to stay longer in the vicinity of the vortex pair. The computations for this figure were performed by Saumav Kapoor and this figure forms a part of his thesis. It is shown here to help some of the present discussion.

shows the different kinds of attracting orbits obtained from reduced MRG model for inertial particles. We may identify the following three broad regimes: for $1 > R \gtrsim 0.5$ we have a period-doubling route to chaos, for $0.5 > R > 0.35$ a period-doubling route, which may go all the way to chaos or may be limited to a few bifurcations, is followed by period halving, leading to a single fixed point, and for $0.35 > R$ we have only attracting fixed point in the regime where we have trapped particles. Even with the BBH force, the three regimes prevail, but the transitions happen at lower values of R. The density ratio of $R \sim 0.5$ is most interesting, distinguished by the existence of attracting orbits at large particle Stokes number, with sensitive dependence on R. Chaotic attractors only exist at $R \gtrsim 0.5$, i.e., when the particle and fluid densities are comparable. The corresponding areas of the BoA are shown as a phase plot in fig. 4.3.6(b). Broadly, at low particle Stokes numbers, as the particles become denser, the BoA shrinks. However, at intermediate Stokes numbers and density ratios, we see non-monotonic behavior.

4.4 Conclusions and Discussion

In this chapter, we investigated the dynamics of inertial particles that are denser than the fluid in the simplest rotating vortical system: of two identical co-rotating vortices in a periodic circular motion, using both the MRG and the reduced MRG models. Primarily, we demonstrated using our toy problem that the conventional wisdom of clustering in high-strain regions, away from vortical regions, is challenged in rotating systems of vortices. Broadly, we find that particles of finite density have a higher propensity to be trapped indefinitely in the system compared to the idealized infinitely dense particles, where the history effects due to the BBH force is negligible. This warrants caution in using *heavy point-particle* models for practical scenarios.

We summarize our findings from the toy problem. For brevity, particles evolved with memory effects of the BBH force are referred to as *Particles-E*, and those without as *Particles-G*, with E and G standing for elephant and goldfish[1], respectively.

1. Our study reveals rich dynamical states for such particles depending on (R, St): they can get confined into regions of complex structures, ranging from simple fixed points to limit cycles of varying periodicity, including possibly chaotic attractors, shown by the phase plot in fig. 4.3.6.

2. Particles-E are more susceptible to clustering and trapping near the vortex pair over a wider range of densities and sizes than particles-G. The larger critical Stokes number

[1] going by the adages based on myths: "memory like a goldfish" and "elephants never forget".

for particles-E, a parameter beyond which no trapping is seen, is suggestive of this.

3. A larger fraction of particles-E than particles-G in the vicinity of the vortex pair participate in extreme and permanent clustering on the attractors. The larger size of the basins of attraction of particles-E is suggestive of this (see fig. 4.3.3).

4. Particles-E take longer to converge to the attractor, if one exists, due to the slow late-time relaxation enforced by the BBH force. These long transients indicate that the non-interacting particles-E spend longer time around each other, in the vicinity of the vortex pair.

We now discuss the limitations of our model. We recall that the MRG equation is a model equation derived in the small particle Reynolds number limit, $Re_p \to 0$. In practical scenarios where Re_p is only finitely small, the effects due to flow inertia will become significant in long but finite time. Therefore, the validity of the MRG equation in various regards including the form of the history force and quasi-steady drag force are questionable after long simulation-time. However, our results are valid and insightful in the cases where significant clustering is observed within short-times, subject to the condition $Re_p < 1$.

The MRG equation is widely used at Stokes numbers of $\mathcal{O}(1)$ but the need to satisfy this requirement simultaneously with $Re_p \ll 1$, as well as keeping the particle size small, i.e., $a_p/d_{\text{sep}} \ll 1$ imposes additional restrictions. By expressing Re_p in terms of our control parameters R and St, we obtain the scaling relation $Re_p(a_p/d_{\text{sep}}) \sim RSt|\boldsymbol{w}|$, where we recall that $\boldsymbol{w}$ is the nondimensional particle slip velocity. For a small particle under the influence of a single vortex, the vortex turnover time may be used to define St. In our model, the St is defined using the system's period of rotation. In both cases, when $St \sim \mathcal{O}(1)$ we usually have $|\boldsymbol{w}| \sim \mathcal{O}(1)$. In principle, the above scaling requirement can be satisfied if $R \to 0$, but in practice we typically have non-zero R, however small. Demanding arbitrary smallness of the particle size (a_p/d_{sep}) is therefore penalized by large Re_p near vortices. For finite density ratios, as in our case, satisfying the requirements is even harder. From our computations of slip velocity, we find that the slip velocities with the BBH force are usually significantly lower than without it. At the highest Stokes numbers in our study, $Re_p \sim \mathcal{O}(10)$ for $a_p/d_{\text{sep}} \sim \mathcal{O}(10^{-2})$ for some part of the dynamics. However, close to the fixed points, and often near the limit cycles, slip velocities are low and so is Re_p. The small Re_p assumption is realized for very dense and near-neutrally buoyant particles. Due to this, and the findings in [116] that show applicability of the MRG equation for $Re_p \lesssim 17$, we expect that our findings have qualitative significance. We note that estimates of Re_p are rarely discussed in the literature, and need more attention.

Chapter 5

Particle-interaction model in two-dimensional unsteady Stokes flow

5.1 Introduction

In the previous chapters, we used the Maxey-Riley-Gatignol (MRG) equation to model the motion of an isolated sphere (chapters 2 and 3) and a collection of non-interacting particles (chapter 4) in flows. However, particle interactions may become significant, say, when two particles approach each other just before a collision-event. The long-term goal of the work presented in this chapter is to derive an analogue of the MRG equation that accounts for inter-particle interactions mediated by an unsteady Stokes flow.

Ardekani and Rangel (2006) [117] studied the unsteady motion of two spheres embedded within a Stokesian flow, derived equations of motion using approximation techniques (such as repeated reflections and the point-force method) and computed the unsteady hydrodynamic force acting on the particles. However, the kernels associated with the history forces in their equations can be challenging (and possibly even intractable) to compute due to the presence of poles in the complex plane whose location must be determined for the pertinent set of system parameters.

The reciprocal theorem [24], used in the derivation of the original MRG equation, has also been used to study the hydrodynamic interactions between solid surfaces mediated by Stokesian flow for simplified geometries, for example, a sphere near a wall. The success of the reciprocal theorem lies in the use of a particular auxiliary solution, which is typically only known for the simplest of geometries. Thus, the application of the reciprocal theorem in more complex geometries with multiple boundaries is less fruitful where the auxiliary function is not available readily.

In this chapter, we consider a simplified interaction problem involving two stationary

disks embedded in a two-dimensional fluid with finite-time relaxation. This translates into the problem of solving the unsteady Stokes equation in a multiply connected domain. Our immediate goal is to derive an approximate integral equation for the unsteady hydrodynamic force on the disks as the initial nonzero flow relaxes under the unsteady Stokes dynamics. This simplified problem establishes an approach and framework to derive the MRG analogue with inter-particle interactions. Once the hydrodynamic forces on the stationary disks have been computed, the subsequent steps in the program would involve allowing the disks to move and then ultimately repeating the calculations for spherical particles in a three-dimensional fluid. As we shall see, the two-dimensional stationary disk scenario already requires the introduction of new ideas.

5.2 Problem statement

Consider an incompressible Newtonian fluid in a two-dimensional, multiply connected domain $\mathcal{V}$ embedded in $\mathbb{R}^2$ (see fig. 5.2.1). The domain is exterior to two rigid stationary disks of radius a_p whose centers are given by the position vectors $\boldsymbol{r}^{(1)}$ and $\boldsymbol{r}^{(2)}$ and we denote their mutual separation by $l = |\boldsymbol{r}^{(1)} - \boldsymbol{r}^{(2)}|$. The boundaries of the disks are denoted by $\partial\mathcal{V}^{(1)}$ and $\partial\mathcal{V}^{(2)}$, where the index in the superscript identifies the disk. We denote the union of the two disk boundaries by $\partial\mathcal{V} := \partial\mathcal{V}^{(1)} \cup \partial\mathcal{V}^{(2)}$. The far-field boundary at infinity is denoted by $\partial\mathcal{V}^{\infty}$ where we assume the fluid velocity $\boldsymbol{v}$ and pressure p vanishes.

We consider a nonzero initial state of the flow $(\boldsymbol{v}_0(\boldsymbol{x}), p_0(\boldsymbol{x}))$ supported in $\mathcal{V}$. The flow is left to relax according to the unsteady Stokes equation while satisfying the no-slip boundary condition simultaneously on both disks (equivalently on $\partial\mathcal{V}$). The nondimensional PDE system describing the scenario is given below,

$$\frac{\partial \boldsymbol{v}}{\partial t} = \boldsymbol{\nabla}\cdot\boldsymbol{\sigma}\ , \quad \boldsymbol{\nabla}\cdot\boldsymbol{v} = 0\ , \quad \boldsymbol{x}\in\mathcal{V} \tag{5.1}$$

subject to the following initial and boundary conditions,

$$\boldsymbol{v}(\boldsymbol{x},0) = \boldsymbol{v}_0(\boldsymbol{x}), \quad \boldsymbol{x}\in\mathcal{V}\ , \tag{5.2a}$$

$$\boldsymbol{v}(\boldsymbol{x},t) = \boldsymbol{0}\ , \qquad \boldsymbol{x}\in\partial\mathcal{V}\ , \quad t>0\ , \tag{5.2b}$$

$$\boldsymbol{v}(\boldsymbol{x},t) = \boldsymbol{0}\ , \qquad \boldsymbol{x}\in\partial\mathcal{V}^{\infty}\ , \ t>0\ , \tag{5.2c}$$

where $\boldsymbol{\sigma}(\boldsymbol{v},p) = [\boldsymbol{\nabla}\boldsymbol{v} + (\boldsymbol{\nabla}\boldsymbol{v})^T] - p\mathbb{I}$ denotes the stress tensor for a Newtonian fluid and $\mathbb{I}$ is a 2×2 identity matrix. We impose a compatibility condition on the initial flow field: $\boldsymbol{v}_0(\boldsymbol{x}) = \boldsymbol{0}$ when $\boldsymbol{x}\in\partial\mathcal{V}$, in order to satisfy eq. (5.2b) at $t = 0$. Similarly, we also assume

incompressibility of initial flow field $\boldsymbol{\nabla} \cdot \boldsymbol{v}_0 = 0$.

The variables in eq. (5.1) are scaled by $L_c = a_p,\ T_c = a_p^2/\nu$ and an independent velocity scale, U_c, characteristic to the initial flow field $\boldsymbol{v}_0$. The stress tensor and pressure are scaled by $\mu U_c/a_p$. Consequently, all the coefficients in the nondimensional form of the governing eq. (5.1) and the constitutive relation for the stress tensor are unity. Also, the disks have unit radius and the inter-particle separation between the disks is given by the nondimensional parameter $\epsilon^{-1} = l/a_p$.

The principal quantity of interest is the time-dependent hydrodynamic force on each disk that develops as the surrounding fluid relaxes under the unsteady Stokes dynamics,

$$\boldsymbol{f}_H^{(m)}(t) := \oint_{\boldsymbol{x} \in \partial \mathcal{V}^{(m)}} \boldsymbol{\sigma}(\boldsymbol{v}(\boldsymbol{x},t), p(\boldsymbol{x},t)) \cdot \boldsymbol{n}(\boldsymbol{x})\, dS = \oint_{\boldsymbol{x} \in \partial \mathcal{V}^{(m)}} \boldsymbol{T}(\boldsymbol{x},t)\, dS\ , \tag{5.3}$$

where we have introduced the vector-valued traction, given by,

$$\boldsymbol{T}(\boldsymbol{x},t) := \boldsymbol{\sigma}(\boldsymbol{v}(\boldsymbol{x},t), p(\boldsymbol{x},t)) \cdot \boldsymbol{n}(\boldsymbol{x})\ .$$

The superscript m in eq. (5.3) refers to the disk, *i.e.* $m = 1, 2$, and $\boldsymbol{n}$ is the unit vector normal to the disk's surface, directed into the fluid domain.

Remark 5.1. We motivate our interest in the unsteady hydrodynamic force by anticipating how it will feature in the construction of the MRG analogue down the line (which will be actively pursued in future work). Suppose the disks are allowed to move in response to the flow dynamics, and assume no other external force acts on the system. Then the equation of motion for the disk will be given by Newton's equation as follows,

$$\frac{d\boldsymbol{V}_p^{(m)}(t)}{dt} = \boldsymbol{f}_H^{(m)}(t)\ ,$$

where $\boldsymbol{V}_p^{(m)}(t)$ is the $m-$th disk's instantaneous velocity vector related to its position vector (now time-dependent) by $\boldsymbol{V}_p^{(m)} = d\boldsymbol{r}^{(m)}(t)/dt$. The coefficients here are set to unity for exposition only. By constructing the appropriate hydrodynamic force that, in addition to modeling finite-time relaxation of the fluid, also incorporates inter-particle interactions, the analogous MRG equation with inter-particle interactions may be subsequently derived. This chapter describes the computation of such a hydrodynamic force.

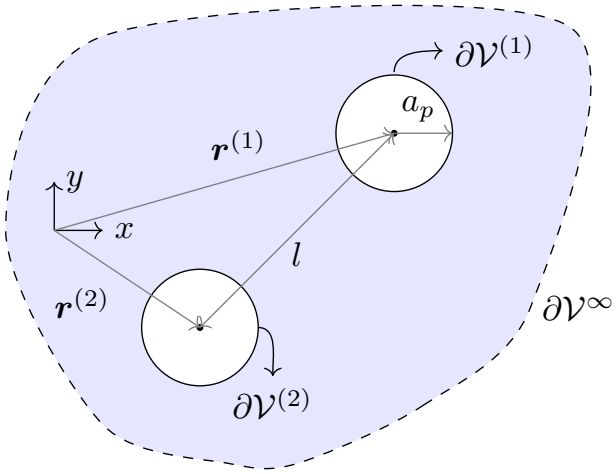

Figure 5.2.1: Schematic of the domain and coordinate system. The region occupied by the fluid, $\mathcal{V}$, is marked in blue. Two identical stationary disks are placed at a mutual separation of $l = |\boldsymbol{r}^{(1)} - \boldsymbol{r}^{(2)}|$. The boundaries of $\mathcal{V}$ are shown: $\partial\mathcal{V}^{(m)}$ on the disks, for $m = 1, 2$, and $\partial\mathcal{V}^{\infty}$ denotes the boundary at far-field.

5.3 Derivation

We use ideas from the Unified Transform method (UTM), also known as the Fokas method, to derive various expressions [118]. We introduce the Fourier transform pair of a function supported in $\mathcal{V}$ as follows:

$$\hat{(.)}(\boldsymbol{k}, t) := \int_{\boldsymbol{x}\in\mathcal{V}} e^{-i\boldsymbol{k}\cdot\boldsymbol{x}}(.)(\boldsymbol{x}, t) dV(\boldsymbol{x}) \ , \ (.)(\boldsymbol{x}, t) = \frac{1}{(2\pi)^2} \int_{\mathbb{R}^2} e^{i\boldsymbol{k}\cdot\boldsymbol{x}} \hat{(.)}(\boldsymbol{k}, t) \, d\boldsymbol{k} \ ,$$

where $\boldsymbol{k}$ is an arbitrary real vector in the two-dimensional Fourier space. Note, to define the inverse transform, we have extended the function originally supported only in $\mathcal{V}$ to the whole of $\mathbb{R}^2$ by setting the function to zero in the disk-regions. We denote the magnitude of $\boldsymbol{k}$ by $k = |\boldsymbol{k}|$.

Note the incompressibility condition for the velocity field in the multiply connected domain $\mathcal{V}$ is given by

$$0 = \int_{\mathcal{V}} e^{-i\boldsymbol{k}\cdot\boldsymbol{x}} \nabla \cdot \boldsymbol{v}(\boldsymbol{x}, t) \, dV = \oint_{\partial\mathcal{V}} e^{-i\boldsymbol{k}\cdot\boldsymbol{x}} \boldsymbol{v}(\boldsymbol{x}, \boldsymbol{t}) \cdot \boldsymbol{n'}(\boldsymbol{x}) \, dS + i\boldsymbol{k} \cdot \hat{\boldsymbol{v}}(\boldsymbol{k}, t) \ . \tag{5.4}$$

Since we assume the disks are stationary, the integral term vanishes resulting in a simple condition for incompressibility in Fourier space: $\boldsymbol{k} \cdot \hat{\boldsymbol{v}} = 0$.

5.3.1 The global relation

Let us define,

$$\varphi(\boldsymbol{x}, t, \boldsymbol{k}) = -i\boldsymbol{k}\cdot\boldsymbol{x} + \omega(k)t\,.$$

For brevity, we use φ dropping the arguments when the dependence is unambiguous. We now introduce the following functions:

$$\boldsymbol{A}(\boldsymbol{x}, t, \boldsymbol{k}) = e^{\varphi}\boldsymbol{v}, \quad \mathbb{B}(\boldsymbol{x}, t, \boldsymbol{k}) = e^{\varphi}\Big\{\boldsymbol{\sigma} + i\boldsymbol{k} \otimes \boldsymbol{v}\Big\}, \quad C(\boldsymbol{x}, t, \boldsymbol{k}) = ie^{\varphi}(\boldsymbol{k}\cdot\boldsymbol{v})\,, \tag{5.5}$$

where $\boldsymbol{A}$, $\mathbb{B}$, and C are vector, tensor, and scalar functions respectively. The symbol $\otimes$ indicates tensor product (of 2D vectors). Using these functions, we can write the governing equation in eq. (5.1) in divergence form to the extent possible, leaving a few extra terms as follows,

$$\frac{\partial \boldsymbol{A}}{\partial t} = \boldsymbol{\nabla}\cdot\mathbb{B} + \boldsymbol{\nabla}C - i(e^{\varphi}\boldsymbol{k})p - \boldsymbol{k}(\boldsymbol{k}\cdot\boldsymbol{v})e^{\varphi}\,, \tag{5.6}$$

if we assume the following relationship between ω and k (also referred to as the *dispersion relation* in the UTM literature)

$$\omega(k) = k^2\,.$$

Henceforth in all the subsequent expressions, we always set $\omega = k^2$.

We integrate eq. (5.6) over the fluid domain $\mathcal{V}$ and over time $[0, t]$ to obtain the following:

$$\int_0^t \int_{\boldsymbol{x}\in\mathcal{V}} \Bigg(-\frac{\partial \boldsymbol{A}(\boldsymbol{x},\tau,\boldsymbol{k})}{\partial\tau} + \boldsymbol{\nabla}\cdot\mathbb{B}(\boldsymbol{x},\tau,\boldsymbol{k}) + \boldsymbol{\nabla}C(\boldsymbol{x},\tau,\boldsymbol{k}) \\ - i(e^{\varphi(\boldsymbol{x},\tau,\boldsymbol{k})}\boldsymbol{k})p(\boldsymbol{x},\tau,\boldsymbol{k}) - \boldsymbol{k}(\boldsymbol{k}\cdot\boldsymbol{v}(\boldsymbol{x},\tau))e^{\varphi(\boldsymbol{x},\tau,\boldsymbol{k})}\Bigg)\, dV\, d\tau = 0. \tag{5.7}$$

One can show the last term vanishes on account of incompressibility condition on $\boldsymbol{v}$ in the Fourier space. Subsequently, using divergence theorem, the above equation gives the following relation in the Fourier space,

$$-\int_{\boldsymbol{x}\in\mathcal{V}} \Big\{\boldsymbol{A}(\boldsymbol{x},t,\boldsymbol{k}) - \boldsymbol{A}(\boldsymbol{x},0,\boldsymbol{k})\Big\}\, dV + \int_0^t \oint_{\boldsymbol{x}\in\partial\mathcal{V}} \mathbb{B}(\boldsymbol{x},\tau,\boldsymbol{k})\cdot\boldsymbol{n}'(\boldsymbol{x})\, dS\, d\tau \\ + \int_0^t \oint_{\boldsymbol{x}\in\partial\mathcal{V}} C(\boldsymbol{x},\tau,\boldsymbol{k})\boldsymbol{n}'(\boldsymbol{x})\, dS\, d\tau - i\int_0^t \int_{\boldsymbol{x}\in\mathcal{V}} e^{\varphi(\boldsymbol{x},\tau,\boldsymbol{k})}\boldsymbol{k}\; p(\boldsymbol{x},\tau)\, dV\, d\tau = 0\,, \tag{5.8}$$

where $n'(\boldsymbol{x})$ is the unit normal vector at $\boldsymbol{x}$ on the disk's surface pointing outwards from the fluid domain $\mathcal{V}$, and therefore relates to the unit normal vector on the disk as $\boldsymbol{n}' = -\boldsymbol{n}$.

Finally, by expressing the functions $\boldsymbol{A}$, $\mathbb{B}$ and C back in terms of the primary dynamical

variables $\boldsymbol{v}$ and $\boldsymbol{\sigma}$, and using the definition of the Fourier transform, we derive the following relation in the Fourier space,

$$e^{k^2 t}\hat{\boldsymbol{v}}(\boldsymbol{k},t) + i\boldsymbol{k}\int_0^t e^{k^2\tau}\hat{p}(\boldsymbol{k},\tau)\,d\tau = \hat{\boldsymbol{v}}_0(\boldsymbol{k}) + \int_0^t e^{k^2\tau}\oint_{\boldsymbol{x}\in\partial\mathcal{V}} e^{-i\boldsymbol{k}\cdot\boldsymbol{x}}\Big\{\boldsymbol{\sigma}(\boldsymbol{v}(\boldsymbol{x},\tau),\ p(\boldsymbol{x},\tau))\cdot\boldsymbol{n}'(\boldsymbol{x}) + \boldsymbol{\phi}(\boldsymbol{x},\tau,\boldsymbol{k})\Big\}\,dS\,d\tau\ , \tag{5.9}$$

where the vector function $\boldsymbol{\phi}(\boldsymbol{x},t,\boldsymbol{k}) := i\Big\{\Big(\boldsymbol{v}\cdot\boldsymbol{n}'(\boldsymbol{x})\Big)\boldsymbol{k} + \Big(\boldsymbol{v}\cdot\boldsymbol{k}\Big)\boldsymbol{n}'(\boldsymbol{x})\Big\}$.

We note that $\boldsymbol{\phi} = \boldsymbol{0}$ on the surface of stationary disks due to eq. (5.2b). Therefore, the equation further reduces to:

$$e^{k^2 t}\hat{\boldsymbol{v}}(\boldsymbol{k},t) + i\boldsymbol{k}\int_0^t e^{k^2\tau}\hat{p}(\boldsymbol{k},\tau)\,d\tau = \hat{\boldsymbol{v}}_0(\boldsymbol{k}) + \int_0^t e^{k^2\tau}\oint_{\boldsymbol{x}\in\partial\mathcal{V}} e^{-i\boldsymbol{k}\cdot\boldsymbol{x}}\boldsymbol{\sigma}(\boldsymbol{v}(\boldsymbol{x},\tau),\ p(\boldsymbol{x},\tau))\cdot\boldsymbol{n}'(\boldsymbol{x})\,dS\,d\tau\ , \quad \boldsymbol{k}\in\mathbb{R}^2\ . \tag{5.10}$$

We refer to eq. (5.10) as the (vector) *global relation*[1] for the PDE system in eq. (5.1). It contains all relevant boundary conditions and initial condition that the solution, here its Fourier transform ($\hat{\boldsymbol{v}}$, $\hat{p}$), depends on. This is the master equation from which desired quantities of interest can be constructed by performing suitable operations. Indeed, the global relation can be interpreted as an integral relation equivalent to the original PDE description in eq. (5.1).

Note that we have already used the Dirichlet condition, prescribed by the no-slip condition, in deriving the global relation. Further, if traction ($\boldsymbol{T} = \boldsymbol{\sigma}\cdot\boldsymbol{n}$) on the surface is prescribed, then the expressions for the solution function can be readily derived using the inverse Fourier transform. However, when the no-slip boundary condition is enforced, the traction on the disk must be determined from the solution to the PDE. In other words, the traction is an unknown here. More importantly, the final term in eq. (5.10) resembles our quantity of interest, the hydrodynamic force, except for the lingering exponential function. However, progress has been made in identifying such a term in the global relation.

Our objective now is to derive an independent integral equation for the evolution of the traction. A surface integral of the traction over a specific disk will then yield an integral equation for the corresponding unsteady hydrodynamic force, the quantity of our interest. For that, we proceed to find expressions for the flow field.

[1]The phrase global relation comes from the UTM literature [118–120].

5.3.2 Expressions for the flow field

We now derive the expressions for the velocity and the pressure fields as a function of traction using the global relation. By taking the dot product of the global relation eq. (5.10) with the vector $\boldsymbol{k}$, and applying the divergence-free condition to $\boldsymbol{v}_0$ and $\boldsymbol{v}$ in the bulk for $t > 0$, we eliminate the explicit dependence on the current unknown velocity field $\hat{\boldsymbol{v}}(\boldsymbol{k}, t)$. Thus, we derive an expression for the integral of (the Fourier transform of the) pressure:

$$i\boldsymbol{k} \int_0^t de^{k^2\tau} \hat{p}(\boldsymbol{k}, \tau)\, d\tau = \int_0^t e^{k^2\tau} \oint_{\boldsymbol{x}\in\partial\mathcal{V}} e^{-i\boldsymbol{k}\cdot\boldsymbol{x}} \frac{(\boldsymbol{k}\otimes\boldsymbol{k})}{k^2} \cdot \Big\{ \boldsymbol{\sigma}(\boldsymbol{v}(\boldsymbol{x},\tau),\ p(\boldsymbol{x},\tau)) \cdot \boldsymbol{n}'(\boldsymbol{x}) \Big\}\, dS(\boldsymbol{x})\, d\tau \ . \tag{5.11}$$

Substituting eq. (5.11) in eq. (5.10), we get the following expression for the fluid velocity field:

$$\begin{aligned} \hat{\boldsymbol{v}}(\boldsymbol{k}, t) =& e^{-k^2 t} \hat{\boldsymbol{v}}_0(\boldsymbol{k}) \\ &+ \left(\mathbb{I} - \frac{(\boldsymbol{k}\otimes\boldsymbol{k})}{k^2} \right) \cdot \int_0^t d\tau\, e^{-k^2(t-\tau)} \oint_{\boldsymbol{x}\in\partial\mathcal{V}} e^{-i\boldsymbol{k}\cdot\boldsymbol{x}} \boldsymbol{\sigma}(\boldsymbol{v}(\boldsymbol{x},\tau),\ p(\boldsymbol{x},\tau)) \cdot \boldsymbol{n}'(\boldsymbol{x})\ \ dS(\boldsymbol{x})\ \ d\tau \ . \end{aligned} \tag{5.12}$$

We have eliminated explicit pressure dependence from the expression for velocity; an implicit dependence via the traction term remains. But, in line with our goal, we have derived an expression for the Fourier transform of velocity field in terms of the traction field.

Next, we proceed to derive an expression for the pressure field. We differentiate eq. (5.11) with respect to the time variable, to obtain the following:

$$\hat{p}(\boldsymbol{k}, t) = -i \oint_{\boldsymbol{x}\in\partial\mathcal{V}} e^{-i\boldsymbol{k}\cdot\boldsymbol{x}} \frac{\boldsymbol{k}\cdot\boldsymbol{\sigma}(\boldsymbol{v}(\boldsymbol{x},t),\ p(\boldsymbol{x},t))\cdot\boldsymbol{n}'(\boldsymbol{x})}{k^2}\, dS(\boldsymbol{x}) \ . \tag{5.13}$$

Thus, we have obtained the expressions for both the Fourier transform of the flow fields, namely eq. (5.12) and eq. (5.13). A few remarks are in order at the moment:

1. *Fluid velocity in real space:* We perform an inverse Fourier transform of eq. (5.12) at an arbitrary point $\boldsymbol{x} \in \mathcal{V}$ to obtain

$$\boldsymbol{v}(\boldsymbol{x}, t) = \int_{\boldsymbol{y}\in\mathcal{V}} \mathbb{G}_0(\boldsymbol{x}, t, \boldsymbol{y}, 0) \cdot \boldsymbol{v}_0(\boldsymbol{y})\, dV(\boldsymbol{y}) + \int_0^t \oint_{\boldsymbol{y}\in\partial\mathcal{V}} \mathbb{G}(\boldsymbol{x}, t, \boldsymbol{y}, \tau) \cdot \boldsymbol{T}(\boldsymbol{y}, \tau)\, dS(\boldsymbol{y})\, d\tau \ , \tag{5.14}$$

where $\mathbb{G}_0$ and $\mathbb{G}$ are Green's function associated with the unsteady Stokes flow, for zero Dirichlet condition and no bulk forcing, with divergence-free constraint. Their

expressions are given by:

$$\mathbb{G}_0(\boldsymbol{x},t,\boldsymbol{y},\tau) := \frac{1}{(2\pi)^2}\int_{\mathbb{R}^2} e^{i\boldsymbol{k}\cdot(\boldsymbol{x}-\boldsymbol{y})-k^2(t-\tau)}\mathbb{I}\,d\boldsymbol{k}\ ,$$
$$\mathbb{G}(\boldsymbol{x},t,\boldsymbol{y},\tau) := -\frac{1}{(2\pi)^2}\int_{\mathbb{R}^2}\Big(\mathbb{I}-\frac{(\boldsymbol{k}\otimes\boldsymbol{k})}{k^2}\Big)e^{i\boldsymbol{k}\cdot(\boldsymbol{x}-\boldsymbol{y})-k^2(t-\tau)}\,d\boldsymbol{k}\ .$$

The above solution expression in eq. (5.14) is written in the form that appears in the classical potential theory: the two terms on the right-hand side are the *initial potential* and the *single layer potential*, respectively [121].

2. *Divergence-free fluid velocity field:* The Fourier-space projection operator featuring in eq. (5.12), $\Big(\mathbb{I}-\frac{(\boldsymbol{k}\otimes\boldsymbol{k})}{k^2}\Big)$, enforces the divergence-free condition for the flow velocity field at all times $t>0$.

3. *Pressure develops instantaneously in incompressible flows.* The hydrodynamic pressure responds instantaneously to the surface traction (see eq. (5.13)), whereas the velocity field depends nonlocally on the surface traction (see eq. (5.12)), with the presence of the time-integral. This, however, is not the case if the velocity field is compressible.

5.3.3 Expression for the hydrodynamic force on a disk

Using the expressions for the flow field, we now construct the traction term. To construct the corresponding traction term in Fourier space, we consider the following combination of terms written in index notation for convenience: $(k_j\hat{v}_i + k_i\hat{v}_j + i\hat{p}\delta_{ij})$, where δ_{ij} is the Kronecker delta. The inverse Fourier transform of this expression relates to the traction and, in turn, the hydrodynamic force in the following way,

$$\begin{aligned}&\int_{\mathbb{R}^2} e^{i\boldsymbol{k}\cdot\boldsymbol{x}}\Big(k_j\hat{v}_i + k_i\hat{v}_j + i\hat{p}\delta_{ij}\Big)n'_j(\boldsymbol{x})\,d\boldsymbol{k} = -i(2\pi)^2\sigma_{ij}(\boldsymbol{x},t)n'_j(\boldsymbol{x}) = i(2\pi)^2T_i(\boldsymbol{x},t)\ ,\\ \implies &\oint_{\boldsymbol{x}\in\partial\mathcal{V}^{(m)}}\left\{\int_{\mathbb{R}^2} e^{i\boldsymbol{k}\cdot\boldsymbol{x}}\Big(k_j\hat{v}_i + k_i\hat{v}_j + i\hat{p}\delta_{ij}\Big)n'_j(\boldsymbol{x})\,d\boldsymbol{k}\right\}dS(\boldsymbol{x}) = i(2\pi)^2(\boldsymbol{f}_H^{(m)})_i(t)\ ,\end{aligned} \tag{5.15}$$

where we have used eq. (5.3) to relate traction to hydrodynamic force and the relation $\boldsymbol{n}' = -\boldsymbol{n}$.

The above relation guides the series of operations to be performed to derive an expression for the hydrodynamic force on the $m-$th disk: an inverse Fourier transform followed by a surface integral over the chosen disk. We perform this sequence of operations on the left-hand side of the expression in eq. (5.15) after substituting the expressions for $\hat{\boldsymbol{v}}$ and $\hat{p}$ from eqs. (5.12) and (5.13). Computations involve multiple integrals over the disks' surfaces, the

spectral $\boldsymbol{k}$ space, and possibly a time integral (a typical computation for one such term is shown in section 5.A). We recall the small parameter, $\epsilon = a_p/l$, which compares the disk's size with the inter-disk separation and appears in the following equations. Choosing $m = 1$, without loss of generality, the series of integral computations on eq. (5.15) yields the following final integral relation for the hydrodynamic force on the first disk:

$$\begin{aligned}\left(\frac{\pi}{2}-1\right)\boldsymbol{f}_H^{(1)}(t) + \pi\int_0^t K(t-\tau;1)\boldsymbol{f}_H^{(1)}(\tau)\,d\tau = \boldsymbol{g}(\boldsymbol{v}_0(\boldsymbol{r}^{(1)})) - \frac{\pi}{2}\boldsymbol{h}^{(1)}(t) \\ + \pi\int_0^t G(t-\tau;1)\boldsymbol{h}^{(1)}(\tau)\,d\tau - \pi\epsilon^2\boldsymbol{M}(\theta,\boldsymbol{r}^{(1)})\cdot\boldsymbol{f}_H^{(2)}(t) \\ - \pi\int_0^t K(t-\tau;\epsilon^{-1})\boldsymbol{f}_H^{(2)}(\tau)\,d\tau \\ + \boldsymbol{M}(\theta,\boldsymbol{r}^{(1)})\cdot\int_0^t G(t-\tau;\epsilon^{-1})\boldsymbol{f}_H^{(2)}(\tau)\,d\tau\ .\end{aligned} \tag{5.16}$$

Note that a symmetric equation for $\boldsymbol{f}_H^{(2)}$ for the second disk can be similarly derived.

The function $\boldsymbol{g}$ is the driving function, which abstracts the dependencies on the initial flow field at the disk's location. The function $\boldsymbol{h}$ is defined as,

$$\boldsymbol{h}^{(m)}(t) = \int_0^{2\pi}\boldsymbol{M}(\theta,\boldsymbol{r}^{(m)})\cdot\boldsymbol{T}(\theta,t)\,d\theta\ ,$$

which represents variation of the traction over the disk's surface. The matrix $\boldsymbol{M}$ and the memory kernels are defined in the subsequent section, where we derive the minimal model.

5.4 The minimal model: integral equations

To derive a minimal model that captures the memory effects at the leading order, we assume (i) large separation compared to disk size, $l/a_p = \epsilon^{-1} \gg 1$, and (ii) very small variation of the traction over the disk's circumference, which allows us to ignore the functions $\boldsymbol{h}^{(m)}$ from eq. (5.16). As a result, we are able to derive a closed set of integral equations for the unknown unsteady hydrodynamic forces on the two disks, driven by a known driving term, here $\boldsymbol{g}$. The resultant model for the hydrodynamic forces is nonlocal and is given by the following compactly-written set of integral equations, at the leading order in ϵ:

$$\begin{pmatrix}\mathcal{L}-\mathbb{I} & \mathcal{I}^{(1)}\\ \mathcal{I}^{(2)} & \mathcal{L}-\mathbb{I}\end{pmatrix}\begin{pmatrix}\boldsymbol{f}_H^{(1)}(t)\\ \boldsymbol{f}_H^{(2)}(t)\end{pmatrix} = \begin{pmatrix}\boldsymbol{g}(\boldsymbol{v}_0(\boldsymbol{r}^{(1)}))\\ \boldsymbol{g}(\boldsymbol{v}_0(\boldsymbol{r}^{(2)}))\end{pmatrix}\ , \tag{5.17}$$

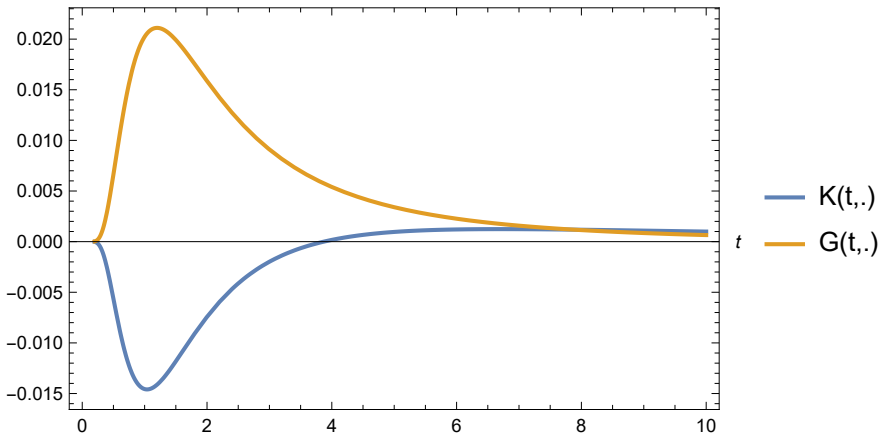

Figure 5.4.1: Behaviour of the kernels in the integral operators, $K(t,\cdot)$ and $G(t,\cdot)$, as a function of time t for the parameter, $c = 4$ which is representative of disk-separation of $l/a_p \sim 4$

where the vector-valued function $\boldsymbol{g}$ contains dependence on the initial flow field, $\boldsymbol{v}_0$, which drives the dynamics in our problem. $\mathbb{I}$ is the 2×2 identity matrix, and $\mathcal{L}$, $\mathcal{I}$ are integral operators, denoting self-interaction and inter-particle interaction, respectively. They are defined by their action on an arbitrary vector $\boldsymbol{z}$, using index notation:

$$\mathcal{L}[z_i](t) = \frac{\pi}{2} z_i(t) + \pi \int_0^t K(t-\tau;1) z_i(\tau)\, d\tau \ ,$$
$$\mathcal{I}^{(m)}[z_i](t) = \pi \int_0^t \left\{ K(t-\tau;\epsilon^{-1})\delta_{ij} - M_{ij}(\theta, \boldsymbol{r}^{(m)}) G(t-\tau;\epsilon^{-1}) \right\} z_j(\tau)\, d\tau \ , \quad i,j \in \{1,2\} \ ,$$

where $\boldsymbol{M}(\theta, \boldsymbol{r}^{(m)})$ is the standard 2×2 reflection matrix along the directed line joining the centers of the interacting disks, which originates from $\boldsymbol{r}^{(m)}$ and makes an angle θ with the horizontal axis. The kernels in the operator definitions are given in terms of Bessel functions of the first kind:

$$K(t;c) = \int_0^\infty e^{-k^2 t} k^2 J_1(k) J_0(ck)\, dk \ , \ G(t;c) = \int_0^\infty e^{-k^2 t} k^2 J_1(k) J_2(ck)\, dk \ , \tag{5.18}$$

which are well-behaved smooth functions as shown in fig. 5.4.1.

The derived set of integral equations in eq. (5.17) can be solved, either analytically or numerically, directly for the quantities of interest, namely the unsteady hydrodynamic forces on the disks.

5.5 Conclusion

In this chapter, we have presented a framework to derive an integral equation for unsteady hydrodynamic force under unsteady Stokesian dynamics. We have shown the procedure systematically for the simplified model problem: of two stationary rigid disks in a two-dimensional flow field, experiencing unsteady force as the surrounding flow relaxes from an initial nonzero state. The model problem identifies many of the challenges that will be present when we consider more complex scenarios, such as movable disks and spheres, where other geometry-specific computations will be needed.

The integral equations we derive are shown to have well-behaved memory kernels. Particularly, they have spectral representations, which can be potentially used to realize the Markovian embedding procedure, discussed in chapters 3 and 6 to efficiently solve the integral equations numerically.

Appendix

5.A Typical computation of integrals

We consider the following term appearing in eq. (5.15) for $m = 1$:

$$I(t) = i \oint_{\boldsymbol{x}\in\partial\mathcal{V}^{(1)}} \int_{\mathbb{R}^2} e^{i\boldsymbol{k}\cdot\boldsymbol{x}} \hat{p}(\boldsymbol{k}, t) n_j'(\boldsymbol{x})\, d\boldsymbol{k}\, dS(\boldsymbol{x}) \ .$$

Substituting the expression for $\hat{p}$ from eq. (5.13) in the above, we get an integral over three quantities:

$$I(t) = \oint_{\boldsymbol{x}\in\partial\mathcal{V}^{(1)}} \int_{\mathbb{R}^2} \oint_{\boldsymbol{y}\in\partial\mathcal{V}} \Big(e^{i\boldsymbol{k}\cdot(\boldsymbol{x}-\boldsymbol{y})} \frac{\boldsymbol{k}\cdot\boldsymbol{T}(\boldsymbol{y})}{k^2} \Big) n_j(\boldsymbol{x})\, dS(\boldsymbol{y})\, d\boldsymbol{k}\, dS(\boldsymbol{x})$$

where the outermost integral is over the surface of the first disk, the middle integral over the spectral space $\boldsymbol{k}$, and the innermost is a surface integral over the union of the surfaces of the two disks. Therefore, we can decompose the integral into two contributions based on the innermost integral:

$$\begin{aligned} I(t) &= I_1(t) + I_2(t) \\ &= \oint_{\boldsymbol{x}\in\partial\mathcal{V}^{(1)}} \int_{\mathbb{R}^2} \Bigg[\oint_{\boldsymbol{y}\in\partial\mathcal{V}^{(1)}} \left\{ e^{i\boldsymbol{k}\cdot(\boldsymbol{x}-\boldsymbol{y})} \frac{\boldsymbol{k}\cdot\boldsymbol{T}(\boldsymbol{y})}{k^2} \right\} n_j(\boldsymbol{x})\, dS(\boldsymbol{y}) \\ &\quad + \oint_{\boldsymbol{y}\in\partial\mathcal{V}^{(2)}} \left\{ e^{i\boldsymbol{k}\cdot(\boldsymbol{x}-\boldsymbol{y})} \frac{\boldsymbol{k}\cdot\boldsymbol{T}(\boldsymbol{y})}{k^2} \right\} n_j(\boldsymbol{x})\, dS(\boldsymbol{y}) \Bigg] d\boldsymbol{k}\, dS(\boldsymbol{x}) \end{aligned} \tag{5.19}$$

We can express the position vector, $\boldsymbol{x}$, to the $m-$th disk's surface in terms of the known position vector of the disk's center and the unit normal vector at $\boldsymbol{x}$: $\boldsymbol{x} = \boldsymbol{r}^{(m)} - \boldsymbol{n}'(\boldsymbol{x})$. We reiterate $\boldsymbol{n}' = -\boldsymbol{n}$ to avoid misinterpretation. Consequently, the vector $\boldsymbol{x} - \boldsymbol{y}$ that appears

in the exponent in the above equation reduces to one of two expressions:

$$\boldsymbol{x}-\boldsymbol{y}=\begin{cases}-\boldsymbol{n'}(\boldsymbol{x})+\boldsymbol{n'}(\boldsymbol{y})\ , & \text{when } \boldsymbol{x},\ \boldsymbol{y} \text{ lie on same disk}\\ (\boldsymbol{r}^{(m)}-\boldsymbol{r}^{(n)})+(-\boldsymbol{n'}(\boldsymbol{x})+\boldsymbol{n'}(\boldsymbol{y})) & \text{when } \boldsymbol{x}\in\partial\mathcal{V}^{(m)},\ \boldsymbol{y}\in\partial\mathcal{V}^{(n)}\ ,\end{cases}$$

where note the vectors are oriented with respect to the disk for which the expression is written, and $(\boldsymbol{r}^{(m)}-\boldsymbol{r}^{(n)})$ is the known inter-particle separation (directional) vector.

We expand the integrals in eq. (5.19) and write them in the polar coordinates for disk indices $\alpha,\ \beta$:

$$\oint\limits_{\boldsymbol{x}\in\partial\mathcal{V}^{(\alpha)}} dS(\boldsymbol{x}) \int\limits_{\mathbb{R}^2} d\boldsymbol{k} \oint\limits_{\boldsymbol{y}\in\partial\mathcal{V}^{(\beta)}} dS(\boldsymbol{y})\Big(.\Big) = \int_0^{2\pi} d\theta_\alpha \int_0^{\infty} dk \int_0^{2\pi} d\theta_k \int_0^{2\pi} d\theta_\beta\ k\Big(.\Big)\ .$$

We perform these integrals sequentially and carefully to derive the final expression. Some identities that we use along the way are:

$$\int_0^{2\pi} e^{iC\cos(\theta-\phi)}\, d\theta = 2\pi J_0(C)\ , \tag{5.20a}$$

$$\int_0^{2\pi} e^{iC\cos(\theta-\phi)}\boldsymbol{n}(\theta)\, d\theta = 2\pi i J_1(C)\boldsymbol{n}(\phi), \tag{5.20b}$$

$$\int_0^{2\pi} e^{iC\cos(\theta-\phi)}\boldsymbol{n}(\theta)\boldsymbol{n}(\theta)\, d\theta = \pi J_0(C)\begin{pmatrix}1 & 0\\ 0 & 1\end{pmatrix} - J_2(C)\pi\begin{pmatrix}\cos(2\phi) & \sin(2\phi)\\ \sin(2\phi) & -\cos(2\phi)\end{pmatrix}\ , \tag{5.20c}$$

where ϕ is an arbitrary angle and $C\in\mathbb{R}$ is a non-negative constant. $\boldsymbol{n}=(\cos(\theta),\sin(\theta))$ is the unit vector on the disk's surface, written in terms of the angle θ which is measured with respect to the horizontal. The matrix that appears is a reflection matrix, about the unit normal vector at θ, centered at the disk locally. The functions $J_0,\ J_2$ are Bessel functions of the first kind.

Chapter 6

Markovian embedding of nonlocal equations using spectral representation

This chapter is a verbatim reproduction of the article titled *Markovian Embedding of nonlocal equations with spectral representation* [Jaganathan & Valani RN, arXiv:2402.00009]. I acknowledge the contributions of the co-author, Rahil N. Valani.

6.1 Introduction

Memory effects often emerge when modelling evolutionary processes having many degrees of freedom. They are usually the result of isolating a state variable of interest by "integrating out" the effects of the "environment" comprising other state variables. Mathematical models describing the evolution of state variables of such processes often take the form of nonlocal equations. Examples include particle motion in unsteady hydrodynamic environments [16], dynamics of self-propelled walking droplets [65] and chemically active particles [123], boundary evolution in diffusion processes in time-dependent domains [124, 125] and under nonlinear boundary forcing [126–128], dynamics of optical and mechanical resonators [129] and population dynamics [130]. In this chapter, we are concerned with nonlocal models where the evolution equation for a state variable $y(t)$ has the following canonical structure:

$$y^{(n)}(t) = L(t, y(t)) + \int_0^t N(y(t), y(\tau), t-\tau)\, d\tau \ , \tag{6.1}$$

where the superscript n indicates the order of the time derivative. The function $L(\cdot)$ is a local-in-time term driving the evolution, whereas the function $N(\cdot)$ is a memory kernel

of the nonlocal integral, which is also a nonlinear function of $y(t)$. Without the nonlocal term, eq. (6.1) can be readily transformed into a system of first order ordinary differential equations (ODEs) yielding a Markovian description. However, with the nonlocal term, such a transformation is not trivial. Different Markovian embeddings in an abstract extended space are commonly realized by introducing an auxiliary variable that accounts for the memory [131]. In this study, we show that a Markovian prescription can be realized for nonlocal equations of the form in eq. (6.1) by an embedding procedure that relies on the spectral representation of the nonlinear memory kernel (previously discussed for linear memory kernel in chapter 3).

Our approach involves expressing the nonlocal integral term in eq. (6.1) as a local-in-time term. We assume that the nonlinear memory kernel has a spectral representation of the following form:

$$N(y(t), y(\tau), t-\tau) = \int_\Gamma e^{\phi(k;y(t),y(\tau),t-\tau)}\psi(k, y(\tau))\, dk \ , \tag{6.2}$$

where Γ is a smooth contour in the complex-plane and ϕ, ψ are complex-analytic functions of the variable k. The spectral representation allows embedding of eq. (6.1) into an extended space. This is done by substituting the spectral representation in the memory term, followed by an interchange of order of integrals, to give:

$$\int_0^t \int_\Gamma e^{\phi(k;y(t),y(\tau),t-\tau)}\psi(k, y(\tau))\, dk\, d\tau =: \int_\Gamma H(k,t)\, dk$$

where $H(k,t)$ is the newly-introduced complex-valued auxiliary variable. Since it encapsulates "memory", we refer to it as the history function. Owing to the particular spectral form, we can infer that the history function has a Markovian evolution given by an ODE, parameterized by the spectral variable k. Therefore, we have the following local-in-time reformulation of eq. (6.1) in an infinite-dimensional space:

$$y^{(n)}(t) = L(t, y(t)) + \int_\Gamma H(k,t)\, dk \ , \tag{6.3a}$$

$$\dot{H}(k,t) = \dot{\phi}(k; y(t))H(k,t) + e^{\phi(k;y(t))}\psi(k, y(t)) \ , \tag{6.3b}$$

where we introduce overdot notation to denote time derivative in this chapter.

We demonstrate our embedding procedure for two physical models with nonlinear memory effects, namely the one-dimensional walking droplet and the single-phase one-dimensional Stefan problem. Both models illustrate that a Markovian embedding into an infinite-dimensional space can be constructed subject to a natural spectral representation of the

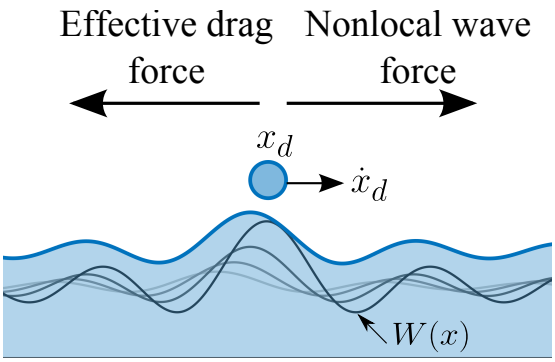

Figure 6.2.1: Schematic of the 1D walking droplet. Courtesy: *Rahil N. Valani*.

nonlinear memory kernel (eq. (6.2)). These models differ in the complexity of the auxiliary history variable introduced upon embedding, highlighting the versatility of the approach.

6.2 Walking droplets

A hydrodynamic active system described by non-Markovian dynamics is that of walking [132] and superwalking [133] droplets. By vertically vibrating an oil bath, a drop of the same oil can be made to bounce and walk on the liquid surface. Each bounce of the droplet locally excites a damped standing wave. The droplet interacts obliquely with these self-excited waves on subsequent bounces to propel itself horizontally, giving rise to a self-propelled, classical wave-particle entity (WPE). At large vibration amplitudes, the droplet-generated waves decay slowly in time. Hence, the motion of the droplet is affected by the history of waves along its trajectory. This gives rise to *path memory* in the system and makes the dynamics non-Markovian.

Oza *et al.* [65] developed a theoretical stroboscopic model to describe the horizontal walking motion of such a WPE. The model averages over the fast vertical periodic bouncing of the droplet and provides a trajectory equation for the slow walking dynamics in the horizontal plane. We consider a reduction of this model to one horizontal dimension, $x \in \mathbb{R}$ (see fig. 6.2.1a). Consider a droplet with position and velocity given by $(x_d(t), \dot{x}_d(t)) \in \mathbb{R}^2$, which continuously generates standing waves with prescribed spatial structure $W(x)$ that decay with time. The dynamics of a 1D WPE follows the non-dimensional integro-differential equation:

$$\ddot{x_d}(t) = -\dot{x_d}(t) - C_1 \int_0^t W'(x_d(t) - x_d(\tau)) K(t-\tau; C_2)\, d\tau, \tag{6.4}$$

where C_1 and C_2 are non-negative constants representing dimensionless wave-amplitude and inverse memory parameter, respectively[1]. We refer the reader to Ref. [65] for details and explicit expressions for these parameters. Equation (6.4) is a horizontal force balance of the WPE, with the right-hand side containing an effective drag term proportional to velocity $-\dot{x}_d(t)$ and the nonlocal memory term capturing the cumulative force on the particle from the superposition of the self-generated waves along its path. The memory kernel comprises the functions $W'(\cdot)$ and $K(\cdot)$; the former represents the wave-gradient where the prime denotes derivative with respect to its argument, and $K(\cdot)$ imposes the temporal decay. In the stroboscopic model of a walking droplet, $-W'(x) = J_1(x)$, where J_1 is the Bessel-J function of order one and $K(t) = e^{-C_2 t}$.

In the high-memory regime ($C_2 \ll 1$), WPEs exhibit hydrodynamic quantum analogs [134]. However, the regime may become experimentally difficult to access [135] due to the increased susceptibility of the system to the Faraday instability [136]. Numerical simulations provide an alternative with greater degree of control, but also entail dealing with the non-Markovian structure of eq. (6.4) and the associated time-dependent computational costs.

6.2.1 Markovian embedding for the stroboscopic model

We convert eq. (6.4) to a Markovian description in the following way. We recall the following integral representation of the Bessel-J_1 function for some $z \in \mathbb{R}$:

$$J_1(z) = -\frac{i}{\pi}\int_{-1}^{1} e^{ikz}\frac{k}{\sqrt{1-k^2}}\,dk\ .$$

Substituting the above in the memory term of eq. (6.4), followed by a switch in the order of integrals, we construct the equivalent local-in-time representation for the memory integral,

$$-\frac{i}{\pi}\int_0^t\int_{-1}^{1} e^{ik(x_d(t)-x_d(s))-C_2(t-s)}\frac{k}{\sqrt{1-k^2}}\,dk\,ds =: \int_{-1}^{1} H(k,t)w(k)\,dk$$

where the weight function $w(k) = 1/\sqrt{1-k^2}$ and $H(k,t)$ is a complex-valued function of time t and a real number k with a finite support in $[-1,1]$. The induced definition of $H(k,t)$ is

$$H(k,t) := -\frac{ik}{\pi}\int_0^t e^{ik(x_d(t)-x_d(\tau))-C_2(t-\tau)}\,d\tau\ . \tag{6.5}$$

The form of $H(\cdot)$ in eq. (6.5) suggests that it has a Markovian evolution according to an ODE parameterized by the spectral variable k. Consequently, combined with the definition

[1]Note that C_1 and C_2 are related to the dimensionless parameters κ and β in Oza *et al.* [65] by $C_1 = \beta\kappa^2$ and $C_2 = \kappa$.

of the droplet's velocity $\dot{x}_d = v_d$, we derive the following Markovian prescription for the WPE dynamics in the extended state space for $t > 0$:

$$\dot{v}_d(t) = -v_d(t) + C_1 \int_{-1}^{1} H(k,t) w(k)\, dk, \tag{6.6a}$$

$$\dot{H}(k,t) = -C_2 H(k,t) + ikv_d(t) H(k,t) - \frac{ik}{\pi}\,, \tag{6.6b}$$

subject to initial conditions (x_{d0}, v_{d0}) and $H(k,0) = 0$. We note in eq. (6.5) that $H(\cdot)$ preserves certain symmetries with respect to the spectral variable k at all times: the real part of the history function, $\mathrm{Re}(H)$, has an even-symmetry, whereas its imaginary part, $\mathrm{Im}(H)$, is odd-symmetric. Therefore, whereas the real and imaginary parts of the history function drive each other's dynamics, only the real part contributes to the memory integral in eq. (6.6a).

The resultant set of local differential equations eq. (6.6) can be readily solved using any standard time-integrator; we use the second-order Runge-Kutta scheme. An additional task involves computing the history integral over k. The integrand, with its finite support in $[-1, 1]$ and the form of weight function w, naturally suggests expansion of $H(k,t)$ in the bases of Chebyshev polynomials of the first kind. Therefore, we use the spectrally-accurate Clenshaw-Curtis quadrature method to approximate the integral:

$$\int_{-1}^{1} H(k,t) w(k)\, dk \approx \sum_{n=0}^{M} \omega_n H(k_n, t), \quad M \in \mathbb{N}\,,$$

where $k_n = \cos(n\pi/M)$ are the Chebyshev nodes and ω_n are the associated weights. We numerically solve eq. (6.6) for a few representative parameter sets (C_1, C_2). Figure 6.2.2 shows that the embedded system of equations eq. (6.6) successfully reproduces the previously known non-walking and walking regimes in the parameter space [137, 138]. For a steady walker, an analytical expression for its steady speed [65] is :

$$v_d^{\infty} = \frac{1}{\sqrt{2}} \sqrt{2C_1 - C_2^2 - \sqrt{C_2^4 + 4C_1 C_2^2}}\,. \tag{6.7}$$

The numerical solution for the steady walker attains the above analytical steady walking speed (dashed line) in fig. 6.2.2c.

In fig. 6.2.3, we plot the evolution of the real and imaginary parts of the history function in the $k-$domain over time. The plots at different time instances demonstrate symmetry-preserving numerical evolution of the history function in the spectral space, consistent with the exact evolution given by eq. (6.6b) The finite support of $H(k,t)$ in $[-1, 1]$ and its smooth-

ness demands a nominal, fixed (in time) requirement of fewer Chebyshev quadrature nodes to accurately compute the history integral.

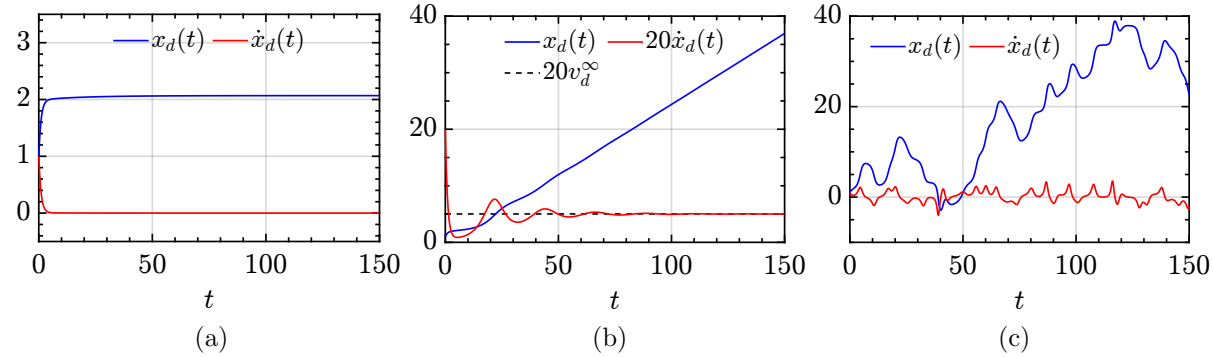

Figure 6.2.2: Typical known droplet states in the stroboscopic model obtained by solving the Markovian system (Equation (6.6)) for $(x_{d0}, \dot{x}_{d0}) = (1, 1)$: (a) *Non-walker* ($C_1 = 0.01, C_2 = 0.1$), (b) *Steady walker* ($C_1 = C_2 = 0.1$), (c) *Chaotic walker* ($C_1 = 1.5, C_2 = 0.01$). Velocity in (b) is scaled by a factor of 20 for visibility.

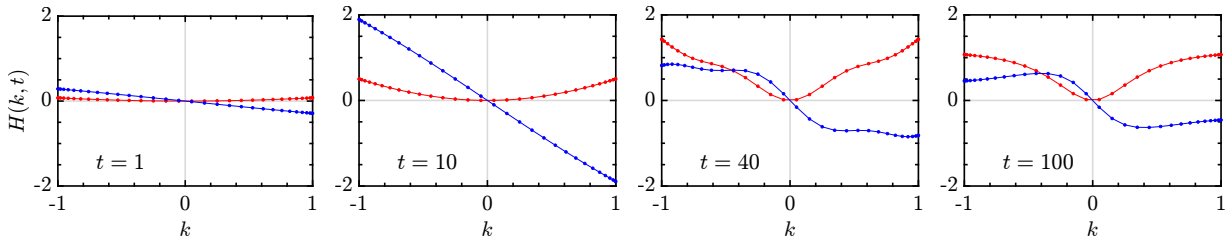

Figure 6.2.3: Evolution of real (red)/imaginary (blue) parts of the history function $H(k, t)$ at representative times for a steady walker ($C_1 = C_2 = 0.1$), with $H(k, 0) = 0$. $M = 30$ Chebyshev quadrature nodes are used to discretize the history function in $k-$ space.

There have been previous works [137, 139–141] that rewrite the integro-differential equation for the walker into a system of ODEs. However, these transformations work for only specific choices of the wave form $W(x)$. The Markovian embedding formalism is applicable for a broader class of wave forms that have a suitable spectral representation. This is particularly useful in generalized pilot-wave framework, where new hydrodynamic quantum analogues are being explored by investigating various wave forms [134].

6.3 Single-phase Stefan problem

We now consider the class of free boundary problems called the *Stefan problem*, which primarily describes phase-change processes such as the melting of a solid [66, 124]. In its

simplest non-dimensional formulation, it comprises a one-dimensional domain in $\mathbb{R}^+$, contiguously supporting a molten phase and a solid phase, separated at their interface, which is free to move as the solid melts (see fig. 6.3.1). The solid phase is modelled as an infinite heat sink maintained at the melting temperature at all times. Therefore, the simplified problem involves finding the solution pair $(\theta(x,t), l(t))$, where $\theta(x,t)$ describes the instantaneous temperature distribution in the molten phase and $l(t)$ is the location of the melting front. The function θ satisfies the diffusion equation $\partial_t\theta - \partial_x^2\theta = 0$ in $x \in [0, l(t)]$, subject to an arbitrary initial condition $\theta_0(x)$ in the initial domain $x \in [0, l_0]$ at $t = t_0$, and a temperature or heat flux condition at the fixed boundary $x = 0$. The moving front, which is at the melting temperature, is governed by the *Stefan condition* $\dot{l} = -\partial_x\theta(l(t), t)$.

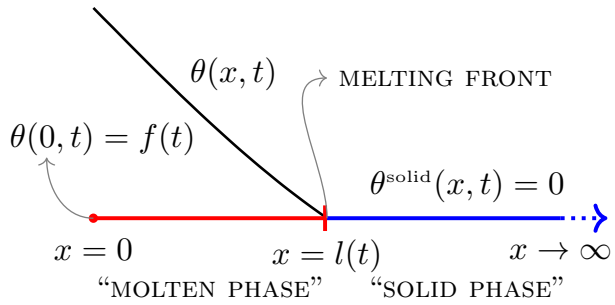

Figure 6.3.1: Schematic of 1D one-phase Stefan problem.

We consider the case where temperature is prescribed at the fixed boundary, $\theta(0,t) = f(t)$ for exposition. With primary interest in the interface's location, the bulk heat diffusion process in the molten phase may be effectively "integrated out" to derive a non-Markovian equation of motion for the moving front. The resulting velocity equation for the moving front, $v(t) = \dot{l}(t)$, is compactly written in the following nonlinear Volterra integral form for $t > t_0$ [66, 125]:

$$v(t) = g(t - t_0, l(t); \theta_0', l_0) + \int_{t_0}^{t} N(l(t), l(\tau), t - \tau; v(\tau), \dot{f}(\tau))\, d\tau \tag{6.8}$$

where $\theta_0', \dot{f}$ denote the spatial derivative and temporal derivative of θ_0, f respectively, and the function g is:

$$g(t - t_0, l(t); \theta_0', l_0) = -\frac{1}{\sqrt{\pi(t - t_0)}} \int_0^{l_0} \left(e^{-(l(t)+x)^2/4(t-t_0)} + e^{-(l(t)-x)^2/4(t-t_0)} \right) \theta_0'(x)\, dx\ . \tag{6.9}$$

The nonlinear kernel may be decomposed into contributions from forcing at the fixed bound-

ary and the unknown velocity of the solid-liquid interface as follows:

$$N(l(t), l(\tau), t-s; v(\tau), \dot{f}(\tau)) = v(\tau) N_1(l(t), l(\tau), t-\tau) + \dot{f}(\tau) N_2(l(t), 0, t-\tau) \ , \qquad (6.10)$$

with the definitions

$$N_1(x,y,z) = \frac{1}{2\sqrt{\pi}} \left(\frac{(x+y)e^{-(x+y)^2/4z} - (x-y)e^{-(x-y)^2/4z}}{z^{3/2}} \right), \quad N_2(x,y,z) = \frac{2}{\sqrt{\pi}} \frac{e^{-x^2/4z}}{z^{1/2}} \ .$$

Note that the function g is a local-in-time term. The second term on the right-hand side in eq. (6.8) is the memory term, which introduces non-locality and the nonlinear dependence on the moving front $l(t)$.

6.3.1 Markovian embedding for Stefan problem

As before, we construct an embedding such that the present non-Markovian representation for $v(t)$ may be turned Markovian. We claim the following spectral representation of the nonlinear kernel for a real k:

$$N_1(x,y,z) = \int_{-\infty}^{\infty} n_1(k;x,y,z)\, dk = \frac{i}{\pi} \int_{-\infty}^{\infty} \left(e^{-k^2 z + ik(x-y)} - e^{-k^2 z + ik(x+y)} \right) k \, dk, \qquad (6.11a)$$

$$N_2(x,y,z) = \int_{-\infty}^{\infty} n_2(k;x,y,z)\, dk = \frac{1}{\pi} \int_{-\infty}^{\infty} \left(e^{-k^2 z + ik(x-y)} + e^{-k^2 z + ik(x+y)} \right) dk \ . \qquad (6.11b)$$

Substituting the above spectral representations in the memory term, followed by a switch in the order of integrals, we derive the local representation with the introduction of the auxiliary history function $H(k,t)$:

$$\int_{t_0}^{t} \left(v(\tau) \int_{-\infty}^{\infty} n_1(k; l(t), l(\tau), t-\tau) dk + \dot{f}(\tau) \int_{-\infty}^{\infty} n_2(k; l(t), 0, t-\tau) dk \right) d\tau =: \int_{-\infty}^{\infty} H(k,t) dk \ .$$

The corresponding induced definition of the complex-valued history function is:

$$H(k,t) := \int_{t_0}^{t} \left(v(\tau) n_1(k; l(t), l(\tau), t-\tau) + \dot{f}(\tau) n_2(k; l(t), 0, t-\tau) \right) d\tau \ . \qquad (6.12)$$

Differentiating the above with respect to time, one may derive an ODE for the history function and realize the following equivalent Markovian prescription for the moving front for

$t > t_0$:

$$\dot{l}(t) = g(t - t_0, l(t); \theta_0', l_0) + \int_{-\infty}^{\infty} H(k,t)\, dk, \tag{6.13a}$$

$$\dot{H}(k,t) = -k^2 H(k,t) + ikv(t)H(k,t) + \frac{ik}{\pi}(1 - e^{2ikl(t)})v(t) + \frac{2}{\pi}e^{ikl(t)}\dot{f}(t)\ , \tag{6.13b}$$

subject to $l(t_0) = l_0, v(t_0) = g(0, l_0; \theta_0', l_0),\ H(k, t_0) = 0$. The history function in this case too preserves similar symmetries, suggesting that only its even-symmetric real part contributes to the history integral.

We show equivalence of the derived embedded Markovian system to the original non-Markovian system (eq. (6.8)) by numerically solving eq. (6.13). We use the second-order Runge-Kutta exponential time-differencing method [3] to solve for $H(k,t)$ due to stiffness introduced by the $-k^2 H$ term, and a standard integrator to solve for $l(t)$. The latter requires evaluating the history integral whose quadrature approximation, however, demands different treatment from the walker problem on two accounts:

1. $H(k,t)$ has infinite support in the $k-$space. While this warrants truncation of the $k-$space, its decay behavior at large k constraints the extent of truncation.

2. $H(k,t)$ is highly oscillatory; the frequency of oscillations increases with both k and t, which is ascribed to terms such as $e^{ikl(t)}$ in eq. (6.13b). The dependence on t through $l(t)$ exacerbates the oscillations in domain growth problems such as the one under discussion. Consequently, for accurate quadrature approximation, an increasingly dense set of collocation points in the truncated domain is required.

The above points are cautionary observations. While one could potentially address these concerns through computationally efficient methods, such an undertaking exceeds the scope of our present work. Therefore, we adopt a heuristic approach to compute the history integral. This involves truncating the $k-$space, mapping it to the interval $[-1, 1]$, and employing Clenshaw-Curtis quadrature to compute the history integral.

We consider the example corresponding to melting due to constant temperature at the fixed end, $f(t) = 1$, with the following analytical solution pair [142]:

$$\theta(x,t) = 1 - \frac{\mathrm{erf}(x/2\sqrt{t})}{\mathrm{erf}(\alpha)} \quad \text{for } x \in [0, l(t)], \quad l(t) = 2\alpha\sqrt{t}, \quad t > 0\ , \tag{6.14}$$

where the constant α satisfies the transcendental equation: $\sqrt{\pi}\alpha \exp(\alpha^2)\mathrm{erf}(\alpha) = 1$. To avoid the degeneracy at $t = 0$ due to zero-length domain, we let the process evolve for time $t_0 > 0$ to a non-zero domain length l_0. Prescribing $(\theta(x, t_0), l_0)$ as the initial state, we

numerically evolve eq. (6.13) from t_0. Figure 6.3.2 shows agreement between the numerical and analytical solutions (eq. (6.14)) for location of the interface, supplemented with the pointwise error. In fig. 6.3.3, we plot the pertinent history function in the truncated spectral space at different time instances. The highly oscillatory behavior of $H(k,t)$ in the truncated $k-$domain necessitates a large number of Chebyshev nodes to adequately capture it, ensuring the accuracy of the history integral.

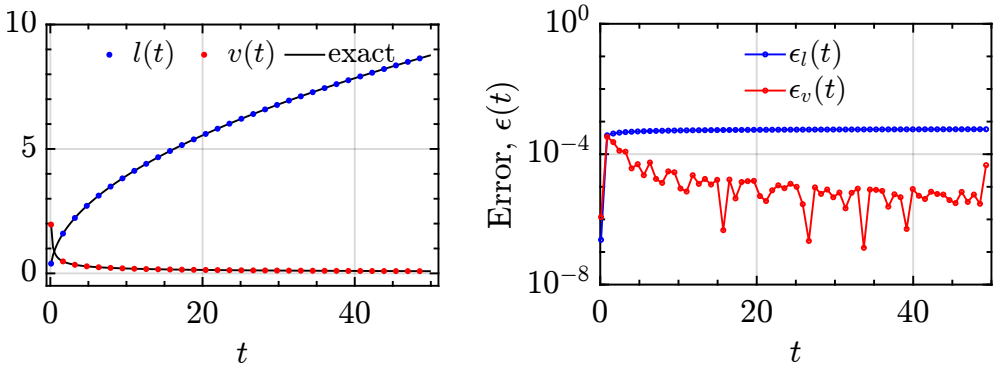

Figure 6.3.2: (a) Numerical response of the melting front to a constant temperature forcing $\theta(0,t) = f(t) = 1$ at the fixed end $x = 0$ along with (b) the instantaneous pointwise error.

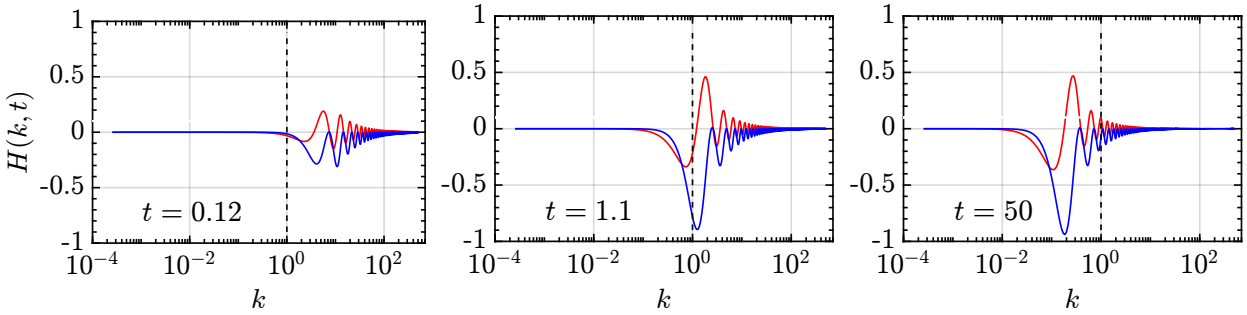

Figure 6.3.3: Evolution of real (red)/imaginary (blue) parts of the history function $H(k,t)$ in the truncated $k-$domain $k \in [0, 500]$ at different time instances for the single-phase Stefan problem subject to constant temperature forcing ($f(t) = 1$) at the fixed end $x = 0$. $M = 2000$ Chebyshev nodes were used to accurately compute the integral of the highly oscillatory history function.

6.4 Conclusions

We have described a Markovian embedding procedure for evolutionary equations with memory effects, which critically relied on the spectral representation of the memory kernel. We

have explicitly shown the embedding procedure for two physical models, namely the one-dimensional walking droplet and the single-phase Stefan problem. In both cases, the memory kernel is a nonlinear function of the underlying state variable.

Physical processes inherently follow Markovian dynamics when described adequately by all the driving state variables. The non-Markovian description of the evolution of an isolated state variable, such as in eqs. (6.4) and (6.8), is often the result of "integrating out" the effects of the "environment" comprising the other state variables. While identifying these integrated physical variables may not always be feasible, our Markovian embedding procedure provides an alternative mathematical reconstruction of the Markovian dynamics.

From a computational standpoint, a Markovian representation ensures that the numerical evolution of the corresponding time-discretized system incurs a time-independent cost. This is in contrast with the standard approaches for memory-dependent systems, where the computational cost grows with time. It is important to recognize that our Markovian embedding procedure comes at the cost of solving an additional local-in-time equation for the history function, which is an infinite-dimensional object. An accurate finite-dimensional approximation of the function depends on the behavior of $H(k,t)$ in the spectral space. In this regard, the two model problems discussed here demonstrate the extreme scenarios: the Stefan problem required a higher-dimensional approximation of the history function, comprising thousands of spectral variables, while the walker problem allowed a lower-dimensional approximation, with only a few tens of spectral variables for an accurate representation of the history function.

Chapter 7

Summary and future directions

In this thesis, we explore inertial particle transport in unsteady environments, accounting for the finite-time hydrodynamic response of both the particle and the fluid. We extensively use the unsteady Stokes model, which introduces nontrivial memory effects from the Basset-Boussinesq history (BBH) force. Through chapters 1 to 5, we emphasize the relevance of the unsteady Stokes model using analytical, numerical, and experimental approaches while highlighting its limitations where appropriate. In chapter 6, we look at nonlocal evolutionary processes–specifically, the walking droplets on a fluid surface and the classical Stefan's problem for phase-change, both of which are described by *nonlinear* memory effects.

In chapter 2, we describe experiments by our collaborators on the settling of an isolated rigid sphere in a highly viscous fluid under gravity. We test the unsteady Stokes model to capture both the sphere's trajectory and the perturbation flow it induces. We derive expressions for the unsteady flow structures and find that the model qualitatively captures experimental features such as vortex formation, its handedness, and drift at very small particle Reynolds numbers, in line with theoretical expectations. These features are not explained by the commonly-used quasi-steady Stokes model. However, the unsteady Stokes model fails to explain the asymmetric vortex drift at later times for larger particle Reynolds numbers ($Re_p \sim 1$). We attribute this to the increased significance of convective inertia, $(\boldsymbol{v} \cdot \boldsymbol{\nabla} \boldsymbol{v})$, in the dynamics, which is neglected in the model. Prior studies by [16, 143] provide an analytical and semi-analytical reference to develop models incorporating these effects. Notably, the unsteady Stokes model still accurately predicts the particle's trajectory, governed by the Basset-Boussinesq-Oseen (BBO)/Maxey-Riley-Gatignol (MRG) equation derived from the integrated effects of the ambient flow structures, for all $Re_p < 1$. The observed vortical structures may play a key role in collective particle dynamics via hydrodynamic interactions. This study encourages future experiments on multi-particle gravitational settling and the resulting collective dynamics, revisiting phenomena such as Crowley's instability [74] through

the unsteady Stokes model. This naturally leads to the topic of inter-particle interaction models addressed in chapter 5.

In chapter 5, we consider the simplified problem of two stationary disks embedded in a two-dimensional incompressible, Newtonian fluid. We develop a framework to derive integral equations that approximately describe the evolution of the unsteady hydrodynamic force on these disks, driven by inter-particle hydrodynamic interactions mediated by the unsteady Stokes flow. In the future, this framework could be extended to incorporate non-stationary, arbitrarily moving disks and spheres, with the ultimate goal of deriving an analogue of the MRG equation that includes inter-particle interactions. If successful, the model could be tested against the multi-particle experiments mentioned earlier to predict and explain collective behaviors.

In chapters 3 and 6, we examine nonlocal evolutionary equations and develop a memoryless framework to reformulate them as local-in-time equations in an extended space, using a Markovian embedding procedure. This procedure relies on a spectral representation of a problem-dependent mathematical quantity, though its physical interpretation is often not apparent. In chapter 3, we apply the procedure to the MRG equation, derived from the unsteady Stokes model for an accelerating sphere. The nonlocality in the MRG equation arises from the BBH force, which introduces linear memory effects from the particle's past states. We design an explicit time integrator, that we call RK-χTD schemes (section 3.4), for the local reformulation of the MRG equation, significantly reducing computational and memory storage costs. The construction procedure may be directly adapted to build numerical approaches for a class of fractional differential equations. In chapter 6, we extend the Markovian embedding approach to other evolutionary equations but with *nonlinear* memory effects from prior system states, namely the one-dimensional stroboscopic model for the walking droplets and the classical one-dimensional Stefan's problem for phase-change. In these cases, however, whether this local reformulation yields numerical benefits depends on the specific structure of the spectral representation. With the embedding procedure realized for these specific equations, there is potential to derive generalization rules based on the structure of the spectrally represented quantity, allowing broader application of the approach to nonlocal equations.

Finally, in chapter 4, we perform numerical simulations to examine trapping of finitely dense ($\rho_p/\rho_f < \infty$) inertial particles in a prototypical rotating flow described by a rotating pair of Lamb–Oseen vortices of identical strength, in the absence of gravity. We use RK-χTD from chapter 3 to evolve the particles under the MRG equation. Broadly, we find that the memory effects of the BBH force non trivially enhances clustering and trapping of inertial particles. In future, numerical simulations for particles in turbulent flow fields using the

explicit integrator for the MRG equation may provide insights, more directly applicable to physical and environmental flows of importance.

In conclusion, we have demonstrated the relevance of unsteady dynamics resulting from finite-time hydrodynamic response of the particle-laden system. While other physical factors/effects may sometimes dominate the unsteady hydrodynamic effects in physical applications, there is ample evidence that unsteady dynamics should not be dismissed, especially on the grounds of numerical challenges posed by the nonlocal BBH force. The importance of the history force requires careful consideration and can only be properly assessed with its accurate inclusion in models.

Bibliography

[1] Michael Bentwich and Touvia Miloh. The unsteady matched Stokes-Oseen solution for the flow past a sphere. *Journal of Fluid Mechanics*, 88(1):17–32, 1978.

[2] Takao Sano. Unsteady flow past a sphere at low Reynolds number. *Journal of Fluid Mechanics*, 112:433–441, 1981.

[3] S.M. Cox and P.C. Matthews. Exponential time differencing for stiff systems. *Journal of Computational Physics*, 2:430–455, 2002.

[4] Jean-Régis Angilella. Dust trapping in vortex pairs. *Physica D: Nonlinear Phenomena*, 239(18):1789–1797, 2010.

[5] Jeffrey S. Guasto, Roberto Rusconi, and Roman Stocker. Fluid mechanics of planktonic microorganisms. *Annual Review of Fluid Mechanics*, 44(Volume 44, 2012):373–400, 2012.

[6] Mari Takeuchi, Mark J. Doubell, George A. Jackson, et al. Turbulence mediates marine aggregate formation and destruction in the upper ocean. *Scientific Reports*, 9, 2019.

[7] T. J. Pedley and J. O. Kessler. Hydrodynamic phenomena in suspensions of swimming microorganisms. *Annual Review of Fluid Mechanics*, 24(Volume 24, 1992):313–358, 1992.

[8] Kakani Katija and John O. Dabiri. A viscosity-enhanced mechanism for biogenic ocean mixing. *Nature*, 460:624–626, 2009.

[9] G Falkovich, A Fouxon, and M G Stepanov. Acceleration of rain initiation by cloud turbulence. *Nature*, 419(6903):151–154, 2002.

[10] Michael Wilkinson, Bernhard Mehlig, and Vlad Bezuglyy. Caustic activation of rain showers. *Physical Review Letters*, 97:048501, 2006.

[11] G. K. Batchelor. The stress system in a suspension of force-free particles. *Journal of Fluid Mechanics*, 41(3):545–570, 1970.

[12] G. K. Batchelor. Chapter 3 - Equations governing the motion of a fluid. In *An Introduction to Fluid Dynamics*, pages 131–173. Cambridge University Press, 2000.

[13] Rama Govindarajan and Kirti Chandra Sahu. Instabilities in viscosity-stratified flow. *Annual Review of Fluid Mechanics*, 46(Volume 46, 2014):331–353, 2014.

[14] Pijush K. Kundu and Ira M. Cohen. Chapter 9 - Laminar flow. In Pijush K. Kundu and Ira M. Cohen, editors, *Fluid Mechanics (Second Edition)*, pages 271–311. Academic Press, Boston, second edition edition, 2002.

[15] G. K. Batchelor. Chapter 4 - Flow of a uniform incompressible viscous fluid. In *An Introduction to Fluid Dynamics*, pages 229–234. Cambridge University Press, Cambridge, UK, 1973.

[16] Phillip M. Lovalenti and John F. Brady. The hydrodynamic force on a rigid particle undergoing arbitrary time-dependent motion at small Reynolds number. *Journal of Fluid Mechanics*, 256:561–605, 1993.

[17] Carl Wilhelm Oseen. Über die Stokes'sche formel, und über eine verwandte aufgabe in der hydrodynamik. *Arkiv för Matematik, Astronomi och Fysik*, 6:29–46, 1910.

[18] P. G. Saffman. The lift on a small sphere in a slow shear flow. *Journal of Fluid Mechanics*, 22(2):385–400, 1965.

[19] Kwitae Chong, Scott D. Kelly, Stuart Smith, and Jeff D. Eldredge. Inertial particle trapping in viscous streaming. *Physics of Fluids*, 25(3):033602, 2013.

[20] Fabien Candelier, Bernhard Mehlig, and Jacques Magnaudet. Time-dependent lift and drag on a rigid body in a viscous steady linear flow. *Journal of Fluid Mechanics*, 864:554–595, 2019.

[21] Mathieu Le Provost and Jeff D. Eldredge. Mean transport of inertial particles in viscous streaming flows. *Physical Review Fluids*, 5:054302, 2020.

[22] F. Candelier, R. Mehaddi, B. Mehlig, and J. Magnaudet. Second-order inertial forces and torques on a sphere in a viscous steady linear flow. *Journal of Fluid Mechanics*, 954:A25, 2023.

[23] Sangtae Kim and Seppo J. Karrila. Chapter 2 - general properties and fundamental theorems. page 20. Dover Publications, Inc., Mineola, New York, 1991.

[24] Hassan Masoud and Howard A. Stone. The reciprocal theorem in fluid dynamics and transport phenomena. *Journal of Fluid Mechanics*, 879:P1, 2019.

[25] C. Pozrikidis. A study of linearized oscillatory flow past particles by the boundary-integral method. *Journal of Fluid Mechanics*, 202:17–41, 1989.

[26] Shidong Jiang, Shravan Veerapaneni, and Leslie Greengard. Integral equation methods for unsteady Stokes flow in two dimensions. *SIAM Journal on Scientific Computing*, 34(4):A2197–A2219, 2012.

[27] Yuto Hosaka, Ramin Golestanian, and Andrej Vilfan. Lorentz reciprocal theorem in fluids with odd viscosity. *Physical Review Letters*, 131:178303, 2023.

[28] Gwynn J. Elfring and John F. Brady. Active Stokesian dynamics. *Journal of Fluid Mechanics*, 952:A19, 2022.

[29] Martin R Maxey and James J Riley. Equation of motion for a small rigid sphere in a nonuniform flow. *The Physics of Fluids*, 26(4):883–889, 1983.

[30] R Gatignol. The Faxén formulae for a rigid particle in an unsteady non-uniform Stokes flow. *Journal of theoretical and applied mechanics*, 2:241–282, 1983.

[31] TR Auton, JCR Hunt, and M. Prud'Homme. The force exerted on a body in inviscid unsteady non-uniform rotational flow. *Journal of Fluid Mechanics*, 197:241–257, 1988.

[32] Bhargav Rallabandi. Inertial forces in the Maxey–Riley equation in nonuniform flows. *Physical Review Fluids*, 6:L012302, 2021.

[33] Divya Jaganathan, S Ganga Prasath, Rama Govindarajan, and Vishal Vasan. The Basset–Boussinesq history force: its neglect, validity, and recent numerical developments. *Frontiers in Physics*, 11:370, 2023.

[34] Alfred Barnard Basset. *On the descent of a sphere in a viscous liquid*, volume 41. 1910b.

[35] A. Belmonte, J. Jacobsen, and A. Jayaraman. Monotone Solutions of a Nonautonomous Differential Equation for a Sedimenting Sphere. *Electronic Journal of Differential Equations*, 2001(62):1–17, 2001.

[36] Mohammad Farazmand and George Haller. The Maxey–Riley equation: Existence, uniqueness and regularity of solutions. *Nonlinear Analysis: Real World Applications*, 22:98–106, 2015.

[37] S Ganga Prasath, Vishal Vasan, and Rama Govindarajan. Accurate solution method for the Maxey-Riley equation, and the effects of Basset history. *Journal of Fluid Mechanics*, 868:428–460, 2019.

[38] N. Mordant and JF Pinton. Velocity measurement of a settling sphere. *The European Physical Journal B*, 18:343–352, 2000.

[39] A. Rahman. Correlations in the motion of atoms in liquid Argon. *Physical Review*, 136:A405–A411, 1964.

[40] B. J. Alder and T. E. Wainwright. Decay of the velocity autocorrelation function. *Physical Review A*, 1:18–21, 1970.

[41] Robert Zwanzig and Mordechai Bixon. Hydrodynamic theory of the velocity correlation function. *Physical Review A*, 2:2005–2012, 1970.

[42] Allan Widom. Velocity fluctuations of a hard-core Brownian particle. *Physical Review A*, 3:1394–1396, 1971.

[43] E. J. Hinch. Application of the Langevin equation to fluid suspensions. *Journal of Fluid Mechanics*, 72(3):499–511, 1975.

[44] H. J. H. Clercx and P. P. J. M. Schram. Brownian particles in shear flow and harmonic potentials: A study of long-time tails. *Physical Review A*, 46:1942–1950, 1992.

[45] O.A. Druzhinin and L.A. Ostrovsky. The influence of Basset force on particle dynamics in two-dimensional flows. *Physica D*, 76(1):34–43, 1994.

[46] F. Candelier, J. R. Angilella, and M. Souhar. On the effect of the Boussinesq–Basset force on the radial migration of a Stokes particle in a vortex. *Physics of Fluids*, 16(5):1765–1776, 2004.

[47] Themistoklis P. Sapsis, Nicholas T. Ouellette, Jerry P. Gollub, and George Haller. Neutrally buoyant particle dynamics in fluid flows: Comparison of experiments with Lagrangian stochastic models. *Physics of Fluids*, 23(9):093304, 2011.

[48] Nicholas T. Ouellette, P. J. J. O'Malley, and J. P. Gollub. Transport of finite-sized particles in chaotic flow. *Physical Review Letters*, 101:174504, 2008.

[49] Renwei Mei, Ronald J. Adrian, and Thomas J. Hanratty. Particle dispersion in isotropic turbulence under Stokes drag and Basset force with gravitational settling. *Journal of Fluid Mechanics*, 225:481–495, 1991.

[50] S. Elghobashi and G. C. Truesdell. Direct simulation of particle dispersion in a decaying isotropic turbulence. *Journal of Fluid Mechanics*, 242:655–700, 1992.

[51] Vincenzo Armenio and Virgilio Fiorotto. The importance of the forces acting on particles in turbulent flows. *Physics of Fluids*, 13(8):2437–2440, 2001.

[52] M. van Aartrijk and H. J. H. Clercx. Vertical dispersion of light inertial particles in stably stratified turbulence: The influence of the Basset force. *Physics of Fluids*, 22(1):013301, 2010.

[53] Anton Daitche and Tamás Tél. Memory effects are relevant for chaotic advection of inertial particles. *Physical Review Letters*, 107:244501, 2011.

[54] Enrico Calzavarini, Romain Volk, Emmanuel Lévêque, Jean-François Pinton, and Federico Toschi. Impact of trailing wake drag on the statistical properties and dynamics of finite-sized particle in turbulence. *Physica D*, 241(3):237–244, 2012.

[55] Ksenia Guseva, Ulrike Feudel, and Tamás Tél. Influence of the history force on inertial particle advection: Gravitational effects and horizontal diffusion. *Physical Review E*, 88:042909, 2013.

[56] S. Olivieri, F. Picano, G. Sardina, D. Iudicone, and L. Brandt. The effect of the Basset history force on particle clustering in homogeneous and isotropic turbulence. *Physics of Fluids*, 26(4):041704, 2014.

[57] Anton Daitche. On the role of the history force for inertial particles in turbulence. *Journal of Fluid Mechanics*, 782:567–593, 2015.

[58] Ksenia Guseva, Anton Daitche, Ulrike Feudel, and Tamás Tél. History effects in the sedimentation of light aerosols in turbulence: The case of marine snow. *Physical Review Fluids*, 1:074203, 2016.

[59] M. A. T. van Hinsberg, H. J. H. Clercx, and F. Toschi. Enhanced settling of nonheavy inertial particles in homogeneous isotropic turbulence: The role of the pressure gradient and the Basset history force. *Physical Review E*, 95:023106, 2017.

[60] George Haller. Solving the inertial particle equation with memory. *Journal of Fluid Mechanics*, 874:1–4, 2019.

[61] K. D. Squires and J. K. Eaton. Preferential concentration of particles by turbulence. *Physics of Fluids A: Fluid Dynamics*, 3(5):1169–1178, 05 1991.

[62] L. P. Wang and M. R. Maxey. Settling velocity and concentration distribution of heavy particles in homogeneous isotropic turbulence. *Journal of Fluid Mechanics*, 256:27–68, 1993.

[63] W. C. Reade and L. R. Collins. Effect of preferential concentration on turbulent collision rates. *Physics of Fluids*, 12(10):2530–2540, 10 2000.

[64] A. Aliseda, A. Cartellier, F. Hainaux, and J. C. Lasheras. Effect of preferential concentration on the settling velocity of heavy particles in homogeneous isotropic turbulence. *Journal of Fluid Mechanics*, 468:77–105, 2002.

[65] A. U. Oza, R. R. Rosales, and J. W. M. Bush. A trajectory equation for walking droplets: hydrodynamic pilot-wave theory. *Journal of Fluid Mechanics*, 737:552–570, 2013.

[66] R.B. Guenther and J.W. Lee. *Partial Differential Equations of Mathematical Physics and Integral Equations*. Dover Books on Mathematics. Dover Publications, 2012.

[67] Tomek Jaroslawski, Divya Jaganathan, Rama Govindarajan, and Beverley McKeon. Basset-Boussinesq history force and inertia are relevant for unsteady particle settling dynamics, 2024. arXiv:2408.12530.

[68] M. R. Maxey and S. Corrsin. Gravitational settling of aerosol particles in randomly oriented cellular flow fields. *Journal of Atmospheric Sciences*, 43(11):1112 – 1134, 1986.

[69] J.C. Winterwerp. On the flocculation and settling velocity of estuarine mud. *Continental Shelf Research*, 22(9):1339–1360, 2002.

[70] K. Gustavsson, J. Jucha, A. Naso, E. Lévêque, A. Pumir, and B. Mehlig. Statistical model for the orientation of nonspherical particles settling in turbulence. *Physical Review Letters*, 119:254501, 2017.

[71] L G Leal. Particle motions in a viscous fluid. *Annual Review of Fluid Mechanics*, 12(Volume 12, 1980):435–476, 1980.

[72] Tymoteusz Miara, Christian Vaquero-Stainer, Draga Pihler-Puzović, Matthias Heil, and Anne Juel. Dynamics of inertialess sedimentation of a rigid u-shaped disk. *Communications Physics*, 7(1):47, 2024.

[73] Harshit Joshi and Rama Govindarajan. Sedimentation dynamics of bodies with two planes of symmetry. *Physical Review Letters*, 134:014002, 2025.

[74] Joseph M. Crowley. Viscosity-induced instability of a one-dimensional lattice of falling spheres. *Journal of Fluid Mechanics*, 45(1):151–159, 1971.

[75] Rahul Chajwa, Narayanan Menon, Sriram Ramaswamy, and Rama Govindarajan. Waves, algebraic growth, and clumping in sedimenting disk arrays. *Physical Review X*, 10:041016, 2020.

[76] David Deepwell and Bruce R. Sutherland. Cluster formation during particle settling in stratified fluid. *Physical Review Fluids*, 7:014302, 2022.

[77] Rishabh V. More and Arezoo M. Ardekani. Motion in stratified fluids. *Annual Review of Fluid Mechanics*, 55(Volume 55, 2023):157–192, 2023.

[78] Alfred Barnard Basset. A treatise on hydrodynamics: with numerous examples. *Deighton, Bell and Company*, 2, 1888.

[79] Provencher Gabriel Langlois, Mohammad Farazmand, and George Haller. Asymptotic dynamics of inertial particles with memory. *Journal of Nonlinear Science*, 25:1225–1255, 2015.

[80] G. G. Stokes. On the Effect of the Internal Friction of Fluids on the Motion of Pendulums. *Transactions of the Cambridge Philosophical Society*, 9:8, 1851.

[81] R. A. Millikan. The isolation of an ion, a precision measurement of its charge, and the correction of Stokes's law. *Physical Review (Series I)*, 32:349–397, 1911.

[82] Horace Lamb. On the uniform motion of a sphere through a viscous fluid. *Philosophical Magazine*, 21(6):112–121, 1911.

[83] Ian Proudman and J. R. A. Pearson. Expansions at small Reynolds numbers for the flow past a sphere and a circular cylinder. *Journal of Fluid Mechanics*, 2(3):237–262, 1957.

[84] Roland Clift, John R Grace, and Martin E Weber. *Bubbles, drops, and particles*. Courier Corporation, 2005.

[85] Divya Jaganathan, Rama Govindarajan, and Vishal Vasan. Explicit integrators for nonlocal equations: The case of the Maxey-Riley-Gatignol equation. *Quarterly of Applied Mathematics*, 83:135–158, 2025.

[86] Anton Daitche. Advection of inertial particles in the presence of the history force: Higher order numerical schemes. *Journal of Computational Physics*, 254:93–106, 2013.

[87] Roberto Garrappa and Marina Popolizio. Generalized exponential time differencing methods for fractional order problems. *Computers & Mathematics with Applications*, 62:876–890, 2011.

[88] Roberto Garrappa. Numerical solution of fractional differential equations: A survey and a software tutorial. *Mathematics*, 6:16, 2018.

[89] Lucien M. Brush, Hau-Wong Ho, and Ben-Chie Yen. Accelerated motion of a sphere in a viscous fluid. *Journal of the Hydraulics Division*, 90(1):149–160, 1964.

[90] MAT van Hinsberg, JHM ten Thije Boonkkamp, and HJH Clercx. An efficient, second order method for the approximation of the Basset history force. *Journal of Computational Physics*, 230(4):1465–1478, 2011.

[91] Fabián A. Bombardelli, Andrea E. González, and Yarko I. Niño. Computation of the particle Basset force with a fractional-derivative approach. *Journal of Hydraulic Engineering*, 134(10):1513–1520, 2008.

[92] A.J. Dorgan and E. Loth. Efficient calculation of the history force at finite Reynolds numbers. *International Journal of Multiphase Flow*, 33(8):833–848, 2007.

[93] M Parmar, S Annamalai, S Balachandar, and A Prosperetti. Differential formulation of the viscous history force on a particle for efficient and accurate computation. *Journal of Fluid Mechanics*, 844:970–993, 2018.

[94] Gregory Beylkin and Lucas Monzón. On approximation of functions by exponential sums. *Applied and Computational Harmonic Analysis*, 19(1):17–48, 2005.

[95] G. Casas, A. Ferrer, and E. Oñate. Approximating the Basset force by optimizing the method of van Hinsberg et al. *Journal of Computational Physics*, 352:142–171, 2018.

[96] S Campbell, F Ciccarello, GM Palma, and B Vacchini. System-environment correlations and Markovian embedding of quantum non-Markovian dynamics. *Physical Review A*, 98:012142, 2018.

[97] S Kretschmer, K Luoma, and WT Strunz. Collision model for non-Markovian quantum dynamics. *Physical Review A*, 94:012106, 2016.

[98] R McCloskey and M Paternostro. Non-Markovianity and system-environment correlations in a microscopic collision model. *Physical Review A*, 89:052120, 2014.

[99] P Siegle, I Goychuk, and P Hänggi. Markovian embedding of fractional superdiffusion. *Europhysics Letters*, 93(2):20002, 2011.

[100] Roberto Garrappa. Stability-preserving high-order methods for multiterm fractional differential equations. *International Journal of Bifurcation and Chaos*, 22(04):1250073, 2012.

[101] Marlis Hochbruck and Alexander Ostermann. Explicit exponential Runge-Kutta methods for semilinear parabolic problems. *SIAM Journal on Numerical Analysis*, 43(3):1069–1090, 2005.

[102] RF Curtain and H Zwart. *An introduction to infinite-dimensional linear systems theory*, volume 21. Springer Science & Business Media, 2012.

[103] Satya N. Majumdar. Persistence in nonequilibrium systems. *Current Science*, 77(3):370–375, 1999.

[104] Saumav Kapoor, Divya Jaganathan, and Rama Govindarajan. Trapping and extreme clustering of finitely dense inertial particles near a rotating vortex pair. *Journal of Fluid Mechanics*, 996:A44, 2024.

[105] P. Tanga, A. Babiano, B. Dubrulle, and A. Provenzale. Forming planetesimals in vortices. *Icarus*, 121(1):158–170, 1996.

[106] A. Bracco, P. H. Chavanis, A. Provenzale, and E. A. Spiegel. Particle aggregation in a turbulent Keplerian flow. *Physics of Fluids*, 11(8):2280–2287, 1999.

[107] H. K. Moffatt, S. Kida, and K. Ohkitani. Stretched vortices – the sinews of turbulence; large-Reynolds-number asymptotics. *Journal of Fluid Mechanics*, 259:241–264, 1994.

[108] G. Haller and T. Sapsis. Where do inertial particles go in fluid flows? *Physica D: Nonlinear Phenomena*, 237(5):573–583, 2008.

[109] S. Ravichandran, P. Perlekar, and R. Govindarajan. Attracting fixed points for heavy particles in the vicinity of a vortex pair. *Physics of Fluids*, 26:013303, 2014.

[110] T. Gallay and C. E. Wayne. Invariant manifolds and the long-time asymptotics of the Navier-Stokes and vorticity equations on R2. *Archive for Rational Mechanics and Analysis*, 163:209–258, 2002.

[111] R. Ramadugu, P. Perlekar, and R. Govindarajan. Surface tension as the destabiliser of a vortical interface. *Journal of Fluid Mechanics*, 936:A45, 2022.

[112] C. Cerretelli and C. H. K. Williamson. The physical mechanism for vortex merging. *Journal of Fluid Mechanics*, 475:41–77, 2003.

[113] T. Nizkaya, J. R. Angilella, and M. Buès. Note on point vortex pairs with unequal strengths. *Physics of Fluids*, 22(11):113301, 11 2010.

[114] J. R. Angilella, R. D. Vilela, and A. E. Motter. Inertial particle trapping in an open vortical flow. *Journal of Fluid Mechanics*, 744:183–216, 2014.

[115] F. A. Gerosa, H. Méheut, and J. Bec. Clusters of heavy particles in two-dimensional Keplerian turbulence. *European Physical Journal Plus*, 138(9), 2023.

[116] M.R. Maxey, E.J. Chang, and L-P. Wang. Interactions of particles and microbubbles with turbulence. *Experimental Thermal and Fluid Science*, 12(4):417–425, 1996.

[117] A. M. Ardekani and R. H. Rangel. Unsteady motion of two solid spheres in Stokes flow. *Physics of Fluids*, 18(10):103306, 10 2006.

[118] Athanassios S. Fokas. *A Unified Approach to Boundary Value Problems*. Society for Industrial and Applied Mathematics, USA, 2008.

[119] Bernard Deconinck, Thomas Trogdon, and Vishal Vasan. The method of Fokas for solving linear partial differential equations. *SIAM Review*, 56(1):159–186, 2014.

[120] Bernard Deconinck, Qi Guo, Eli Shlizerman, and Vishal Vasan. Fokas's unified transform method for linear systems. *Quarterly of Applied Mathematics*, 76(3):463–488, 2018.

[121] Shidong Jiang, Shravan Veerapaneni, and Leslie Greengard. Integral equation methods for unsteady Stokes flow in two dimensions. *SIAM Journal on Scientific Computing*, 34(4):A2197–A2219, 2012.

[122] Divya Jaganathan and Rahil N. Valani. Markovian embedding of nonlocal equations using spectral representation, 2023. arXiv:2402.00009.

[123] Gunnar G. Peng and Ory Schnitzer. Weakly nonlinear dynamics of a chemically active particle near the threshold for spontaneous motion ii. history-dependent motion. *Physical Review Fluids*, 8:033602, 2023.

[124] J. Stefan. Ueber die theorie der eisbildung, insbesondere über die eisbildung im polarmeere. *Annalen der Physik*, 278(2):269–286, 1891.

[125] A. S. Fokas and B. Pelloni. Generalized Dirichlet-to-Neumann map in time-dependent domains. *Studies in Applied Mathematics*, 129:51–90, 2012.

[126] W. Robert Mann and Frantisek Wolf. Heat transfer between solids and gasses under nonlinear boundary conditions. *Quarterly of Applied Mathematics*, 9(2):163–184, 1951.

[127] Joseph B. Keller and W. E. Olmstead. Temperature of a nonlinearly radiating semi-infinite solid. *Quarterly of Applied Mathematics*, 29(4):559–566, 1972.

[128] W. E. Olmstead and Richard A. Handelsman. Asymptotic solution to a class of nonlinear volterra integral equations. II. *SIAM Journal on Applied Mathematics*, 30:180–189, 1976.

[129] K. J. H. Peters and S. R. K. Rodriguez. Limit cycles and chaos induced by a nonlinearity with memory. *The European Physical Journal Special Topics*, 231(3):247–254, 2022.

[130] J M Cushing. *Integrodifferential equations and delay models in population dynamics*. Lecture Notes in Biomathematics. Springer, Berlin, Germany, 1977.

[131] C.M. Dafermos. Asymptotic stability in viscoelasticity. *Archive for Rational Mechanics and Analysis*, 37:297–308, 1970.

[132] Y. Couder, S. Protière, E. Fort, and A. Boudaoud. Dynamical phenomena: Walking and orbiting droplets. *Nature*, 437:208–208, 2005.

[133] Rahil N. Valani, Anja C. Slim, and Tapio Simula. Superwalking droplets. *Physical Review Letters*, 123, 2019.

[134] John W M Bush and Anand U Oza. Hydrodynamic quantum analogs. *Reports on Progress in Physics*, 84:017001, 2020.

[135] V. Bacot, S. Perrard, M. Labousse, Y. Couder, and E. Fort. Multistable free states of an active particle from a coherent memory dynamics. *Physical Review Letters*, 122:104303, 2019.

[136] M. Faraday. On a peculiar class of acoustical figures; and on certain forms assumed by groups of particles upon vibrating elastic surfaces. *Philosophical Transactions of the Royal Society London Series I*, 121:299–340, 1831.

[137] M. Durey, S. E. Turton, and J. W. M. Bush. Speed oscillations in classical pilot-wave dynamics. *Proceedings of the Royal Society of London Series A: Mathematical, Physical and Engineering Sciences*, 476:20190884, 2020.

[138] Rahil N. Valani, Anja C. Slim, David M. Paganin, Tapio P. Simula, and Theodore Vo. Unsteady dynamics of a classical particle-wave entity. *Physical Review E*, 104:015106, 2021.

[139] J. Moláček. *Bouncing and walking droplets : towards a hydrodynamic pilot-wave theory.* PhD thesis, Massachusetts Institute of Technology, 2013.

[140] Matthew Durey. Bifurcations and chaos in a Lorenz-like pilot-wave system. *Chaos*, 30(10):103115, 2020.

[141] Rahil N. Valani. Lorenz-like systems emerging from an integro-differential trajectory equation of a one-dimensional wave–particle entity. *Chaos*, 32, 2022.

[142] S.L. Mitchell and M. Vynnycky. Finite-difference methods with increased accuracy and correct initialization for one-dimensional Stefan problems. *Applied Mathematics and Computation*, 215:1609–1621, 2009.

[143] Renwei Mei and Ronald Adrian. Flow past a sphere with an oscillation in the free-stream velocity and unsteady drag at finite Reynolds number. *Journal of Fluid Mechanics*, 237:323–341, 04 1992.

List of publications

Published

1. **Divya Jaganathan**, S Ganga Prasath, Rama Govindarajan, Vishal Vasan. The Basset-Boussinesq history force: its neglect, validity, and recent numerical developments. *Frontiers in Physics*, 10.3389/fphy.2023.1167338.

2. **Divya Jaganathan**, Rama Govindarajan, Vishal Vasan. Explicit integrators for non-local equations: the case of the Maxey-Riley-Gatignol equation. *Quarterly of Applied Mathematics*, 10.1090/qam/1693, arXiv.2308.09714.

3. Saumav Kapoor, **Divya Jaganathan**, Rama Govindarajan. Trapping and extreme clustering of finitely dense inertial particles near a rotating vortex pair. *Journal of Fluid Mechanics*, 10.1017/jfm.2024.706.

Preprints

4. **Divya Jaganathan** and Rahil N. Valani. Markovian embedding of non-local equations using spectral representation. arXiv.2402.00009.

5. Tomek Jaroslawski, **Divya Jaganathan**, Rama Govindarajan, Beverley McKeon. Basset-Boussinesq history force and inertia are relevant for unsteady particle settling dynamics. arXiv.2408.12530.